2013

Physical Models of Cell Polarity

Tyler Drake
Lehigh University

Recommended Citation

Drake, Tyler, "Physical Models of Cell Polarity" (2013). *Theses and Dissertations.* Paper 1475.

Physical Models of Cell Polarity

by

Tyler Gates Drake

Presented to the Graduate and Research Committee

of Lehigh University

in Candidacy of the Degree of

Doctor of Philosophy

in

Physics

Lehigh University

January 2014

Approved and recommended for acceptance as a dissertation in partial fulfillment of the requirements for the degree of Doctor of Philosophy

Tyler Drake
Physical Models of Cell Polarity

Defense Date

Dissertation Director
(**Must Sign with Blue Ink**)

Approved Date

Committee Members:

Dimitrios Vavylonis

Jim Gunton

Daniel Ou-Yang

Jean Toulouse

Lynne Cassimeris

Table of Contents

Table of Figures

Table of Tables

Abstract

Fission yeast is a pill-shaped unicellular organism, and before dividing it grows by extension at the tips to double the original length. This work consists of mathematical models for how fission yeast controls this growth process. The models presented are either developed in collaboration with experimentalists or using published experimental work on this organism.

First, in collaboration with experimentalists Maitreyi Das and Fulvia Verde, we examine the organization of the signaling protein Cdc42, which we implicate as a central part of a control system for polarized growth. Cdc42, a member of the Rho family of proteins, binds to the inner membrane of the cell tips where growth occurs. In collaboration, we find that the fraction of Cdc42 bound to a given cell tip correlates to its growth rate, and that the amount of bound Cdc42 undergoes anti-correlated oscillations between the cell tips. We present a model that describes how Cdc42 and related proteins effect this organization, and shows how the oscillations could function as an exploratory mechanism to help the system overcome a kinetic barrier. Experimental results from our collaborators, such as a loss of correlation in very long cells and a reorganization after disruptive drug treatment, validate the model.

Next, using experimental results from literature, we turn to the patterned remodeling of the cell wall. We make a hypothesis that extends the result that Cdc42 marks cell tips for growth from previous work: that Cdc42 marks sites for growth on a microscopic level. A model for the fission yeast cell as an elastic shell being remodeled under turgor pressure at a rate that depends on cortical Cdc42 levels reproduces essential experimental results, namely the ratio of signal width to cell diameter and a linear relation between growth rate and pressure, and gives an estimation of the wall remodeling rate at the cell tips. Since this model predicts that cell diameter depends crucially on the width of a Cdc42 signal, we consider the plausibility of mechanisms for establishing the width of that signal. We find that stronger-than-linear feedback from cell diameter to signal width leads to unstable width regulation, and propose an independent length scale such as from a reaction-diffusion-type mechanism for a cell-diameter-independent Cdc42 signal width. Finally, we describe a mathematical model consisting of Cdc42-signal-dependent cell growth, diffusing Cdc42 growth zones with native width, and an axis-sensing microtubule-based system capable of delivering landmark proteins to the cell tips that bias the diffusion of the growth zones. Parameter dependence of the model is explored, and we show that such a model can give straight, bent, and wide cells, all of which have been observed by experimentalists. We argue that such a model is consistent with the roles of cytoskeleton- and signal-related proteins and known aberrant shapes of mutant cells.

As a whole, this work provides mechanistic insight into the system regulating shape and growth in one important model organism.

1. Introduction to Thesis

There is nothing more fundamental about a cell than the barrier separating it from the outside environment, and managing that barrier is crucial for function and survival. In many cells, that barrier takes the form of a cell wall outside the plasma membrane. Cells traffic material into and out of their walls, sense their environment through them, separate them into compartments for division, and change overall cell shape by modifying them. This work is a study of physical aspects of cell growth, the process by which cells change their shape and expand their size. In general, the targeting of cell growth involves signaling proteins such as the Rho family of proteins, used to relay information across and around the cell; the cytoskeleton, a group of biopolymers such as actin and microtubules that can bridge the gap of length scales between individual proteins and the cell; cytoskeleton-related proteins such as those of the Arp2/3 complex that promotes actin branching, which facilitate the organization of the cytoskeletal proteins and can interact with the signaling proteins; and the cell wall, often made up of different polysaccharides such as chitin or β-1,3-glucan, along with the enzymes responsible for remodeling it. To study this complex process, we focus on fission yeast, which is a common model organism for cell growth and polarity.

This chapter is intended as a roadmap for the chapters that follow. The thesis is organized around three chapters that correspond to three papers out of the four I wrote during my doctoral studies [1-4]. The work described herein is a study of how cells change their shape, and it focuses specifically on fission yeast, a single-celled eukaryotic organism. Because changes to shape occur at dramatically different scales of space and time from the proteins that make up the cell and their interactions (this idea will be further described in section 3-1), cell growth is governed by the collective dynamics of many proteins, and these collective interactions can be described by physics.

Following this overview, I have included a short chapter to provide background on necessary biological concepts for the thesis. This includes sections on signaling proteins, in particular of the Rho family; the cytoskeleton; and the methods from the experiments that will be described to motivate and test the physical theories detailed in this thesis.

Next, a background chapter describes theoretical work on fission yeast [4]. In the chapters that follow, I also describe how that work relates to research into other organisms that use similar mechanisms or follow similar growth patterns.

Chapter 4 details the results of our collaboration with Maitreyi Das and Fulvia Verde of the University of Miami [3]. We met them while presenting an early version of the theoretical side of this work at the American Society for Cell Biology Annual Meeting 2009. Because their experimental results fit with the way we were thinking about the system, we collaborated. Financed by an internal grant from Lehigh and a grant-in-aid from Sigma Xi, we visited their group in Miami. The resulting work described in Chapter 4 is a back-and-forth between mathematical modeling and experimental approaches. We contributed by doing the mathematical modeling, developing tools for image analysis and data processing, and by suggesting experiments. The biological experiments were carried out by Maitreyi Das under the guidance of Fulvia Verde. In brief, this work identifies a small protein called Cdc42 as a signal for growth in fission yeast and describes how it is organized between two growth sites by both biochemistry and physical processes such as diffusion.

Chapter 5 extends the investigation of Cdc42 and its role in guiding fission-yeast growth. This theoretical work, which comes from a recently published report [1], proposes a direct link between Cdc42 and changes in shape. In Chapter 4 we had looked at how Cdc42 marked one or both cell tips for growth, but here we examine the hypothesis that Cdc42 marks specific locations for growth and that through this mechanism the intensity profile of Cdc42 determines the shape of the cell. We develop a mathematical model of cell shape based on that hypothesis and a physical description of material being inserted into the wall. Additionally, this chapter contains further efforts to understand how Cdc42 organization comes about and to place this within the context of fission-yeast shape change.

Taken as a whole, this work should advance our understanding of how one particular organism controls its growth and shape. We address how the cell guides growth to one or two locations, in this case the cell tips, and investigate how growth works on a smaller scale. Further, we look at how a signal for growth might be physically organized, and provide a picture of how multiple modular components might work together to establish and maintain a polarized shape.

2. Rho GTPase Signals and the Cytoskeleton

The purpose of this chapter is to acquaint readers with a few basic concepts that are important for this thesis. In particular, I will describe how intracellular signaling by Rho GTPases by can function endothermally (*i.e.*, can consume energy), introduce a class of proteins called the cytoskeleton, and discuss the types of experiments that will appear in the thesis as motivation for and testing of the physical models we have developed.

2-1. Intracellular Signaling Can Be Endothermic Because Signaling Proteins Can Hydrolyze Nucleoside Triphosphates

Cells express genes by making proteins. Proteins do almost everything in a cell, including signaling, transport, adhering to or moving along a surface, managing division and reproduction, catalyzing biochemical reactions for metabolism, sensing the environment, and repairing DNA. Structurally, proteins are linear chains of amino acids connected by peptide bonds. Genes specify the sequence of amino acids, and variations in this sequence give rise to the diversity of proteins seen in cells. After or as genes are translated into proteins, the resulting chain of amino acids folds into a three-dimensional structure, either by itself or with assistance from a chaperone protein.

Some tasks performed by proteins require energy. Within cells, usable energy is stored in high-energy phosphate bonds of adenosine triphosphate (ATP) or guanosine triphosphate (GTP). The energy cells use to do work comes from the hydrolysis of ATP or GTP into ADP or GDP and a phosphate (P_i). The hydrolysis of ATP and GTP in cells is often assisted by proteins from families of hydrolase enzymes called ATPases and

GTPases respectively. Although there are GTPases with many forms and functions, they bind to and hydrolyze GTP using a common domain. Similarly, ATPases use a structural element usually called the ATPase fold to bind to and hydrolyze ATP. Both GTPases and ATPases can perform tasks that r work.

Guanine nucleotide exchange factors (GEFs) and GTPase-activating proteins (GAPs) assist GTPases in the cycle of hydrolyzing GTP for energy use (see Figure 1 A). The subcellular location of GEFs and GAPs is often highly regulated, for instance by binding to a transmembrane protein that responds to an extracellular cue, in order to specify where GTPase hydrolysis of GTP or replacement of GDP by GTP (see Figure 1 A) will take place.

The Rho family of GTPases is a set of small signaling proteins that function as molecular switches and, together with related GEFs, can transmit information from outside the cell (see Figure 1 B). Rho-family GTPases often regulate the assembly of actin structures, which will be described in the next section.

GEFs and GAPs typically facilitate the activity of one particular GTPase (as shown in Figure 1) by binding to them and inducing a conformational change, and multiple GAPs and GEFs can facilitate this activity (GTP hydrolysis) for a particular GTPase. For example, the fission-yeast signaling protein Cdc42, which will be examined at length in chapter 4, is regulated at least by GEFs Scd1 and Gef1 and GAPs Rga4 and Rga2 [5,6].

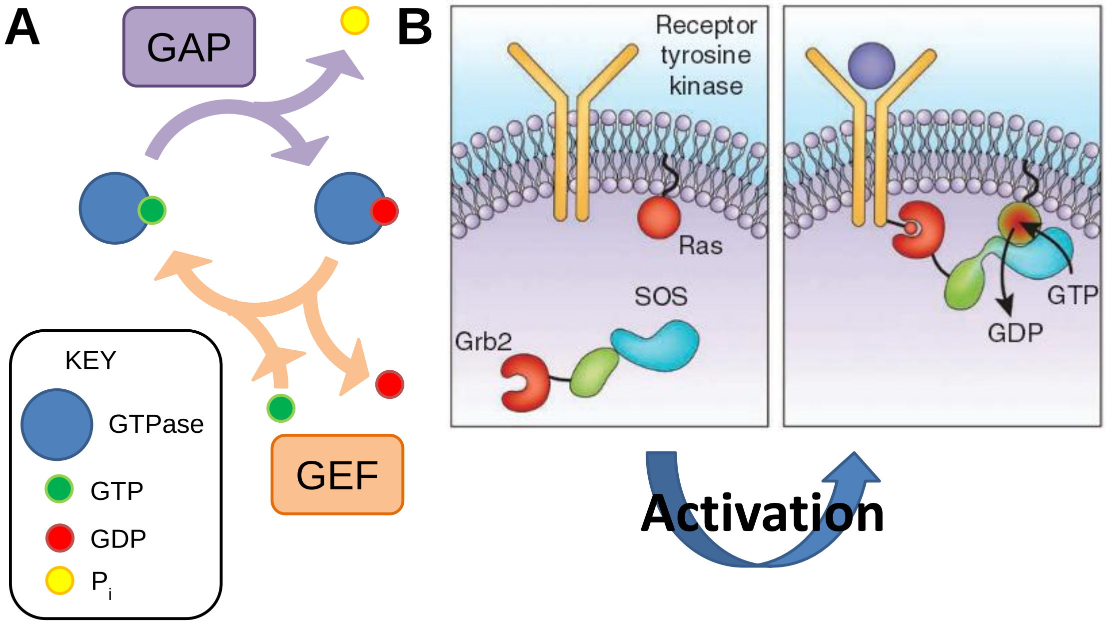

Figure 1. A. The cycle of GTP hydrolysis by GTPases is assisted by GAPs and GEFs, which can bind to the GTPase and induce a conformational change. **B.** An illustrative example of Rho GTPase signal transduction [7]. An external chemical (purple circle) binds to a receptor tyrosine kinase (yellow Y), inducing a change (small red circle linked to base of yellow Y). This allows the protein Grb2 to bind to the receptor. SOS (teal), which is a GEF for the Rho GTPase Ras, is bound in a complex with Grb2, and is brought to the membrane where it facilitates the activation of Ras. Through this chain of events, the activation of Ras reflects the external signal (purple circle).

One further class of regulators that affect the action of Rho GTPases is the guanosine nucleotide dissociation inhibitors (GDIs). These proteins bind to the inactive (GDP-bound) form of Rho GTPases and prevent them from exchanging GTP for GDP and associating with the membrane.

2-2. The Cytoskeleton Allows Cells to Form Complex Internal Structures

Because cells can harvest and harness energy, they can do work to build complex structures out of proteins. Perhaps nowhere is this more apparent than in the large, patterned structures of the cytoskeleton.

The cytoskeleton is the interior scaffolding of the cell, and it is composed of repeated building-block proteins, motor proteins, and other organizing proteins. Actin filaments and microtubules, two elements of the cytoskeleton, assemble spontaneously into linear structures. Actin subunits are ATPase proteins (see Figure 2 A) that bind together in two helical, interlaced strands to form polar microfilaments, and these microfilaments are linked, branched, severed, pulled on, capped, and elongated by actin-related proteins and myosin motor proteins [8]. For example, crawling cells often use a sheet-like protrusion called the lamellipodium, which is supported by a dense network of actin filaments for motility (see Figure 2 B). Cells control lamellipodia through multiple Rho-family GTPase signals, such as by the Cdc42 and Rac GTPases, two signaling proteins that activate proteins upstream of the Arp2/3 complex, which promotes the branching of actin filaments.

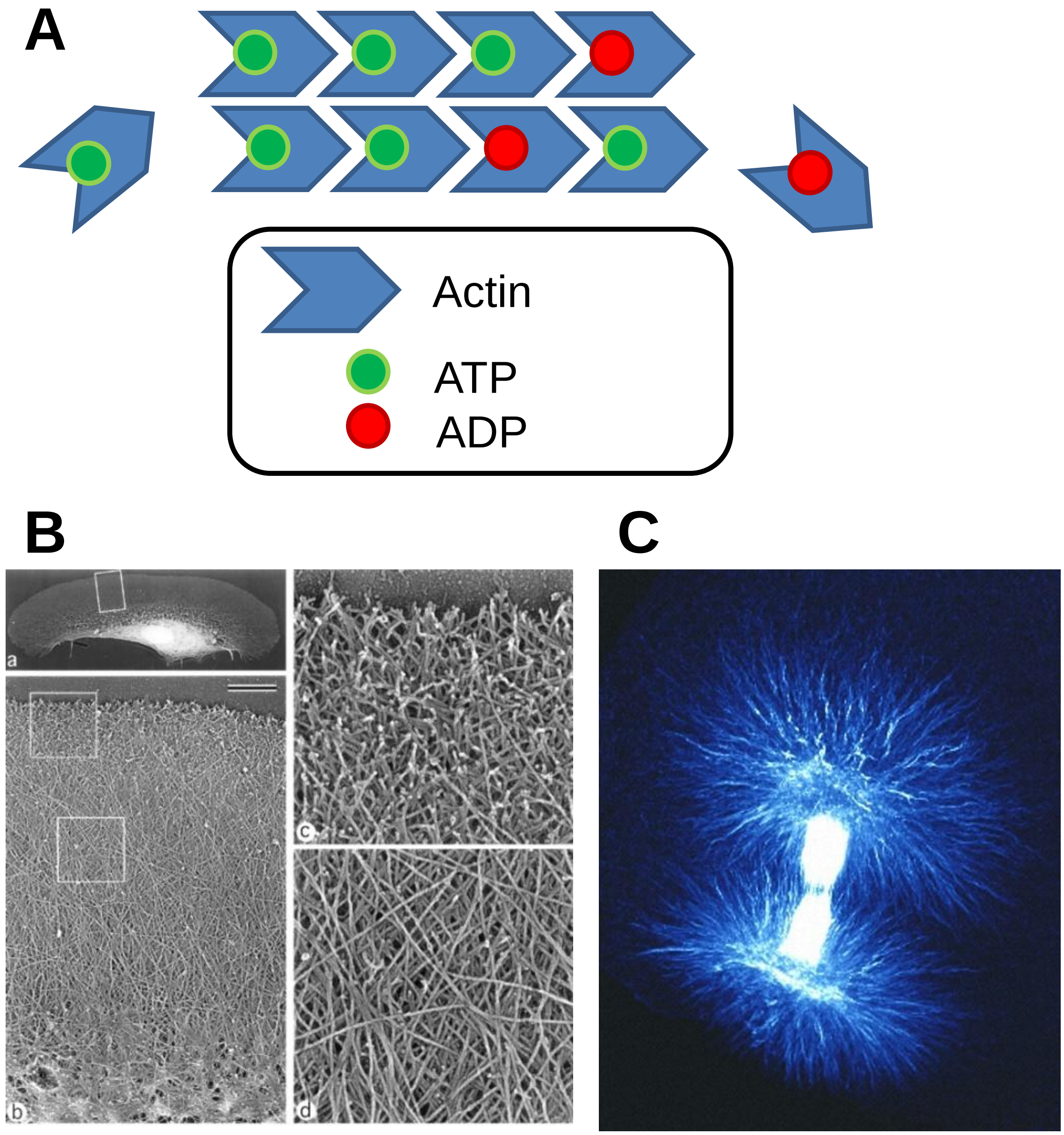

Figure 2. Actin and microtubules are biopolymers employed by the cell to form complex structures. **A.** Actin microfilaments are composed of two strands of actin monomers, which can be bound to ATP or ADP. **B.** In motile cells, such as this fish epidermal keratocyte, often have dense networks of actin filaments (image reproduced from [9]). Electron micrograph shows actin filaments from a detergent-extracted cell. Boxed region in (a) (top left) is enlarged in (b) (bottom left), and boxed regions in (b) are enlarged in (c) (top right) and (d) (bottom right). **C.** Fluorescent micrograph of microtubules in a mitotic spindle (image 39020 from Cell Image Library).

Microtubules are similar to actin cables in that they are linear, repeated structures, but they are instead made of tubulin dimers, bound pairs of α-tubulin and β-tubulin, both of which bind to GTP [10]. Most eukaryotic cells use microtubules to form a mitotic spindle that physically segregates copies of their chromosomes into two daughter cells (see Figure 2 C).

Superstructures such as the network of actin filaments in a lamellipodium or the mitotic spindle require many proteins to organize the basic components of actin subunits and tubulin dimers [8]. These complex structures are highly ordered, and cells consume energy through the use of ATPases and GTPases to build and maintain them in a background of homogenizing Brownian motion, for example by actin-filament treadmilling and active remodeling or continued replenishment of ordered structures like the lamellipodium.

2-3. Common Experimental Methods for Seeing and Manipulating Protein Levels

Many tools have been developed to understand the function and expression of proteins. This brief section gives an overview of the kind of experiments that will be described later in this thesis. Specifically, I will discuss fluorescent tagging of proteins and genetic manipulation of protein expression.

In order to observe proteins inside the cell, scientists use green fluorescent protein (GFP) [11]. This is a fluorescent protein found in the *Aequorea victoria* jellyfish. Once the genetic information for building this protein had been sequenced (and also improved), researchers could attach that information to the genes encoding for other proteins, and when the cell translated those genes the protein was built with a fluorescent marker. Labeled proteins can then be observed within the cell by fluorescence microscopy. In this thesis, many of the experiments described in Chapter 4 use a GFP construct that marks the GTP-bound form of the signaling protein and GTPase Cdc42.

Fluorescent tagging allows researchers to see (and in some cases count [12]) proteins in living cells, but in order to understand the role of different proteins it is also helpful to manipulate the amount of them. In practice, this is often done by the deletion and overexpression of genes. For example, deleting the gene *For3* from fission yeast, which encodes for the protein For3 that helps organize actin into cables, leads to cells without actin cables [13]. Overexpression works similarly, except that in that case the cell is rigged, sometimes by adding additional copies of the gene that encodes for the protein, to make more of the protein in question rather than none. This, along with other evidence, established the role of For3 in fission yeast. Many of the experiments in Chapter 4, such as those shown in Figure 14, involve deleting or overexpressing the genes that encode for GAPs and GEFs of the GTPase Cdc42.

Combining these two techniques, experimentalists can look at the behavior of some proteins while modulating the amount of others. The many variations and extensions of fluorescence microscopy and genetic manipulation are a powerful tool for understanding the roles of the many proteins that cells use.

3. Models of Growth and the Cytoskeleton in Fission Yeast

This chapter gives a review of modeling results on growth and the cytoskeleton of fission yeast. It is adapted from a review we wrote for HFSP Journal [4] during my first year working in the group.

3-1. Modeling the Cytoskeletal Dynamics of Fission Yeast in Asymptotic Regimes of Space and Time

Life is an ordered state of matter. To remain ordered and to divide or produce offspring, organisms must harvest and consume energy. Cells need to control their shape, direct their motion, polarize, and divide. The cytoskeleton is made up of varied filamentous networks that provide scaffolding for internal order [14]. Powered by adenosine triphosphate (ATP) and guanosine triphosphate (GTP) hydrolysis, the biopolymers and motor proteins of the cytoskeleton organize spontaneously into varied networks. These cytoskeletal structures span several orders of magnitude in length. The structural building blocks, proteins that are nanometers across, may be a thousandth the size of the largest structures they form. Cytoskeletal dynamics span several orders of magnitude in time as well. A single polymer subunit may diffuse across the cell in seconds, a ten-thousandth of the cell's division time.

Fission yeast (*Schizosaccharomyces pombe*) is one model organism for the study of subcellular organization mediated by the cytoskeleton [15]. Fission yeast undergo simple and reproducible cell shape changes. Additionally, the ease of genetic manipulations and microscopic imaging make the organism ideal for quantitative studies. A growing body of theoretical work examines cytoskeletal organization in asymptotic regimes of space and time [16]. These mathematical models support reduction of a system to essential components by matching the emergent behavior in the model with the observed behavior from experiments. Where model behavior differs from experimental results, these models motivate further investigation. This chapter reviews how modeling has contributed to understanding the role of the cytoskeleton in fission yeast cell polarization and mitosis, and provides context for the original research that follows.

3-2. Polarized Growth

Fission yeast grow along one axis. Their shape is simple: to first approximation, two hemispheres of constant radius cap a cylinder of increasing length (see Figure 3). When the length has doubled from birth, a contractile ring halves the cell [16,17]. Growth occurs at the tips. When growth starts, only the old end—the end not created by the previous division—grows. This monopolar growth eventually gives way to bipolar growth; this is called new-end take-off (NETO) [18]. Two components of the cytoskeleton, actin filaments and microtubules, mediate growth. These cells mark their tips for growth with the help of microtubules and execute growth with the help of actin filaments [19-21].

Microtubules polymerize towards both tips. Stable ends anchor close to the nucleus in bundles, while the dynamically unstable ends explore the interior near the cell tips (see Figure 3) [20,22,23]. Although individual microtubules are short lived, collectively they provide a directed track to the cell tips. The microtubules contribute to tip growth indirectly—motor proteins follow them to transport landmark proteins to the cell tips [24].

Actin polymerizes near growing tips. Regulating proteins organize actin filaments into two major structures: cables and patches [25,26]. The formin For3p associates with tip markers where it nucleates and polymerizes actin cables [27]. Cables wind from the tips through the cell body; motor proteins transport secretory vesicles and organelles along cables to the cell tips. The Arp2/3 complex nucleates actin patches near growth sites for endocytosis [28]. In patches, short actin filaments form dense, highly-branched networks.

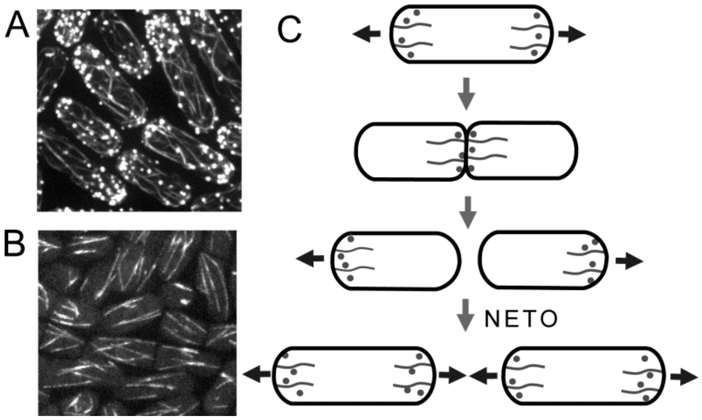

Figure 3. Images of yeast cells (Jian-Qiu Wu, Ohio State University) and yeast growth pattern. **A**. Images of the actin cytoskeleton in cells expressing GFP-CHD which binds to the sides of actin filaments. Actin cables and actin patches are seen distributed in monopolar and bipolar patterns. **B**. In cells expressing GFP-atb2, microtubule bundles run across the cell. **C**. Cartoon showing the redistribution of the actin cytoskeleton during the cell cycle. Prior to cytokinesis actin accumulates at growing tips; during mitosis it accumulates in the middle; daughter cells start to grow in a monopolar manner and transition to bipolar growth at new end take off.

Individually, all of these cytoskeletal structures are transient and disordered compared to the lifespan and order of the whole cell. Yet somehow they self-organize into a system robust enough to provide cells with a simple pattern of cell growth. These coupled growth processes, from a pool of structural components and regulator proteins, provide flexible and reliable scaffolding for the order required by living cells.

3-2-1. Models of Polarized Cell Growth and NETO

The simple growth pattern of fission yeast provides an opportunity to model how cells develop order. For instance, a model of NETO may reveal basic mechanisms responsible for polarity. Several lines of evidence indicate that NETO depends on cytoskeletal dynamics [29,30]. For example, some strains of yeast switch out of the monopolar state into the bipolar state after transient treatments with Latrunculin A (LatA), a drug that prevents actin polymerization by sequestering actin monomers [31]. In monopolar cells the microtubules are symmetrically distributed but the actin filaments and the formin nucleators concentrate at the growing old end. As the cells grow longer, they undergo NETO—transition to a state of symmetric growth, with symmetrically-distributed actin and microtubules. What could be the process responsible for the asymmetry in the actin distribution before NETO, and what triggers NETO?

One modeling study of NETO showed promising insights [32]. The authors cast the problem in the language of non-linear dynamics. According to their model, as cells elongate the state of asymmetric polymerization, or monopolar growth, becomes unstable. The cell assumes a stable symmetric polymerization state—bipolar growth. The model implicates length-dependent instability as the cause of NETO. This model belongs to a well-studied class of models called reaction-diffusion models [33].

In the model of Csikász-Nagy and others, microtubules transport a continuous field of dynamic landmarks towards the cell tips symmetrically, as suggested by experiments [30]. These markers contribute to conversion of a fast-diffusing substrate into a slowly-diffusing polymer. Likely candidates for the substrate and polymer are actin monomers and actin filaments, respectively. Dynamic landmarks activate autocatalytic actin polymerization: presumably, actin filaments in cables and patches further recruit actin nucleators. This could be consistent with experiments suggesting positive feedback in the polarization system [34]. Autocatalytic polymerization amplifies local noise, polarizing the cell and breaking symmetry. Autocatalytic growth at the growing tip depletes the cytoplasmic actin monomer pool and prevents growth at the other tip. As cells grow, diffusion limits the flow of actin monomers to the growing tip (Figure 4), the concentration of actin monomers at the new end increases, and the new end takes off. For some lengths, stable monopolar and bipolar states coexist, consistent with switching between states after transient LatA treatment [31]—a major success for the model.

Riveline approaches the problem differently [35]. According to his scaling arguments, asymmetric end curvature is responsible for the post-division growth pattern. The new end has a higher radius of curvature after septation; he proposes that this inhibits growth and argues NETO occurs when turgor pressure deforms the new end, decreasing its curvature. This model predicts that length at NETO increases with cell radius—this has not yet been tested.

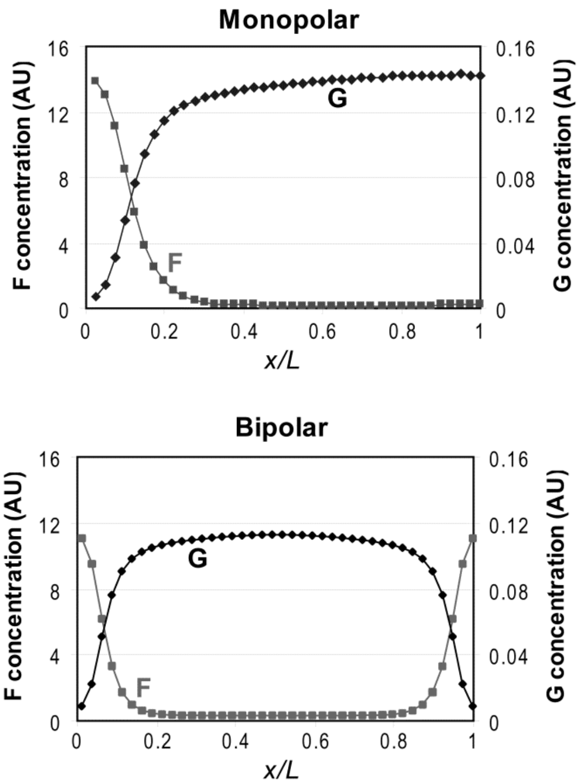

Figure 4. Polymer (F) and substrate (G) concentration gradients across the long axis of a growing cell (distance *x*, total cell length *L*), according to the model of Csikász-Nagy et al. Obtained from online content with default parameters (http://www.cellcycle.bme.hu/morphopaper/). Monopolar cell 8.50 µm, bipolar cell 14.0 µm. Both concentrations in arbitrary units using same scale on both axes.

These models don't directly contradict each other, but they do suggest different dominating factors. According to Csikász-Nagy and others, bipolar growth depends on diffusion limitation, unaccounted for by Riveline; according to Riveline, monopolar growth depends on a difference in tip curvature, unaccounted for by Csikász-Nagy and others. It remains unclear whether both mechanisms could coexist.

Modeling studies of NETO raise questions for experimentalists and theorists. Is NETO dependent on the existence of a growing actin monomer concentration gradient? So far, the actin-monomer concentration profile remains unmeasured in yeast. What new experimental evidence will emerge regarding the connections between cytoskeletal polarization and cell growth [36]?

What other models of bistable behavior are possible? Physical models of collective phenomena such as NETO are necessarily coarse-grained. How can such coarse-grained models be tested using advanced genetics operating at the molecular level?

3-2-2. Models of Interphase Cytoskeletal Subcomponents: Actin

Quantitative studies of the individual cytoskeletal subcomponents—microtubule bundles, actin cables [2], actin patches—explore links between molecular components and cell structure. Recent models describe these subcomponents.

Fission yeast formin For3p nucleates cables from cell tips. For3p molecules attach to cell tips, nucleate actin filaments, dislodge from cell tips, travel into the cell along actin cables, and travel back to the cell tip [27]. Wang and Vavylonis modeled coupled For3p and actin cable turnover [37] (see Figure 5). In their model, a continuous pool of actin monomers and a discrete pool of For3p molecules diffuse through the cell. The formins bind to cortical sites at the cell tips. Once bound, formins aid local actin polymerization until dissociation. Essentially, this model augments the mechanism proposed by Martin and Chang with rate constants, diffusion coefficients, and quantified localization.

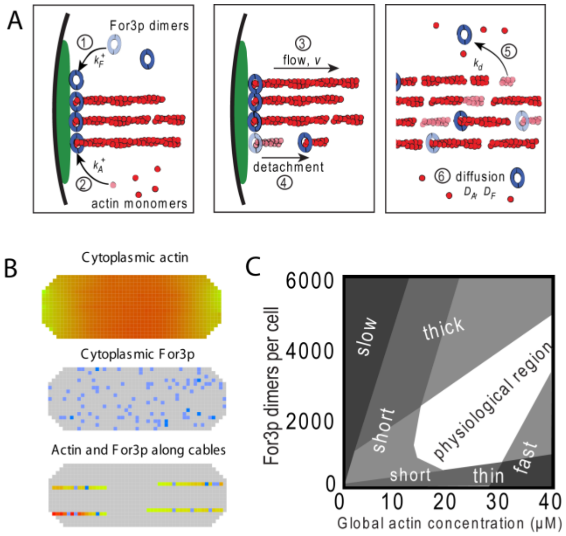

Figure 5. Model of actin cables in fission yeast [37]. **A**. Schematic showing the basic processes of the model. **B.** 3D computational lattice model (http://athena.physics.lehigh.edu/research /actin/cable/applet.html) accounting for the small number of For3p which are treated as discrete units. **C**. Qualitative dynamical phase diagram describing the morphology of the actin cable system as a function of actin and For3p concentration.

According to the model of Wang and Vavylonis, actin cables remove their own nucleator and undergo retrograde flow. Cable flow depletes the actin-monomer pool at the tips, causing a concentration gradient across the cell. More complex actin-For3p interactions could introduce non-linearity and therefore, potentially, multiple stable tip states. This may lead to another possible mechanism for NETO [37]. In such a mechanism, unlike in the model of Csikász -Nagy and others, bistability may be due to removal, rather than recruitment, of actin nucleators.

Cables are not the only actin superstructure in the cell. Fission yeast contain actin patches that contribute to endocytosis near regions of membrane remodeling (Figure 3 A). Recent experiments quantify the kinetics of assembly of coat proteins, Arp2/3 complex, actin, and other cofactors in patches [28,38,39], opening the door for modeling studies. Motivated by such data, Berro and others proposed an ordinary-differential-equation model of actin patches [40], finding that depolymerization of the actin filaments cannot account for the rapid loss of actin and instead suggesting that severing is responsible for that loss. Considering the physical structure in more detail, Liu and others modeled actin patch mechanics and assembly kinetics in budding yeast [41,42]. Their model includes coat protein assembly at the site of endocytosis, pushing forces by local actin polymerization, and phase separation of lipids and membrane proteins at the vesicle bud's border driven by membrane curvature. The combined effects of these processes generate tension around the bud neck, causing vesicle scission for endocytosis.

3-2-3. Models of Interphase Cytoskeletal Subcomponents: Microtubules

To maintain their shape, fission yeast cells must define their tips. Throughout growth, proteins follow microtubules and symmetrically mark both tips. Experimental and theoretical results suggest a simple mechanism is responsible for microtubule alignment.

According to recent experiments, normal cell shape and microtubule organization reinforce each other [34,43]. The rod shape directs elongating microtubules to the ends of the cell (Figure 3 B and Figure 6). Oriented to the long axis of the cell, they provide a path to the cell tips for polarity protein deposition. These proteins contribute to further preferential growth at the cell tips, exaggerating the linear shape that directs the microtubules. This interplay provides a feedback mechanism between cell shape and microtubule alignment. This alignment process also allows microtubules to center the nucleus [44-46].

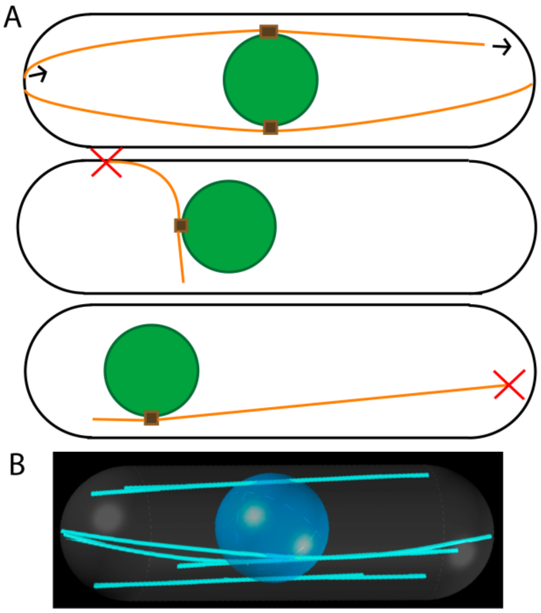

Figure 6. Illustration and results of the model of Foethke *et al*. [47]. **A**. Model schematic: microtubules orange, nucleus green, microtubule organizing centers (MTOCs) brown. Red X indicates likely catastrophe. The model includes 4 MTOCs each nucleating 4 microtubules. Top: normal alignment, polymerization, depolymerization. Middle: likely catastrophe due to force, preventing medially-aligned microtubules. Bottom: likely catastrophe due to length, necessary to center nucleus. **B**. Representative image at steady state, using online content with default parameters (http://www.nature.com/msb).

Microtubules may self-organize by virtue of their confinement and dynamics alone, but this is difficult to show experimentally: if one removes everything else conceivably affecting microtubule dynamics, what is left could not meaningfully be called a cell. Computer simulation helps here. A model extending *in vitro* findings shows it's possible, at least in principle, for observed organization to emerge from simple rules [47]. Indeed, simulations show a physical model can reproduce many measurable traits of interphase microtubule orientation. Foethke and others capture the essential features of microtubules *in vivo*, including their ability to center the nucleus, in a physical model using catastrophe rates dependent on both force and length (see Figure 6). As a result, microtubules that happen to grow with an unfavorable orientation depolymerize. Microtubules push the nucleus opposite their direction of growth. Since shorter microtubules are more stable, more force comes from the closer tip and the microtubule system centers the nucleus, as suggested by an earlier computational model [46]. These results extend easily to microtubule dynamics in differently-shaped cells, such as those in recent experiments where they are confined [34,43].

In the model mentioned above, Foethke and others assume that microtubules overlap and form stable antiparallel bundles near the nucleus. A similar model describes how they self-organize—with nucleators, crosslinkers, and motor proteins—into such bundles [48]. Microtubules slide across each other, but grind to a halt and form steady-state bundles when motor proteins cannot overcome friction due to crosslinkers.

3-3. Dividing the Cell

The simple growth pattern of fission yeast suggests a robust cytoskeletal system. It also rapidly adapts for division. Cells dramatically disassemble both microtubule and actin interphase cytoskeletal systems during mitosis, and each performs a major task in cell division. Microtubules mediate nuclear division, actin filaments mediate cytoplasmic division.

To finish division, an equatorial ring contracts and separates the daughter cells. This ring, the contractile ring (Figure 8 A), is a narrow bundle composed of actin filaments, myosin motors, and other proteins. A broad band of cortical nodes, made up of myosin and other proteins, tightens and becomes the contractile ring [17].

3-3-1. Assembly of the Contractile Ring

Successful contractile-ring assembly depends on the initial node distribution. One recent experimental and theoretical study provides quantitative insight into the positioning of node scaffolding component Mid1p [49]. In their one-dimensional reaction-diffusion model (Figure 7), an active form of Mid1p associates with the inner plasma membrane and the inactive form cannot. Activation occurs in the nucleus, deactivation occurs in the cytoplasm. Padte and others report that localized activation of Mid1p by the nucleus is insufficient to position Mid1p within a band in the center of the cell—active Mid1p diffuses across the cell before binding to the cortex. To match observed behavior, they introduce deactivators at the cells tips. This leads to a sharper Mid1p profile centered in the middle. Additionally, they identify some of the inhibitory interactions involving Pom1p. Some inhibitors may remain unidentified—cells lacking Pom1p still exclude Mid1p from one cell tip.

At least two experimental studies reveal further coupling of node distribution to the cell cycle [50,51]. Both studies argue that physical elongation causes Pom1p depletion near the cell's equator. Cdr2p signaling, inhibited by Pom1p in short cells, triggers cell cycle progression in long cells. The proposed mechanism provides a physical sensor within a signaling pathway. These studies further illustrate that cytoskeleton assembly couples with cytoplasmic gradients, local activation, and deactivation mechanisms to regulate internal organization in fission yeast.

Another study uses modeling to show how a Pom1 clustering mechanism could protect the function of the Pom1 mechanism from cell-to-cell variation [52]. Because Pom1 aggregates into clusters at higher concentrations, the Pom1 gradient is robust to changes in the amount of Pom1. This may be crucial for size homeostasis because the exact copy number of proteins appears to be difficult to control.

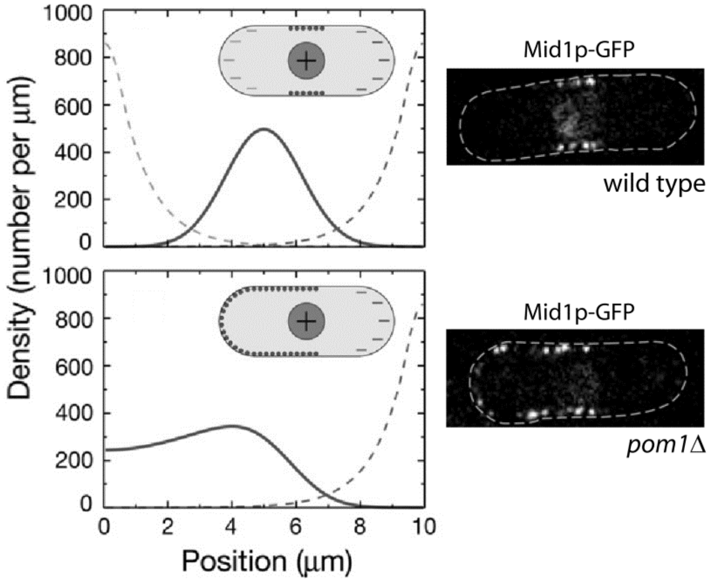

Figure 7. Results of model of positioning of Mid1p in nodes in the middle of the cell and experimental images [49]. The nodes are precursor components of the contractile ring. The model involves activation of Mid1p in the nucleus, deactivation near cell tips (dashed line), and binding of active Mid1p to the membrane. Top graph shows simulated distribution of membrane-bound Mid1p (solid line) as a function of position along the cell. Bottom graph shows membrane-bound Mid1p in cells lacking one of the polar inhibitors, Pom1p. Micrographs show the corresponding experimental images.

Cortical nodes attach firmly to the membrane, effectively restricting their movement to two dimensions. On this surface, the nodes condense, becoming a ring. Myosin motors in the nodes exert the force responsible for this condensation. The motors act on a dynamic meshwork of actin filaments nucleated by formin Cdc12p, another node protein [53]. Once actin filaments polymerize within the medial band, nodes move in ~20 sec bursts at velocities of ~30 nm/sec, starting, stopping, and changing direction. They condense into the contractile ring in 10 minutes [54].

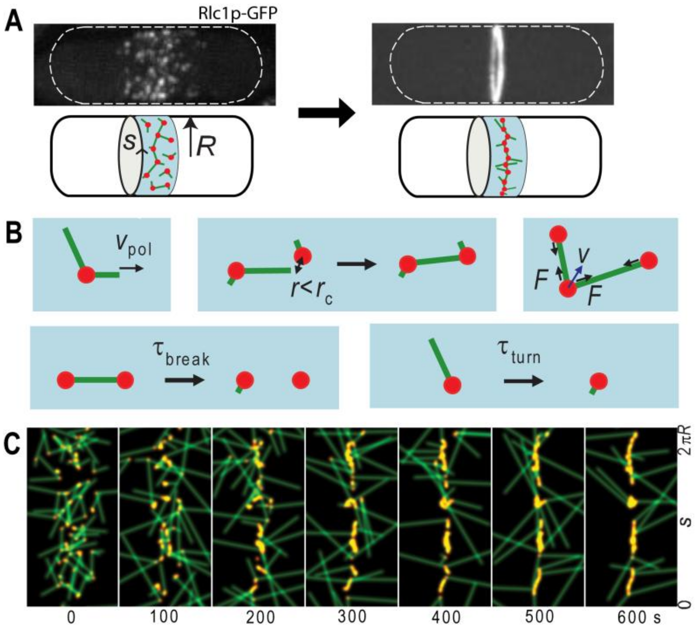

Figure 8. Search, capture, pull, and release model of contractile ring assembly [54]. **A**. Contraction of a broad band of myosin nodes into a narrow ring in fission yeast. **B**. Processes in the model. **C.** Simulated images of condensing broad band of nodes as a function of time (seconds). The y-axis in each simulated image is the arc length around the cylindrical body of a cell of radius R. The x-axis shows 4.5 µm along the long axis of the cell. Nodes are shown in red, actin filaments in green. Using parameter values measured in experiments, nodes formed an equatorial ring within a time consistent with experiment.

On the basis of these observations, Vavylonis and others proposed a stochastic mechanism for self-assembly [54]. According to their model, nodes search, capture, pull, and release (see Figure 8). Nodes search the cortical surface by nucleating actin filaments, which elongate in random directions along the cortex. Nodes capture each other by binding to filaments with myosin-II. Nodes pull each other because, once bound, myosin-II exerts a tensile force and reduces separation. Finally, nodes release as myosin-II dissociates and actin filaments disassemble. Monte Carlo simulations of this model—search, capture, pull, and release—reproduce the start-stop motion of nodes and generate contractile rings within a range of parameter values consistent with experiments. Varying parameter values leads to disconnected clumps, consistent with observations of Cdc12p-defective cells [55]. A recent theoretical work further quantifies requirements for clump formation [56].

Further theoretical work found that local alignment of the nodes could facilitate the condensation of cortical nodes into a contractile ring [57]. A collaborative effort involving theorists and experimentalists showed that actin-cross-linking proteins Ain1 and Fim1 counter a tendency for the nodes to form clumps [58]. As predicted by computer simulations that modeled actin filaments as semiflexible polymers, doubling the amount of type-II myosin Myo2 rescued cells from the defects caused by overexpression of Ain1.

This mechanism of node condensation in fission yeast further illustrates how random growth of filaments can establish transient connections between distant parts within the cell. The success of this unassisted random search and capture process suggests a reason for inherent randomness—it may confer resistance to rupture or relaxation during deformation, endowing assembly with a measure of robustness.

3-3-2. Modeling Ring Constriction

Following formation, the contractile ring constricts around the cell's equator and a septum forms. Several models describe actin filaments and myosin motors in contractile steady states [59-62]. But contractile rings exchange proteins with the cytoplasm during constriction.

One model describes ring constriction in nematode embryos [63] and, according to the authors, may apply to fission yeast. Their model includes dynamic exchange between ring and cytoplasm. This description identifies possible sources of the contractile stress needed to cleave the cell, including depolymerization of filaments cross-linked by end-tracking motor proteins. This model may inform a future model specific to fission yeast but details—magnitudes of forces, identities of proteins, inclusion of nodes—will necessarily differ.

Proctor and others use modeling to show that the mechanical stress due to myosin contraction is insufficient to overcome turgor pressure for constriction [64]. They provide an alternate explanation: that the contractile ring is a guide, but cell-wall assembly drives the ingression of the cleavage furrow. Supporting this conclusion, cells treated with Latrunculin A after contraction begins are able to complete division. In this model, the role of the actomyosin system is targeting, rather than executing, the physical separation of the cytoplasm into two compartments. Another study shows that shape also helps to guide division, using modeling to show that contractile rings would slip off rounder shapes and experiments to show that contractile rings slipped off of great circles around cells made into spheroplasts by enzymatic digestion of the wall [65].

3-3-3. Modeling the Mitotic Spindle

As the ring constricts, the spindle apparatus ensures both compartments contain the proper genetic material. One study describes how microtubule cross-linkers and sliding motors regulate spindle elongation during mitosis [66]. They present a computational model to describe their experimental results. In the model, microtubule bundling protein Ase1p, after dephosphorylation, recruits dephosphorylated kinesin motors to the spindle. These motors control the overlap distance of antiparallel microtubules and, accordingly, the spindle length. This mechanism ties spindle length to the cell cycle.

Most modeling studies of the spindle address other organisms. Reviewing efforts to understand mitosis, Mogilner and others stress the role of modeling in understanding how dividing cells form, maintain, and position their mitotic spindle [67]. And they describe progress, highlighting models that led to experiments that further led to refined models.

One such loop starts with a theoretical study of the budding yeast spindle during metaphase [68]. The authors model how microtubules emanating from the spindle pole body position kinetochores, the protein complex that attaches them to chromosomes. Their models generate images of simulated kinetochores and spindle pole bodies, which they compare statistically to corresponding images of live budding yeast. This rules out several models. Their models, which included dynamic instability of microtubules, failed to match their data with rescue and catastrophe frequencies independent of distance from the spindle. With this dependence included, simulated microtubules behaved as observed. This model did not include effects of kinetochore tension on microtubule dynamics. But more data emerged [69]. This led Gardner and others to refine the earlier model and conclude that a model with tension-dependent regulation better fits experimental data [70]. Continuing this line of inquiry, Gardner and others modeled how kinesin motor proteins may allow cells to raise the catastrophe rate of longer microtubules [71]. Another group employed image analysis to quantify the relationship between microtubules and kinetochores in budding yeast [72].

The models reviewed by Mogilner and others [67] consider the spindle apparatus as it functions in many organisms. But animal cells, budding yeast, and fission yeast solve this problem differently. The solution evolution found for fission yeast may differ due to cell geometry, chromosome count, and the closed nature of mitosis, among other factors. Efficient organelle positioning by microtubules depends on cell shape [73]. Pushing forces predominate in short and symmetric cell interiors such as the fission yeast nucleus. Pulling forces are more complex, but more capable in asymmetric or large interiors. Future quantitative models may support this distinction.

3-3-4. Modeling Meiosis

The fission yeast spindle pole body oscillates during meiosis. Selecting this system since oscillations often signal collective behavior, Vogel and others propose a minimal model to capture the cause of spindle pole body oscillations [74]. They focus on the collective behavior of dynein motor proteins. According to their study, dynein may self-organize and pull dynamic microtubules towards the tips of the cell. In the model, a large-scale behavior, oscillations across the cell, arises from simple interaction at the molecular level.

3-4. Lessons from the Existing Models of Fission Yeast

Healthy fission yeast depend on many systems and mechanisms. Modeling them individually provides progress towards a piecemeal mathematical description of the whole, to be refined according to experimental findings. Although the current description may seem more patchwork than quilt, recent models exhibit some overlap. Models of polarized growth assume cells define their tips and models of microtubule organization explain how cells could define their tips. Accumulating accurate quantitative models of cytoskeletal components reveals new questions about how they fit together and the extent to which this modular approach can provide an integrated description of a living cell.

We began the work that follows by trying to address the issues we pointed out with existing models of NETO in section 3-2-1 using mathematical modeling. Early in this effort, we met the experimentalists Maitreyi Das and Fulvia Verde, and their work on Cdc42 and its role in the control of polarized growth quickly shaped how we thought about growth control and shifted the focus of our work from the cytoskeleton, as described by Csikasz-Nagy and others [32], to the Cdc42 signaling pathway.

4. Modeling Cdc42 Oscillations at Growing Cell Tips

This chapter describes work done in collaboration with the Fulvia Verde and Maitreyi Das at the University of Miami. The chapter is based on our joint publication in *Science* [3].

4-1. Measuring Tip-Bound Cdc42 and Growth

In many cell types, the conserved guanosine triphosphatase (GTPase)[1] Cdc42 establishes cell polarity by regulating the cytoskeletal asymmetry required for normal cell function, differentiation, and motility [75-78]. In budding yeast, Cdc42 breaks the symmetry of spherical cells by clustering in one area of the membrane, the site of bud growth, through a winner-take-all positive-feedback mechanism [79-82]. However, such a mechanism cannot explain how multiple growing zones form simultaneously in other cells. Fission yeast (*Schizosaccharomyces pombe*) cells initially grow in one direction, from the tip that existed before division (the old end), and activate bipolar growth that includes the new end as well, once a minimal cell length has been achieved (this is NETO, as described in section 3-2) [18]. For these reasons, fission yeast is an ideal system to study how Cdc42 is distributed at multiple sites.

To characterize Cdc42 during the transition to bipolar growth, with Fulvia Verde and Maitreyi Das we measured the fluorescence intensity of a fusion protein [Cdc42/Rac interactive binding peptide–green fluorescent protein (GFP), CRIB-GFP] that binds specifically to activated, GTP-bound Cdc42 [83]. This is the active form of the Cdc42

---

[1] GTPases, as described in section 2-1, can bind to and hydrolyze guanosine triphosphate, allowing them to perform tasks in the cell that require energy. This is often done with the assistance of other proteins.

signaling protein [3]. Our collaborators Maitreyi Das and Fulvia Verde prepared the cells and collected images by focusing in the medial plane of the cell. The integrated CRIB-GFP intensity was measured over a crescent-shaped area that includes the entire tip signal. We subtracted the contribution of the cytoplasmic background by subtracting the mean intensity from a cytoplasmic region within the cell, separately for each cell. This process was assisted by an ImageJ plugin that blacks out anything below a threshold set to be three standard deviations from cytoplasmic-region mean[2]. This method was found to be fast, consistent, and to correspond well to the most careful, time-consuming measurements we could make. For time courses, we follow this procedure for every frame and collect the intensities of both cell tips.

In larger bipolar cells, CRIB-GFP intensities at cell ends showed out-of-phase oscillations with an average period of 5 min (Figure 9 A and B; Table 1 and Table 2). Oscillations were detectable in more than 50% of cells (Table 1), when imaging every 15 s instead of 1 min (Figure 9 C), and in three dimensions [3]. The rest of the cells displayed anti-correlated fluctuations without obvious periodicity. For shorter cells, non-growing ends still had detectable CRIB-GFP fluorescence, albeit at lower intensities than the older, growing ends (Figure 10). The tip intensities still underwent anti-correlated oscillations and fluctuations, but around asymmetric averages, unlike longer cells (Table 1).

---

[2] This is available at http://athena.physics.lehigh.edu/cdc42pombe as an ImageJ plugin.

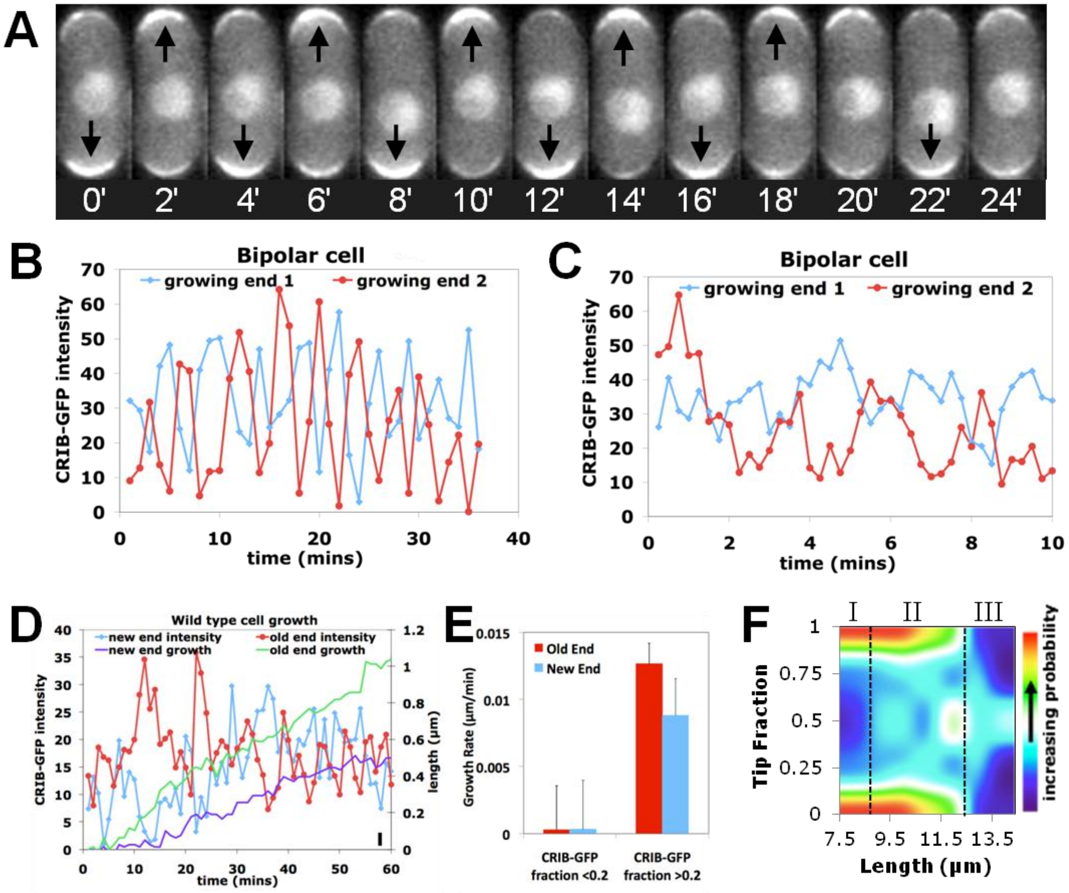

Figure 9. Oscillations and fluctuations of CRIB-GFP fluorescence at fission yeast cell tips. **A.** CRIB-GFP fluorescence at cell tips in a bipolar cell (2-min intervals). **B.** Old (red) and new end (blue) CRIB-GFP intensity in a bipolar cell (1-min intervals). A.U., arbitrary units. **C.** As in B, for 15-s intervals. **D.** Old (red) and new end (blue) CRIB-GFP intensity and cell growth at the old (green) and new (purple) ends in a cell undergoing NETO. The cell was 8.3 μm long at time 0. Bar, bottom right: 1 pixel = 0.1 μm. **E.** Instantaneous growth rate, binned by CRIB-GFP tip fraction (ratio of intensity at one tip over sum of tip intensities) and tip type (old or new). Error bars indicate SEM. **F.** Heat-map of CRIB-GFP tip fraction versus cell length in wild-type cells (smoothed data, n = 653). Note three regions: asymmetric, short cells (I); intermediate-length region with large intensity variations (II); symmetric, longer cells (III).

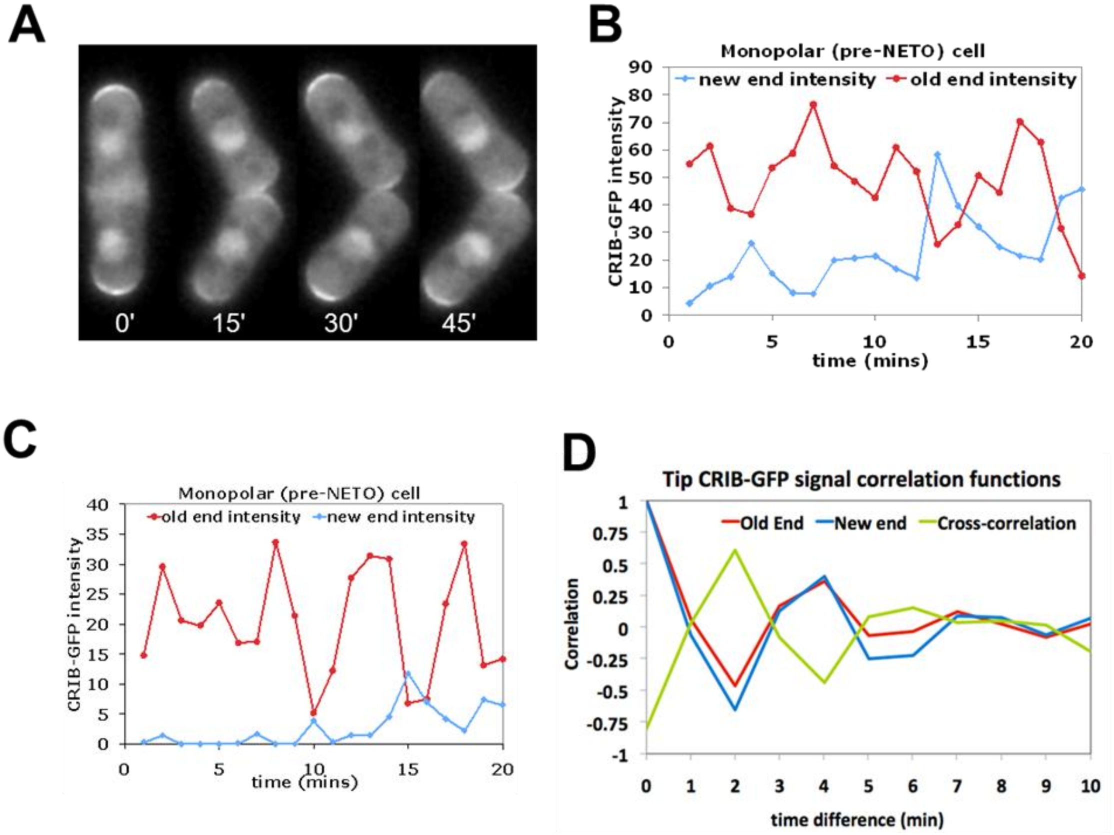

Figure 10. CRIB-GFP levels oscillate and fluctuate at both cell tips in monopolar cells. **A.** CRIB-GFP localization at the old (asterisks) and new (arrows) cell tips following cell division (1 minute intervals). Bar=5 µm. **B, C.** CRIB-GFP intensity at the old (red) and new (blue) cell tips in two short monopolar cell. **D.** Plot of tip intensity auto-correlation and cross-correlation functions for a cell exhibiting symmetric oscillations. The appearance of periodic peaks and valleys indicate oscillatory behavior with period 4 min, for both tips. The peak amplitude decays with increasing time difference, indicating a loss of coherence over a time interval of order 10 min. The valleys and peaks of the cross-correlation function occur together with peaks and valleys of the auto-correlation function, indicating that the two tips oscillate with phase difference 180°. The value of the cross-correlation function at zero time-difference was used to measure the degree of anti-correlation between tips.

We also examined cells, again prepared by Maitreyi Das and Fulvia Verde, in which scaffold protein Scd2 had been labeled with GFP. Scd2 is proposed to mediate Cdc42 activation by binding to the Cdc42 guanine nucleotide exchange factor (GEF)[3] Scd1 and to Cdc42 itself [84,85]. Scd2-GFP intensity at the cell tips oscillated and fluctuated much like CRIB-GFP intensity ([3] and Table 1), as did Scd1-3xGFP and Cdc42-GFP [3]. This shows that CRIB-GFP oscillations are unlikely to be a consequence of the labeling and instead reflect the behavior of the activated Cdc42 protein complex.To understand how GTP-Cdc42 levels might influence the NETO transition, we measured instantaneous cell growth rates along with CRIB-GFP intensity in cells undergoing NETO, which occurs in cells longer than 9 μm [18]. Intensities at both new and old ends fluctuated strongly over time (Figure 9 D). The instantaneous growth rate was correlated with abundance of CRIB-GFP at both old and new ends; cell tips with a CRIB-GFP tip fraction below 0.2 grew slower than tips with the fraction above 0.2 (Figure 9 E, section 4-6 in the appendices describes this calculation). Varied degrees of asymmetry were also observed at intermediate lengths in a population of asynchronous cells (Figure 9 F, region II). These findings indicate that NETO is a noisy transition driven by GTP-Cdc42 redistribution.

To determine the essential requirements for the transition from oscillating monopolar (asymmetric) to oscillating bipolar (symmetric) states during cell elongation, we developed a coarse-grained mathematical model (Figure 11 A) [32].

---

[3] These proteins facilitate the release of guanosine diphosphate (GDP) from a GTPase. This allows another guanosine triphosphate to bind to the GTPase.

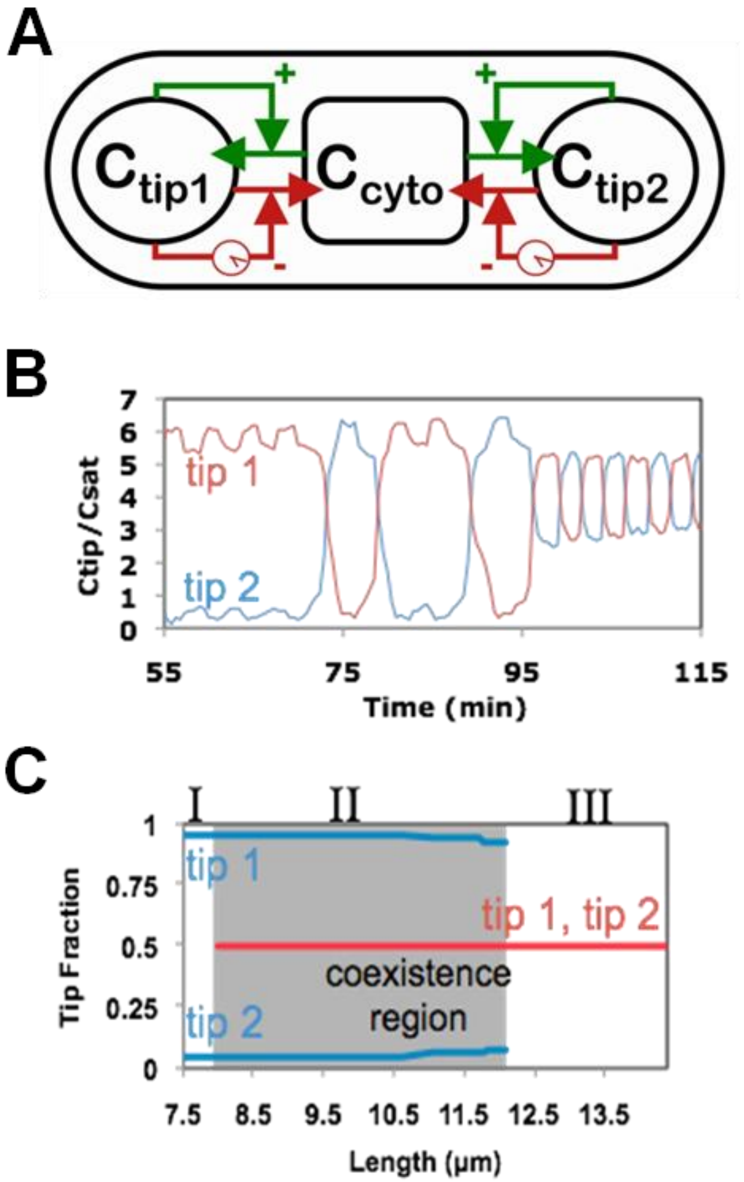

Figure 11. Mathematical model describing Cdc42 oscillations. **A.** Model schematic showing GTP-Cdc42 distribution between tips and the cytoplasm, autocatalytic amplification (green), and delayed dissociation (red). **B.** Simulation showing GTP-Cdc42 fraction at each tip as cell progresses from monopolar to bipolar growth. **C.** Model predicts three regions similar to Fig. 1G. Asymmetric states (I); "coexistence" of symmetric and asymmetric states (II); symmetric states (III).

4-2. Mathematical Model of Cdc42 Distribution

The mathematical model presented in this section describes how Cdc42 is distributed through an individual cell. The model is partly phenomenological, because the details of the many-protein system responsible for because the quantitative (and in some cases qualitative) details of the molecular interactions that guide Cdc42 location and activation. We later use this to make predictions about how genetic and pharmacological manipulations.

This model has a population of Cdc42 associated with each tip, C_{tip1} and C_{tip2}, and another one in the cytoplasm, C_{cyto}. We assumed that the tips compete for Cdc42 but assumptions that tips compete for Cdc42 GEFs or for Cdc42-GTP lead to similar results. The total amount $C_{\text{tot}} \equiv C_{\text{tip1}} + C_{\text{tip2}} + C_{\text{cyto}}$, increases in proportion to cell volume V [3]. Cell tips appear to be inherently symmetric in terms of their ability to recruit active Cdc42. We looked for the simplest possible symmetric model that can exhibit asymmetric (i.e. polarized) behavior depending on the stage of growth. We considered a model in which a population of Cdc42 is distributed among three subpopulations: a cytoplasmic population (total number C_{tot}) and one at each tip (total numbers C_{tip1}, C_{tip2}) as in Figure 11 A. Two observations justify considering distinct tip-bound Cdc42 subpopulations: (i) fission yeast define their tips with microtubule-delivered polarity factors such as Tea proteins [22], and (ii) we observe dense CRIB-GFP signal corresponding to tip-bound active Cdc42. We assume that tip-bound Cdc42 remains in the tip region since membrane-bound Cdc42 diffusion is sufficiently slow [86,87]. We consider the cytoplasmic population to be well mixed because small signaling proteins diffuse across the cell in seconds while tip concentration changes take minutes. This justifies considering as one uniform population.

With association to the tips from the cytoplasm and dissociation to the cytoplasm from the tips, the dynamical equations for this system are:

$$\begin{aligned}
\frac{dC_{tip1}}{dt} &= \frac{\lambda^{+}}{V} C_{cyto} - k^{-} C_{tip1} \\
\frac{dC_{tip2}}{dt} &= \frac{\lambda^{+}}{V} C_{cyto} - k^{-} C_{tip2} \\
C_{tot} &\equiv C_{tip1} + C_{tip2} + C_{cyto}
\end{aligned} \tag{1}$$

Here λ^{+} and k^{-} represent rate constants while V is the cell volume. The volume appears in the denominator of the association term because the cytoplasmic concentration interacts with the tip surface, a fixed area. Note that fission yeast's one-dimensional elongation keeps volume approximately proportional to length. The third equation above is mass conservation, and C_{tot} represents the total amount of active Cdc42.

As written, with λ^{+} and k^{-} constant, the derivatives can be set to zero and the system admits direct steady-state solution:

$$C_{tip1} = \frac{C_{tot} k^{-} \lambda^{+}}{V k^{-2} + 2 k^{-} \lambda^{+}}, \quad C_{tip1} = \frac{C_{tot} k^{-} \lambda^{+}}{V k^{-2} + 2 k^{-} \lambda^{+}}, \quad C_{cyto} = \frac{C_{tot} V k^{-2}}{V k^{-2} + 2 k^{-} \lambda^{+}} \tag{2}$$

This solution however is symmetric, representing bipolar cells. To obtain asymmetric solutions, representing monopolar cells, we allow the rate constants to depend on the local tip amount. Both amplifying association and inhibiting dissociation can break the symmetry. We assume amplifying association because of supporting evidence in budding-yeast Cdc42 [80,86]. For a linear association rate, $\lambda^{+} = \lambda_0^{+} + \lambda_1^{+} C_{tip}$, the solution is slightly more complicated but remains symmetric. But a higher-order term,

$\lambda^+ = \lambda_0^+ + \lambda_n^+ C_{tip}^n$, with $n \geq 2$, gives asymmetric solutions. The analytical expressions are unwieldy though, because even for $n = 2$ the linear tip-amount dependence of C_{cyto} makes the equation cubic. However one salient feature is that solutions remain monopolar as volume increases: because nothing in the model allows a weaker tip to catch up so the tip with a bigger population always accumulates faster.

In order to enable the weaker tip to accumulate Cdc42, we introduce saturation at the tips by gradual shut-off of the on rate term with an exponential. The rate becomes:

$$\lambda^+ = \left(\lambda_0^+ + \lambda_n^+ C_{tip}^n\right)\exp\left(-C_{tip} / C_{tot}\right) \tag{3}$$

While the biochemical mechanisms leading to this equation in fission yeast are unknown, modeling studies in budding yeast have demonstrated how a power-law dependence can arise from the biochemistry of Cdc42 activation, with the order depending on the number of molecules required for a reaction [86]. Similarly, saturation may arise biochemically from a limit in the number accessory membrane-bound proteins or membrane binding sites. Saturation has not been introduced in budding yeast where Cdc42 concentrates on one site—here we need it to get bipolarity.

Equations (1) and (3) define a system that reaches stationary steady states (see section 4-7 for numerical methods). Accounting for the observed oscillations requires augmentation. A symmetric, two-population system of first-order ODEs—which this can be reduced to with mass conservation—cannot oscillate around a symmetric state[4]. To model the oscillatory system, we included time-delayed negative feedback [88,89]. Such a mechanism is required for oscillations and represents components recruited to the tips

---

[4] Proof: a clockwise or counterclockwise rotation around a symmetric state in the phase portrait implies its opposite (*i.e.*, a counterclockwise or clockwise rotation), leading to a contradiction.

by Cdc42 that promote its own dissociation. Likely mechanisms include recruitment of GTPase-activating proteins (GAPs)[5] or Cdc42-mediated nucleation of actin cables that in turn increase the rate of cortical Cdc42 dissociation through endocytosis [89]. We write the addition as a perturbation in the new parameter ε:

$$k- = k_0^-\left[\left(1-\frac{\varepsilon}{2}\right)+\varepsilon\frac{C_{tip}(t-\tau)^h}{C_{tip}(t)^h+C_{tip}(t-\tau)^h}\right] \tag{4}$$

This adds two more parameters: the time constant, τ, and the Hill coefficient, *h*. The above rate corresponds to a removal mechanism initiated τ ago that acts on the current tip-bound population in a switch-like manner. If earlier tip-amount is much larger than the current tip-amount, the dissociation rate reaches a value $k^- = k_0^-\left(1+\varepsilon/2\right)$ When the earlier amount is much smaller, the dissociation rate reaches $k^- = k_0^-\left(1-\varepsilon/2\right)$. The switch-like mechanism with an adaptable reference point assumes optimal sensitivity near the present value of tip-amount. Large nonlinearities (large *h* values) could result from a cascade of weakly nonlinear feedback mechanisms. Setting ε, *h*, or τ to zero recovers the stationary model, namely equations (1) and (3) with constant k^-.

In the model above we assume that association of Cdc42 to the tips occurs through Cdc42 activation, implying that tips compete for a common pool of Cdc42. Identical results are obtained in a model that assumes competition for the GEFs of Cdc42. In this case, the monopolarity of the *gef1*Δ cells in Fig. 2E would be interpreted to be due to decreased total GEF amounts: it can be shown that decreasing C_{tot} has a similar effect to decreasing the rate constant λ^+ as in Supplementary Fig. 6. Another possibility is that tips compete for a common pool of Cdc42-GTP. In this case, C_{cyto} in the model

---

[5] These proteins stimulate the hydrolysis of GTP by GTPases.

represents Cdc42-GTP free in the cytoplasm and/or bound to membranes, organelles and the nucleus. Deletion of Gef1 would lead to a decrease in the total amount of Cdc42-GTP, so cells would become more asymmetric due to the scarcity of Cdc42-GTP.

Instead of describing specific molecular interactions, we took into consideration several experimental observations to predict system behavior. We assumed that tips compete for Cdc42 or its effectors and regulators, on the basis of observed GTP-Cdc42 anticorrelations. We also assumed that positive and delayed negative feedbacks combine to generate oscillations, as they do in the bacterial Min system [90]. We added noise to represent random concentration fluctuations and to capture the observed variability (Figure 12 A). The model reproduced the observed time courses: dominant-tip oscillations in short cells (with anticorrelated lagging tip) and out-of-phase oscillations at both tips in long cells [90]. We added noise to represent random concentration fluctuations and to capture the observed variability (Figure 12 A). The model reproduced the observed time courses: dominant-tip oscillations in short cells (with anticorrelated lagging tip) and out-of-phase oscillations at both tips in long cells (Figure 11 C). Allowing different rate constants at the two tips caused them to oscillate around slightly different averages, as observed in many cells (Figure 12 B).

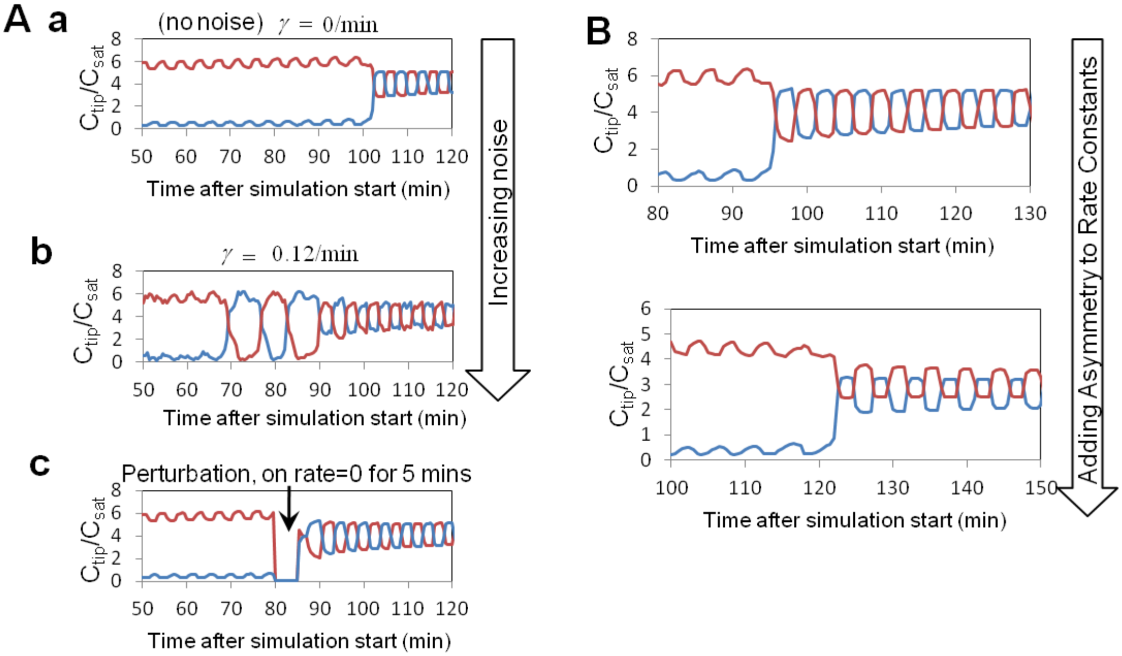

Figure 12. A. Noise and Perturbations Allow State Switching. Trajectories show the amount at each tip versus time using parameters from Table S4, but with $\varepsilon = 0.5$ instead of .5375 to better demonstrate the effects. (a) Trajectories for two tips, without noise in rate constants ($\gamma = 0$) , shows transition to oscillations around a symmetric state. (b) The inclusion of noise (γ =0 .12/min) introduces switching between asymmetric states and leads to an earlier transition to oscillations around a symmetric state. (c) A perturbation that sets the on rate to zero for five minutes leads to an early switch to oscillations around a symmetric state ($\gamma = 0$ was used). **B.** Tips Oscillate around Different Averages when Rate Constants Differ at the Two Tips. For tip 1 (blue), the rate constants are the same as in Table 3. For tip 2 (red) in lower figure, the on rate constants $\lambda^{+}{}_{0}$ and $\lambda^{+}{}_{n}$ are increased by 10% and the off rate constant decreased by 10% with respect to the values in Table 3. Noise in rate constants is not included. In the lower figure, the tips transition from an initial asymmetric state at short times into a less asymmetric state at long times. The change in the rate constants also influences the timing of the transition.

4-3. Testing Predictions of the Model

The experimental tests of the model were carried out in collaboration with Maitreyi Das and Fulvia Verde. We contributed by discussing and recommending experiments, and by analyzing results, but our collaborators cultivated the yeast, did the genetic manipulations, imaged the cells, and carried out all the other physical aspects of the experiment.

According to the mathematical model, cells with similar length may show different degrees of Cdc42 asymmetry (Figure 9 F, Figure 11 C, coexistence region; Figure 20), and changes in abundance or activity of Cdc42, or of its regulators, can shift the system to more asymmetric or symmetric states. The model indicated that cells with a lower rate of Cdc42 activation (or decreased total amounts of GTP-Cdc42 or Cdc42 GEFs) would favor asymmetric states, because the lagging tip would be influenced more severely by the accumulation of GTP-Cdc42 at the dominant tip and by the resulting depletion of the cytoplasmic pool (Figure 20 B and Figure 13 A). To test this, we measured CRIB-GFP tip intensities in *gef1*Δ cells, which lack one of the two Cdc42 GEFs and therefore less active GTP-Cdc42 [91], but otherwise grow at a normal rate. Most (75%; n = 12) *gef1*Δ cells had lower amounts of CRIB-GFP at the new tips in time-lapse recordings (Figure 11 A B). CRIB-GFP tip fractions in *gef1*Δ cells (n = 381) were asymmetric (Figure 11 C), consistent with the model.

From the definition of this model, increasing cell size increases the total amount of active Cdc42 or of Cdc42 GEFs. In the presence of noise, this is predicted to decouple oscillations, because one tip no longer depletes the pool available to the other. To test this prediction, we studied *cdc25-22* cells that delay entry into mitosis, owing to a mutation in a cell-cycle control gene, and become longer than wild-type cells at permissive temperatures (Figure 14 A D E).

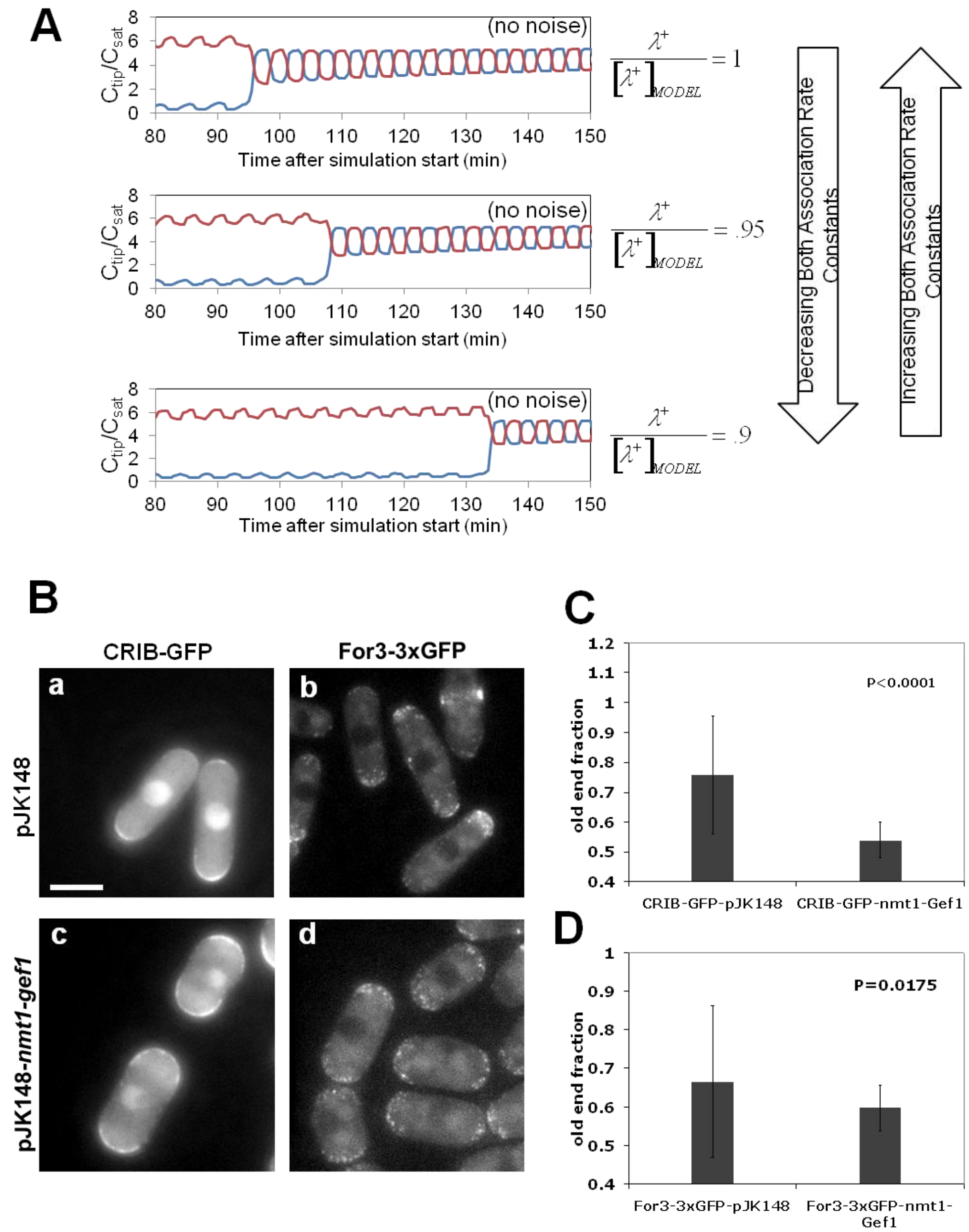

Figure 13. A. Decreasing the association rate of Cdc42 to the tips leads to late transition to symmetric states. Trajectories for two tips as function of changes in the rate constants λ_0^+ and λ_4^+ with respect to those of Table 3 (indicated by subscript “MODEL”), with all other parameters unchanged. Here we eliminated noise to show the effect of the parameter change. **B.** Cells expressing increased levels of Gef1 display more symmetrical CRIB-GFP and For3 distribution. Cells expressing increased levels of Gef1 display a more symmetrical distribution of CRIB-GFP (c) and formin For3p (d) as compared to control cells (a and b) at the old and new ends, Bar=5µm. **C.** Measurement of For3 localization in control and cells with increased levels of Gef1 p= 0.0175, n>30. **D.** Measurement of CRIB-GFP localization in control and cells with increased levels of Gef1 p<0.001, n=40.

To test if Cdc42 GEF availability influences the anti-correlation of Cdc42 oscillations, we measured CRIB-GFP fluorescence in cells that over-expressed Gef1. This eliminated the anti-correlation of CRIB-GFP signal at the cell tips (Figure 11 F G). Increased amounts of Gef1 also led to increased symmetry of CRIB-GFP and Cdc42-target formin For3 [92] (Figure 11 A F, Figure 13 B C D). This agrees with the model, which predicts that increasing Cdc42 activation rate (or total amounts of active Cdc42 or Cdc42 GEFs) (Figure 13 A) leads to more symmetrical GTP-Cdc42 distribution.

Autocatalytic activation within the Cdc42 complex [84,85,93,94] and actin-mediated transport [6] are likely contributors to positive feedback, as in budding yeast [79-82]. Much less is known about negative feedback [89], a required mechanism for oscillations, although another group reported a negative feedback and oscillations in budding yeast while our work on the subject was in press [95]. To identify possible mechanisms for negative feedback in fission yeast, we analyzed CRIB-GFP in morphological mutants [3], including *orb2-34* and *tea1*Δ, which are monopolar [24,96]; *rdi1*Δ (encoding the Rho guanine nucleotide dissociation inhibitor); and *rga4*Δ (encoding the only known Cdc42 GTPase-activating protein) [5,83]. *orb2-34* mutants oscillated asymmetrically, but with a longer period and a decreased amplitude of CRIB-GFP oscillations [3]. Conversely, *rdi1*Δ and *rga4*Δ mutants displayed normal, mostly symmetrical oscillations; *tea1*Δ mutants fluctuated asymmetrically [3].

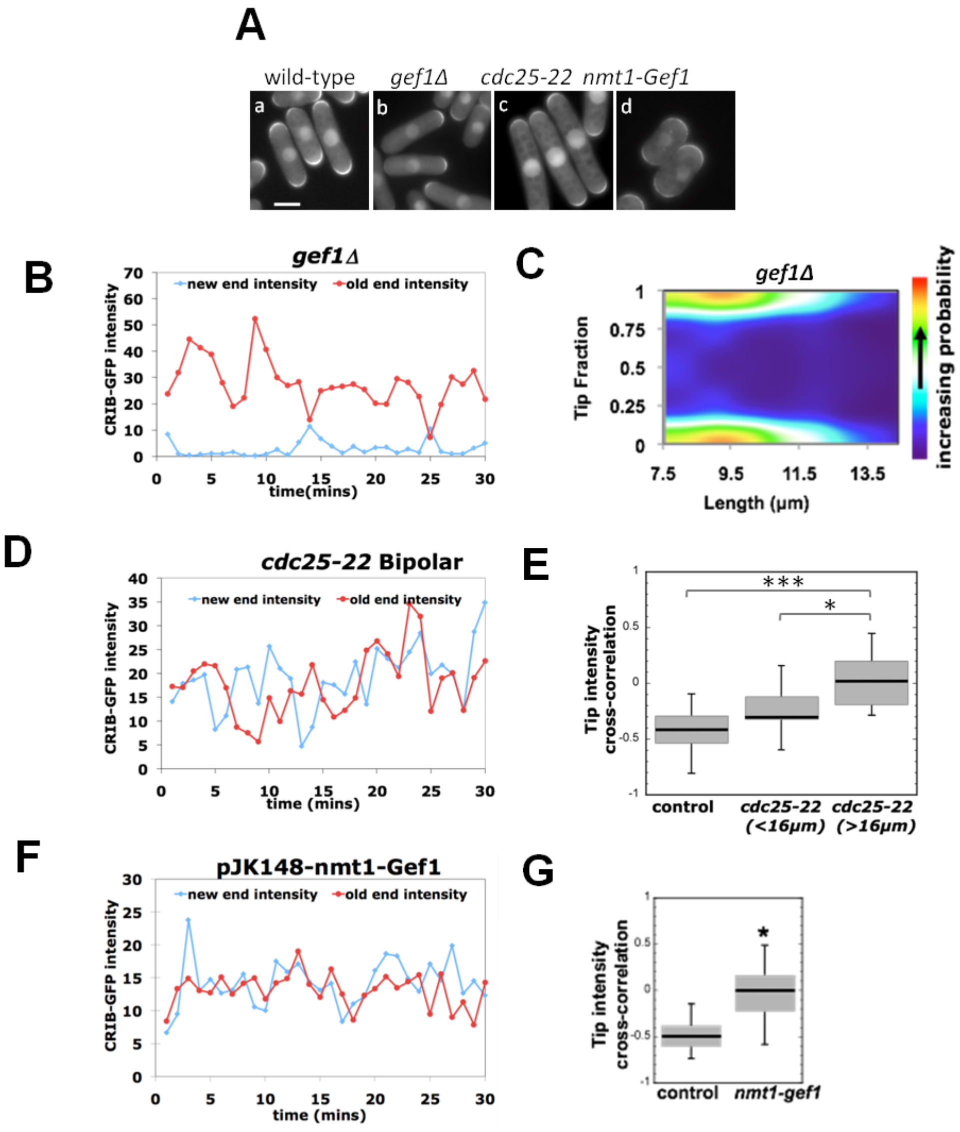

Figure 14. Testing the mathematical model describing Cdc42 oscillations A. CRIB-GFP in wild-type, gef1Δ, cdc25-22 at the permissive temperature (25°C), and Gef1-overexpressing nmt1-gef1 [+thiamine, in YE medium, which contains dextrose (30 mg/ml) and yeast extract (5 mg/ml)] cells. Scale bar, 5 µm. B. CRIB-GFP tip intensities, in a gef1Δ cell (1-min intervals). C. CRIB-GFP tip fractions versus cell length, in gef1Δ cells (as in Fig. 1G, n = 381). D. CRIB-GFP tip intensities, in a cdc25-22 cell at 25°C. E. Anticorrelation of CRIB-GFP tip intensities decreases with respect to wild-type cells and with increasing cell length in cdc25-22 mutants (*P = 0.03, ***P = 0.00039, Student's t test). F. CRIB-GFP tip intensities of cell moderately overexpressing Gef1 (+thiamine, in YE medium). G. CRIB-GFP tip anticorrelation decreases in cells moderately overexpressing Gef1 (***P = 5.7 × 10^{-6}, Student's t test). Whiskers in (E) and (G) indicate the full range of data.

Amounts of CRIB-GFP, Cdc42 GEF Scd1-GFP, and scaffold Scd2-GFP at the one growing tip of *orb2-34* cells were increased compared with the same complexes in control cells ([3] and Figure 15 A B). No localization change was seen for Gef1-3xYFP (yellow fluorescent protein) or Rga4-GFP (Figure 15 C) [83]. The intensity of Scd2-GFP signal [3] or Scd1-GFP at the growing tip in *orb2-34* cells roughly equaled the total fluorescence at both tips (new end plus old end) in control cells [3]. Amounts of total protein were not changed [3]. The implication is that orb2 regulates intracellular distribution of Scd1 and Scd2. In the model, this behavior is expected when the maximal active Cdc42 allowable at each tip increases (Figure 15 E). In mutant cells unable to suppress maximal tip accumulation, the growing tip could function as a sink, trapping Scd1 and Scd2.

To confirm that *orb2-34* mutants remain monopolar because of their inability to redistribute Scd1, Scd2, or other regulators, we destabilized the actin-dependent [6] localization of Scd1 by exposing cells for 10 min to latrunculin A (LatA). In *orb2-34* and wild-type cells, CRIB-GFP, Scd1-GFP, and Scd2-GFP became symmetric in the first hour after LatA removal [3], consistent with reports of brief actin depolymerization promoting bipolar growth in monopolar cells *cdc10*^{ts} and *ssp1*Δ [31,32]. However, 90 min after LatA removal, *orb2-34* cells reaccumulated these markers at one tip, which could be different than the tip originally growing, whereas wild-type cells remained largely symmetric [3]. This agrees with the model's prediction of lack of a symmetric attractor for cells with reduced negative feedback and convergence to a symmetric attractor for wild-type cells after a perturbation (Figure 12 A).

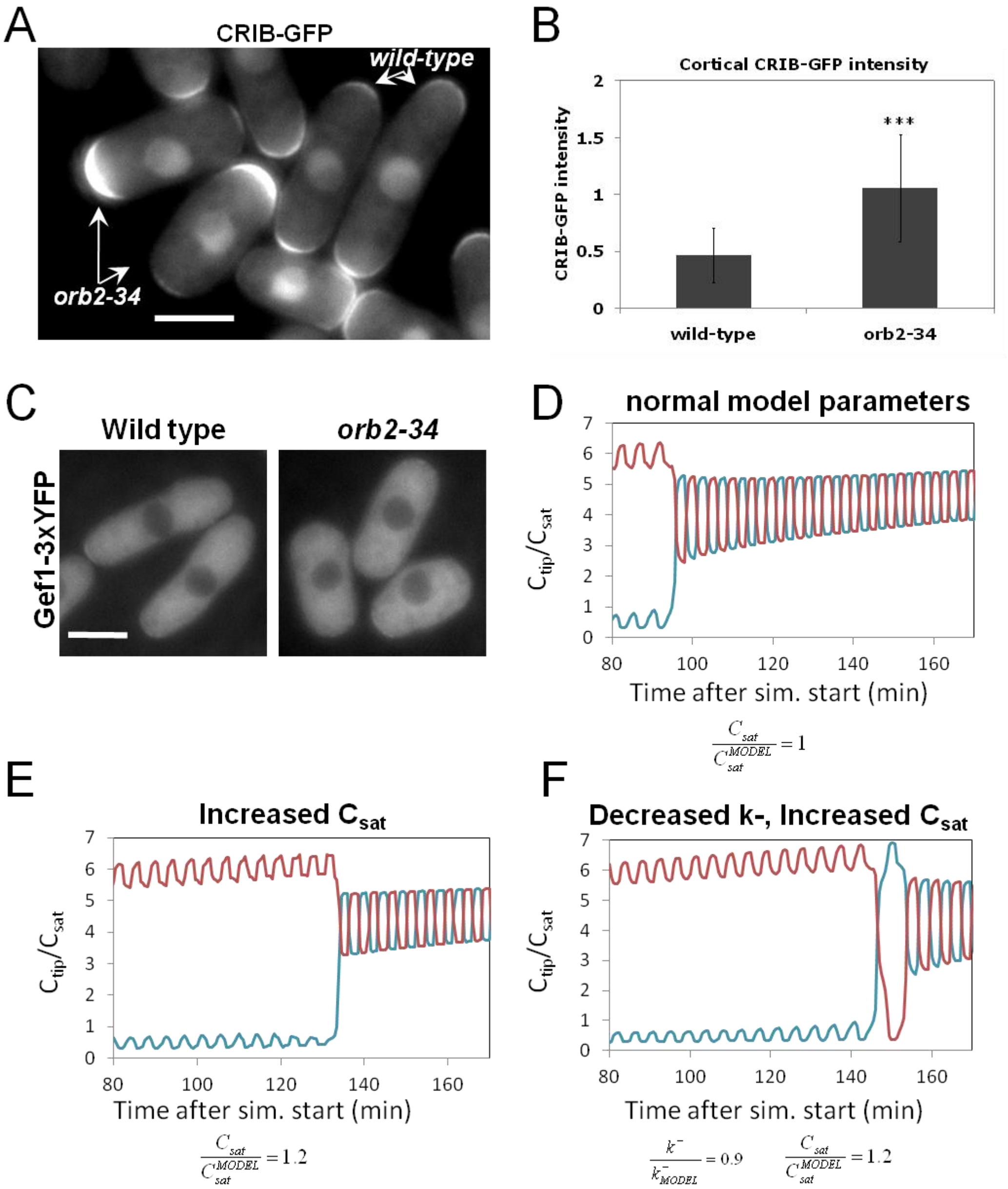

Figure 15. A. Increase of CRIB-GFP tip signal in *orb2-34* cells. CRIB-GFP localization in wild type and *orb2-34* mutant cells. **B.** Cortical CRIB-GFP in wild type and *orb2-34* mutants cells, $p < 0.0001$. **C.** Gef1-3xYFP localization in wild type and *orb2-34* mutant cells. **D-F.** Interpretation by model of CRIB-GFP tip signal increase. The increased monopolarity and increased CRIB-GFP intensity of *orb2-34* cells can be interpreted as an increase in parameter C_{sat} in the model. C_{sat} is the model parameter controlling total tip amount. Trajectories for two tips as active-Cdc42 saturation at cell tip parameter C_{sat} alone increases (E) or a combination of dissociation rate constant k^- decrease and C_{sat} increase (F) with respect to that of parameters in Table S4, (D) (indicated by superscript “MODEL”). Here we eliminated noise to show the effect of the parameter change. We conclude that Pak1 kinase helps decrease C_{sat} in wild type cells (negative regulation).

orb2-34, a mutant allele of *pak1* (also known as *shk1*) [96] contains a point mutation in the Pak1 kinase domain that decreases its activity [3]. Pak1, a Cdc42-dependent kinase [97,98], localizes to tips in an Scd1 and Scd2-dependent manner [6]. Negative regulation of Cdc42 could then be linked to its own activation, as expected from a negative-feedback loop. It might occur through Scd2, a substrate of Pak1 [93], consistent with findings in *Saccharomyces cerevisiae*, where the Pak1 homolog Cla4 negatively regulates the interaction of the scaffold protein Bem1, an Scd2 homolog with Cdc42 GEF Cdc24 [99].

4-4. A Biological Role for Cdc42 Oscillations and Fluctuations

Increased accumulation of Cdc42 GEFs at the membrane, by Gef1 overexpression or loss of negative inhibition (*orb2-34* mutants), dampens Cdc42 fluctuations (Figure 16 A). These mutants are wider, possibly because increasing tip-bound Cdc42 results in growth over a wider area [91] (Figure 16 B C). We suggest that wild-type cells regulate diameter by maintaining Cdc42 activity at the tips within a normal range and activate bipolar growth by Cdc42 redistribution (Figure 17 A). Oscillations and fluctuations may regulate cell morphology and help the switch to bipolar growth. Before NETO, accumulation of Cdc42 at the old end provides a kinetic barrier to bipolar symmetry by depleting the resources available to the new end. Oscillations and fluctuations may relieve this depletion, giving the new end a chance to take off by allowing the system to reach an otherwise inaccessible state of bipolarity (Figure 18 and Figure 19). Mutations affecting Cdc42 regulation may alter the system’s dynamics, by promoting a different pattern of Cdc42 distribution and changing cell diameter and symmetry (Figure 17 B).

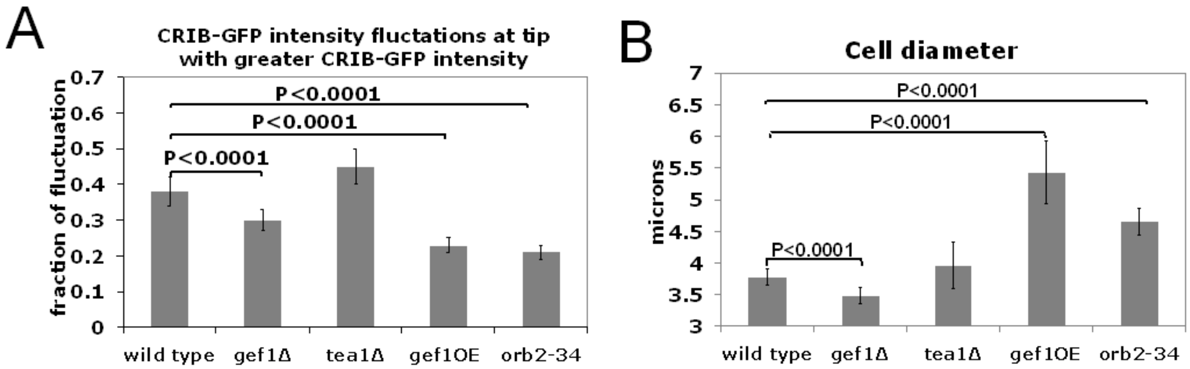

Figure 16. A. Percentage fluctuation of Cdc42-GTP at tip with greater CRIB-GFP intensity in wild type and mutant cells as indicated. **B.** Variation of cell diameter in wild type and mutant cell.

Fission yeast Cdc42 oscillations and fluctuations might represent exploratory behavior, a general strategy among self-organizing biological systems [100]. Despite the associated energy cost, biological systems may benefit because they acquire the ability to quickly reach states that would otherwise be difficult to access. Fluctuations of Cdc42 activity allows fission yeast to rapidly respond to changing intracellular conditions, such as cell volume and length. In an environment with changing external cues, such as nutrient or pheromone gradients, Rho GTPase fluctuations may allow eukaryotic cells to adapt and redirect the direction of growth.

4-5. Comparison to Other Models

The model described here has similarities and differences to the reaction-diffusion model of NETO described by Csikász-Nagy *et al.* ([32], also see section 3-2-1). In both models, symmetric tips compete for a common cytoplasmic substrate. In the reaction-diffusion model, proteins localized at the cell tips promote the conversion of a fast-

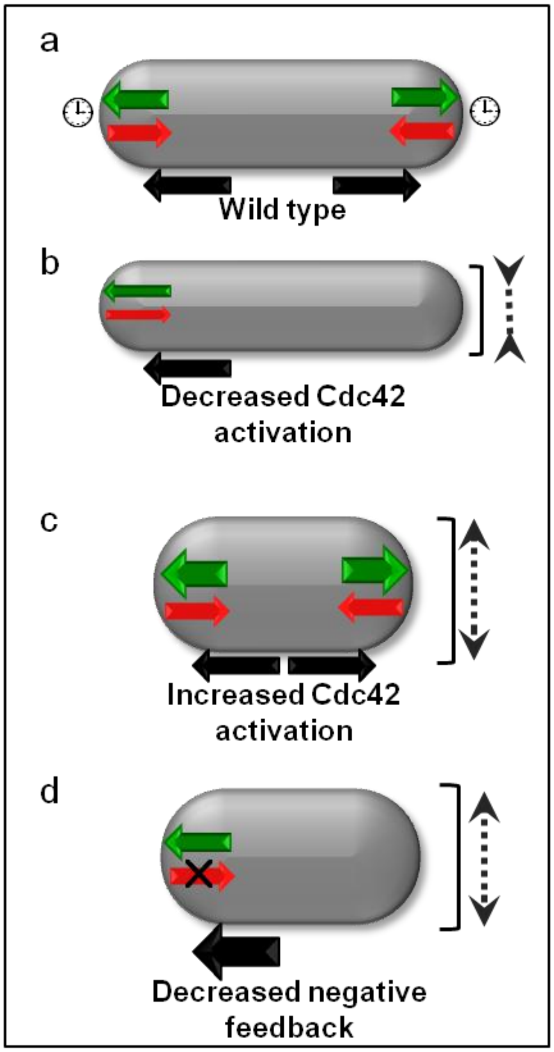

Figure 17. Model of self-organization of Cdc42 at the cell tips and control of cell morphogenesis. **A**. In wild-type cells, Cdc42 recruitment or activation balances Cdc42 removal or deactivation, limiting GTP-Cdc42 tip level and thus setting cell diameter at a normal range. Increased GEF availability promotes bipolar Cdc42 activation at the new cell tip as cell size increases. **B**. Changes in the system's dynamics alter Cdc42 distribution. Decreased Cdc42 activation (*gef1*Δ mutants) increases Cdc42 asymmetry and decreased cell diameter. GEF overexpression increases Cdc42 activation at both tips, which leads to increased diameter. Decreased negative feedback (*orb2-34* mutants) leads to the accumulation of most Cdc42 activity at one single tip and results in monopolar growth. Increased active Cdc42 levels at the growing end results in increased cell diameter.

diffusing cytoplasmic component to a slowly diffusing polymer. This process is autocatalytic. As cells grow, cytoplasmic diffusion limits the rate of substrate delivery to the tips—similar to the saturation mechanism required for bipolarity [see equation (3)]. Because the two models share important similarities (competition, autocatalysis, saturation), both models describe NETO as a transition from monopolar to bipolar states through a coexistence region. This work further includes delayed negative feedback to account for Cdc42 oscillations.

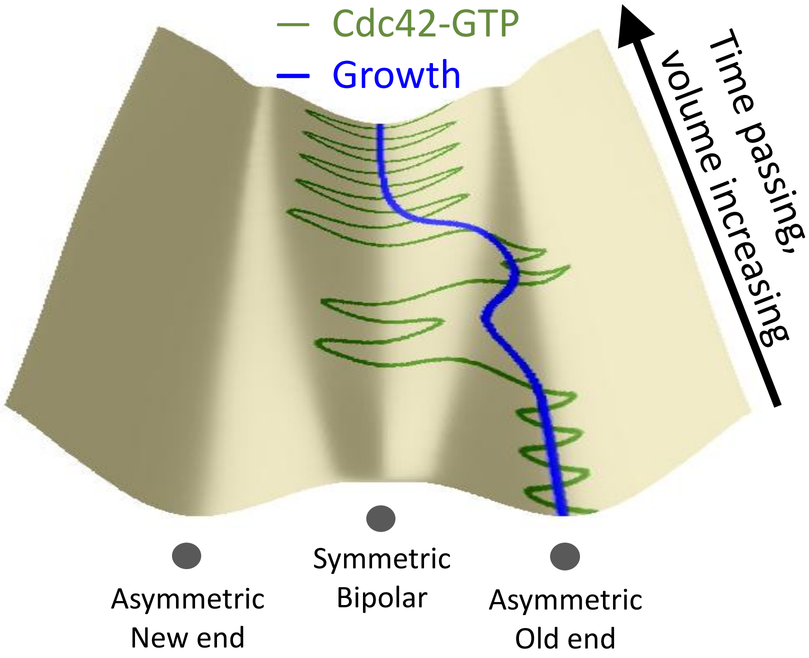

Figure 18. Schematic illustration of the evolution of Cdc42 polarization. During growth, individual cells trace stochastic paths through a polarity landscape that varies from cell to cell, but fits a broad description. Following cell division smaller cell are in an asymmetric oscillatory state with most GTP-CDc42 (green line) at the old end. Autocatalytic accumulation at the old end depletes the active Cdc42 available (or Cdc42 GEFs that activate Cdc42) from the new end, providing an initial kinetic barrier to bipolar symmetry. As cells grow, this landscape changes: the symmetric valley expands and deepens while asymmetric possibilities are progressively lost. Aided by fluctuations and oscillations, the system traverses the waning barrier. The system may revert to asymmetric states, but this is usually temporary—the landscape of the longest cells favors symmetry.

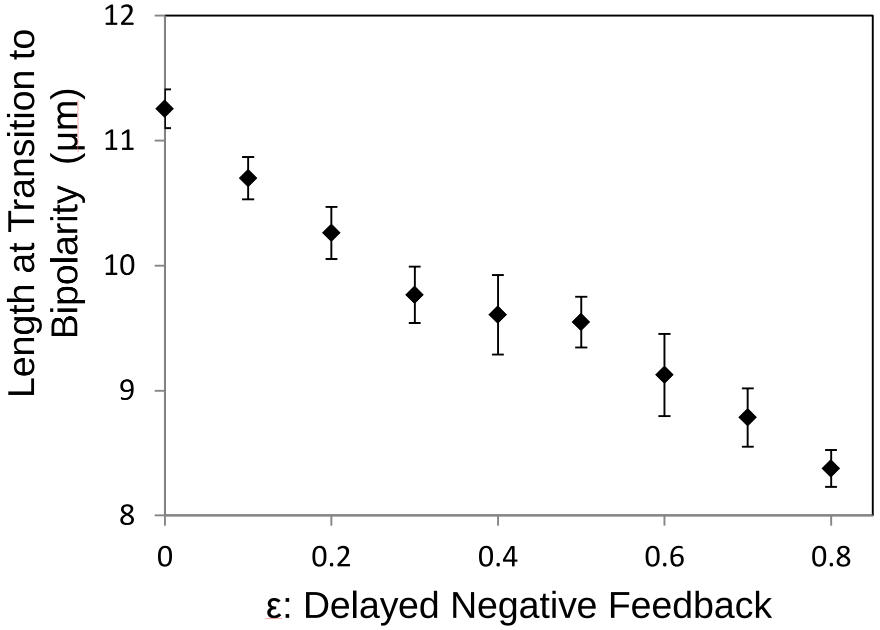

Figure 19. Increasing the strength of delayed negative feedback in simulations increases the amplitude of oscillations and allows faster switching to the symmetric state. Plot: Cell length at time of first switch to symmetric state where the two tip levels first equate, as a function of parameter ε, with all other parameters unchanged (Table 3). Error bars show standard deviation.

Csikász-Nagy *et al*. suggested that the reaction-diffusion model's substrate represents actin monomers, since actin filament nucleation factors at the cell tips convert G-actin to F-actin. But this is unlikely for three reasons. First, filamentous actin moves away from the tip by actin-cable-mediated retrograde flow rather than diffusion [37]. Second, the reaction-diffusion model predicts that actin monomers—the model's limiting substrate—are a smaller portion of the total actin than estimates from experiments [12,37] (and see Figure 4). Third, actin-cable-turnover simulation predicts G-actin cytoplasmic concentration gradients much smaller than those anticipated by the reaction-diffusion model [12,37]. Reinterpreting the fast-diffusing substrate of the reaction-diffusion model as being cytoplasmic Cdc42 and the slowly diffusing polymer as being tip-bound active Cdc42 makes the two models similar. However, here we suggest that factors other than cytoplasmic diffusion may contribute to saturation.

This model for competition described in this chapter has some similarities to the model described by Howell *et al*. [101], which describes mutant budding cells that form two Cdc42 sites for bud growth—and the two sites compete for Bem1 (an SH3-containing protein scaffold that binds Cdc42 GEF Cdc24). However, while this model allows bipolar states, in that case one bud eventually wins.

Just before the publication of our work described in this chapter [3], Howell and others described similar findings in mutant budding-yeast cells [95]. Wild-type budding-yeast cells do not oscillate in this manner, and instead the oscillations are offered as a consequence of negative feedback in the Cdc42 polarization system, and they use modeling to explain that this enhances the robustness of the polarization system to the copy numbers of Cdc42 and Bem1p-complex-related proteins.

After the publication of this work, Cerone and others [102] developed a model that combines elements of the earlier reaction-diffusion model [32] with aspects of the work described in this chapter [3]. Specifically, they use a three-population model of abstract reactants, and the resulting nonlinear system has a similar topological progression to that shown in Figure 20 B. They chose an algebraic form for their equations that allows for more analytic work and investigate the effect of a third growing cell tip, but reach similar conclusions and do not address the role of fluctuations and oscillations.

4-6. Appendix: Correlation of Growth and CRIB-GFP Signal

We calculated the correlation between instantaneous growth rate and CRIB-GFP intensity using sequences of alternating DIC and CRIB-GFP images from Maitreyi Das and Fulvia Verde. We selected cells with a clearly resolved birth-scar position that usually corresponded to a spot with low DIC intensity value. This is a feature on the cell wall that does not move, and it used as a landmark that defines the frame of reference for growth at the two tips. We developed an ImageJ plugin[6] to track the positions of the scar and of cell tips in two kymographs showing the positions of the scar and the tips versus time, respectively. The kymographs were constructed by selecting a small strip along the long axis of the cell running through the scar and tip position, respectively. The plugin located the pixel position of the local intensity minimum within a selected range corresponding to the position of the scar. The position of the tip was found similarly by locating the position of maximum slope in the DIC signal. Growth was evaluated by measuring distance between tips and scar. We discarded those parts of the time courses in which the cells move out of focus and where the cell tip interfered with the signal of neighboring cells. When necessary, we corrected for cell drift using another ImageJ plugin called Stackreg[7]. A least-squares fit of length at seven consecutive time points (6 min total) determined the growth rate at the middle time point. The average of current tip fraction with the previous four tip fractions (4 min interval) determined local tip fraction. In Figure 9 E, we used 0.2 as the value of CRIB-GFP tip fraction that discriminated growth rates in a statistically significant manner.

---

[6] This plugin can be found at http://http://athena.physics.lehigh.edu/cdc42pombe/.

[7] Available at http://bigwww.epfl.ch/thevenaz/stackreg/.

4-7. Appendix: Numerical Solutions for Cdc42 Partitioning Model

After including saturation in Eq. (3), we lose the ability to find algebraic solutions to steady state (another group has since published a more algebraically tractable version of this model and investigated its solutions [102], as discussed at the end of section 4-5). In this section we examine the steady state and dynamical behavior of the model numerically. First, we find steady states of the stationary model by fixing ε=0, which removes the delay term. This eliminates the oscillations, which occur around these steady states, but this allows a systematic investigation of the complete model.

We integrated the equations numerically using NDSolve in Mathematica (Wolfram Research) to find terminal points that correspond to stable fixed points. We used initial conditions distributed randomly throughout phase space. Our criterion for convergence was $\dot{C}_{\mathrm{tip1}}^{2}+\dot{C}_{\mathrm{tip2}}^{2}\leq 10^{-10}C_{\mathrm{tot}}^{2}\min^{-2}$. We verify the sufficiency of this condition by comparing to visual inspection of stream plots, typical examples of which are shown in Figure 20 B. We differentiate between two terminal points if at least one tip amount differs by one thousandth of the total amount. For fixed volume, we find one, two, or three terminal points (circles in Figure 20 B). Symmetry constraints demand that the number of total stable fixed points and the number of symmetric total stable fixed points (blue circles) share parity (oddness or evenness) because asymmetric stable fixed points (red circles) must exist as pairs. In all cases, we found that if a system had two or three terminal points, two of them were asymmetric.

Figure 11 C shows the results for terminal points calculated using the parameters in Table 3. For this parameter set, the system proceeds from monopolar to bipolar steady states through a region of coexistence of monopolar and bipolar states. Figure 20 B (panel II) shows that which steady state is reached within the coexistence region depends on initial conditions (blue versus red arrows).

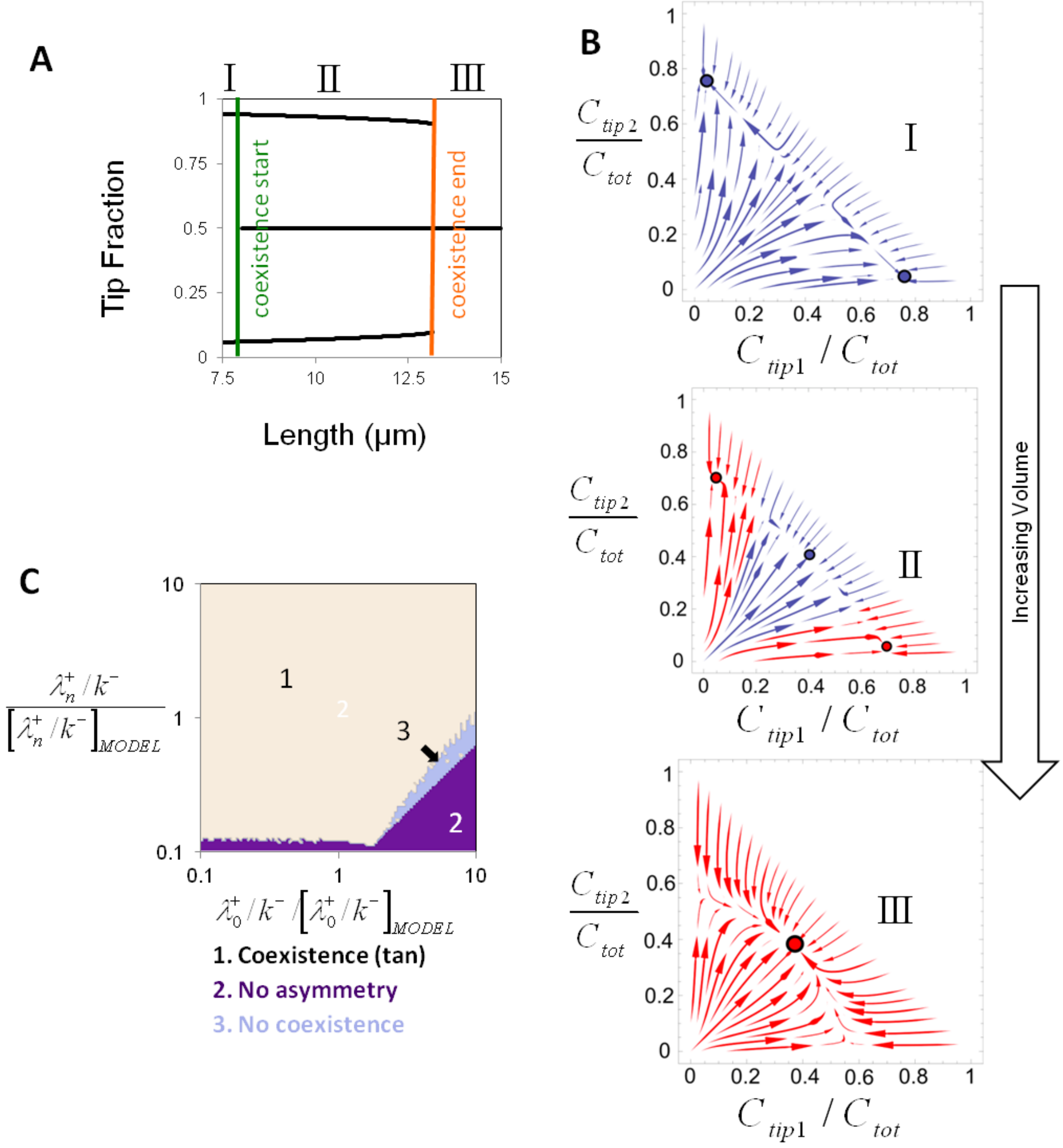

Figure 20. Qualitative dependence of stationary (ε=0) model on parameter values. Varying the system's rate constants (see Table 3) by a factor of ten in both directions shows that the main qualitative feature of the system (progression through asymmetric state, coexistence of symmetric and asymmetric states, and symmetric states with increasing cell length) is maintained. This show that this qualitative progression is not a result of opportunistic choices of rate constants but a result of the form of the equations that represent autocatalytic amplification, competition, and saturation. **A.** Stable tip fractions (black) for increasing total-active-Cdc42 levels, same as in Figure 2C. Vertical

lines indicate the start (green) and end (orange) of the coexistence region, described in supplementary material. **B.** Sample stream plots (arrows indicate time progression of system, their size indicates speed along trajectory). As volume increases, the system allows asymmetric-only states (red) (I), coexisting asymmetric (red) and symmetric states (blue) (II), and symmetric-only states (blue) (III). Red circles represent asymmetrical terminal points; blue circles represent symmetrical terminal points (attractors) of the system. **C.** Existence of asymmetric states and coexistence (found as described in supplementary material) as the two independent parameters (described in supplementary material) are varied from those of Table S4 by one decade (a series of ten) in both directions. The rough boundary and spots near the border between the regions with and without coexistence reflect difficulty distinguishing numerically between the case of having a small coexistence region and that of having none—the latter corresponding to direct transition from asymmetric-only states to symmetric-only states.

To explore the parameter dependence of this steady-state model, we varied the rate constants and examined the system's behavior as $\overline{C}_{\text{tot}} \equiv C_{\text{tot}}/C_{\text{sat}}$, and therefore volume, increases. We found best agreement to experiment for n = 4. For a given n, considering the ratios λ_0^+/k^- and λ_n^+/k^- reduces the number of independent parameters to two and does not affect the steady states—only the time needed to converge to them. We then varied these two parameters (using Mathematica) and determined the properties of steady-state solutions as $\overline{C}_{\text{tot}}$ increases. Figure 20 C shows that three regions in parameter space are possible. For some parameter sets, the system fails to break symmetry, eliminating monopolar possibilities. For other parameter sets, the coexistence region may or may not exist. For cases where the system follows the monopolar–possible-coexistence–bipolar progression, we calculated the dependence of the bounds of the coexistence region on these two ratios (Figure 21).

To find numerical solutions for the general case with nonzero ε, we integrated the equations using the Verlet algorithm in Open-Source Physics (Figure 11 C). Accounting for some of the observations, such as switching between monopolar and bipolar states,

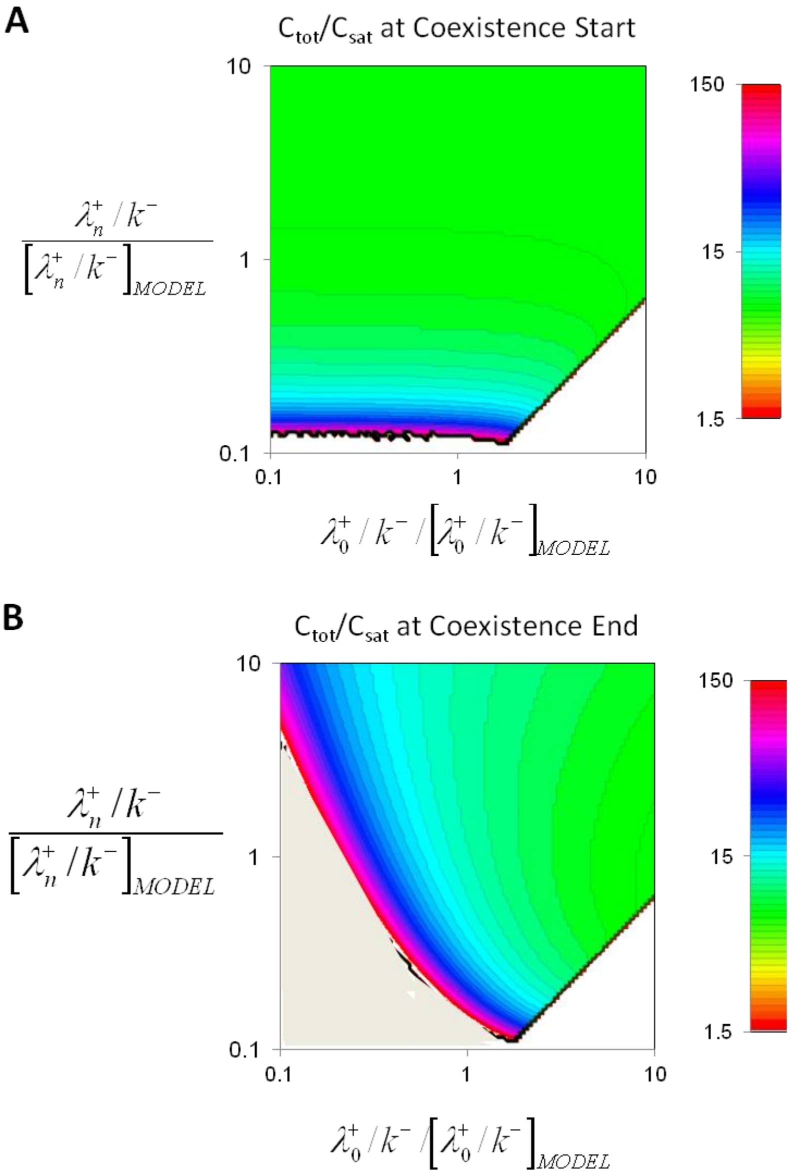

Figure 21. Quantitative dependence of stationary (ε=0) model on parameter values. Varying the system's rate constants (see Table 3) by a factor of ten in both directions shows changes to C_{tot}/C_{sat} at the onset of the coexistence region and exit from that region. **A.** Lowest value of C_{tot}/C_{sat} for stable symmetric solutions, coinciding with the start of the coexistence region, as parameters are changed. **B.** Highest value of C_{tot}/C_{sat} for stable asymmetric solutions, coinciding with the end of the coexistence region, as parameters are changed. Where the values are the same on both panels, no coexistence is possible. In the white region, which corresponds to the purple region on Figure 20 C, the model does not admit stable asymmetric states and therefore has no transition from asymmetry to symmetry. In the gray region, the coexistence region ends for $C_{tot}/C_{sat} >$ 150.

requires adding noise to the model. Many sources of noise are possible. We introduced noise in rate constants to show examples of system behavior. We included Gaussian white noise of amplitude γ in both λ^{+}/V and k^{-} but do not allow them to fall below zero. This method keeps mass conservation and active-Cdc42 amounts cannot become negative. Increasing the magnitude of the noise term by increments shows the effect of noise on the system (Figure 12 A). Increased noise leads to earlier dominant-tip switching and loss of sharpness in the transition to the symmetric state. In Figure 11 B, we used $\gamma = 0.04\ \text{min}^{-1}$. In addition to intrinsic noise, measured distributions differ from the actual active-Cdc42 distributions due to measurement noise. To estimate this effect, we compared tip CRIB-GFP intensity measurements of the same tip taken at one-second intervals and found a standard deviation of about one tenth of the average signal. This indicates that measurement noise is of order 10% or greater.

We tested that oscillations and existence of symmetric and asymmetric states in the model does not depend sensitively on our assumption of identical rate constants at both tips. The model exhibited similar features when the rate constants at one tip were slightly different than those of the second tip (see Figure 12 B where the rate constants at one tip were changed by 10%).

5. Modeling How Membrane-Bound Tip Growth Factors and the Microtubule Cytoskeleton Determine Fission Yeast Cell Shape

Many cells such as fungal hyphae, pollen tubes, and some bacteria grow from their tips by remodeling their cell wall [103-105]. Fission yeast (*Schizosaccharomyces pombe*) also grow this way and, as a well-studied model organism, are good for understanding tip growth and, more generally, the mechanisms of acquisition of cell shape [22,106,107]. Wild type fission yeast cells have a cylindrical shape and maintain a diameter of about 3.4 μm and double in length from approximately 7.5 microns to 15 microns during their life cycle (Figure 22 A). Many fission yeast shape mutants have been identified [108]. Common shape mutants include round cells [108,109], cells with wider or thinner diameter [6,110,111], and branched cells [24,108].

Fission yeast and other eukaryotic tip-growing cells use Rho GTPase signaling and the cytoskeleton to maintain polarized growth [107,112]. Prior work, including that described in Chapter 4, identified two core modules that regulate distinct aspects of fission yeast shape [107,113] (see Figure 22 A): (i) The small Rho GTPase signaling protein Cdc42 and its associated proteins establish a system that influences the width of the growth zone [3,6,114]. Along with its activators and inhibitors, guanine nucleotide exchange factors (GEFs) and GTPase-activating proteins (GAPs) and actin-mediated transport, the Cdc42 system contributes to the formation and upkeep of a growth zone with characteristic width [6] (Figure 22 B C D). By accumulating at the cell tips, active Cdc42 defines an area where vesicle delivery, exocytosis [115], and cell wall remodeling occurs by delivery of cell wall synthases [116,117]. (ii) Microtubules align along the long axis of the cells and deliver landmark proteins to the tips, defining the tip region and maintain a straight central axis [22,34,43] (Figure 22 E F). Microtubules provide a directed track for kinesin-based delivery of +TIP proteins to the cell tip, such as Tea1

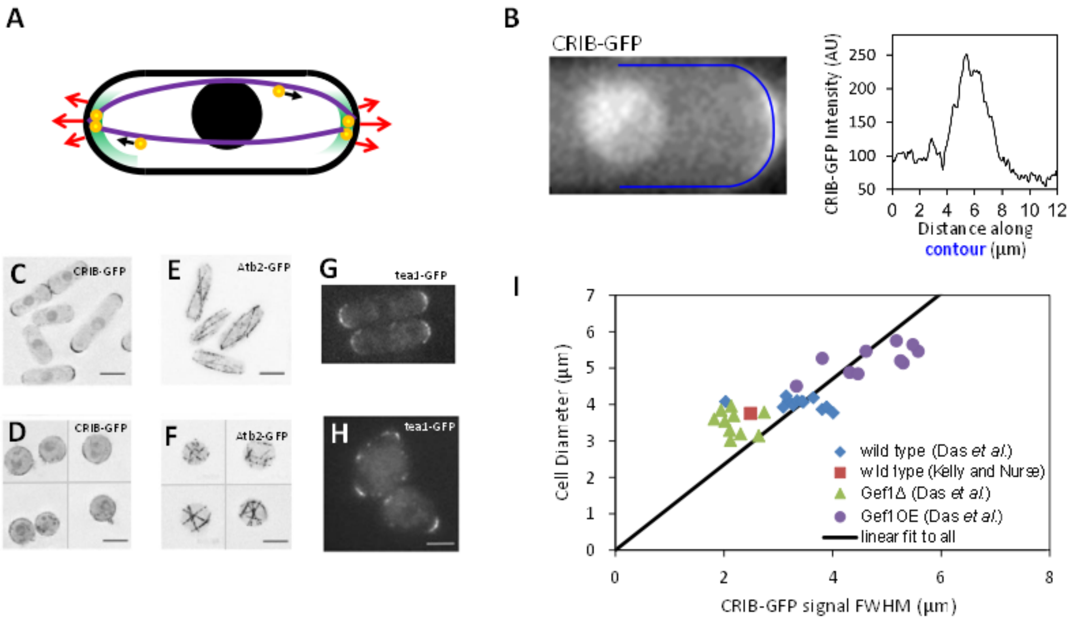

Figure 22. Fission yeast cell shape and regulation by the Cdc42 and microtubule systems. **A.** Schematic of fission yeast. Cell outline and nucleus in black, red arrows indicate outward cell wall expansion during bipolar growth, green represents growth-factor Cdc42 signal, purple shows microtubules aligned to the long axis, orange-and-yellow circles are protein-carrying vesicles delivered along microtubules that mark the tips. **B.** CRIB-GFP (a marker for active Cdc42 [83]) fluorescence localizes at cell tips in control cells. Plot shows intensity along the blue contour in the image. Reproduced from Fig. 1A of [3]. **C.** CRIB-GFP fluorescence in control cells. **D.** CRIB-GFP after enzymatic digestion of the cell wall that causes cell rounding. CRIB-GFP appears to accumulate in patches along the cell surface. **E.** Atb2-GFP fluorescence shows microtubules in control cells. In elongated cells microtubules align along the long axis of the cell. **F.** Atb2-GFP in rounded cells (after enzymatic digestion of the cell wall as in D) shows microtubules with random orientations. **G.** Tea1-GFP, delivered to cell tips by microtubules shows tip-marker location in wild type cells. **H.** Tea1-GFP fluorescence in nearly-round *sla2Δ* cells reveals misplaced tip markers. (C-F: reproduced with permission from [6]; G, H: reproduced with permission from [92]). **I.** Cell diameter versus CRIB-GFP signal full-width half-max (measured as in 1B) for wild-type cells and cells with modulated levels of Gef1, a Cdc42 activator.

[22] (Figure 22 G H). The microtubule system detects shape and marks the cell tips even in mutant cells that lack the ability to direct growth but have been confined to narrow microchannels, and fails to mark the cell tips if physical restrictions force a shape change [34,43,118].

While a large body of experimental work has identified genetic mutations that result in modified cell morphology, such as polarity and width, there has been little modeling work [4] to identify which physical features are required for maintaining cell shape in fission yeast. Cell-scale features such as polarity and width arise from protein-scale cell-wall remodeling and expansion events. Signaling proteins, because they function through short-range interactions, likely operate on a molecular level as well. The specific mechanisms of growth are likely very complex to allow modeling at a molecular level at present; for example, Cdc42 regulates at least two parallel growth pathways [115]. Because of the large separation of scales, however, we anticipate that the cell relies on a modular mechanism that could be approximately described by a coarse-grained model that incorporates the main features of the system. In this modeling study, we explore how the two modules, one based on Cdc42 and another based on microtubules, act in concert to achieve robust regulation—and even recovery—of shape.

We first describe a model for how cell shape depends on the distribution of the Cdc42 signal on the cell tip, and then turn to the problem of how the distribution of Cdc42 could depend on cell shape. We show that stability of cell diameter conditions constrain the possible mechanisms for shape-dependent signal. We show that a model combining Cdc42-signal-dependent cell expansion with microtubule-dependent detection of the long axis of the cell provides a stable system if the Cdc42 signal is shaped by a reaction–diffusion process with an intrinsic length-scale. We discuss the assortment of known shape mutants and show that, given what is known about the mechanistic roles of the missing or affected proteins, they are consistent with the proposed mechanisms of shape regulation.

5-1. Model for Remodeling Under Turgor: From Membrane-Bound Growth Factor Distribution to Cell Shape

Calcofluor staining that marks new cell wall reveals that new material during vegetative growth is incorporated at cell tips [18], where Cdc42 accumulates. Two studies [3,6] using a fluorescent marker for active Cdc42 found an approximately Gaussian intensity profile along the meriodonal contour with a maximum intensity at the cell tip (Fig. 1B). In one of these studies, active Cdc42 distribution in cells that overexpress or lack Cdc42 activator Gef1 show that cell diameter correlates with the width of the active Cdc42 signal profile [3] (Figure 22 I). Since Cdc42 targets actin cables to cell tips [115] and also helps the cell target the exocyst using PIP2 independently of the cytoskeleton [115], and because these two parallel pathways are thought to be responsible for bringing the relevant cell-wall synthases such as Bgs1 and Bgs4 [116,117] to the tips for polarized growth, it is likely that the rate of cell wall expansion depends on the local concentration of active Cdc42. Newly deposited cell wall material will deform under turgor pressure: turgor pressure likely deforms the cell wall within the range of its elastic response, because even cells bent by confinement in stiff microchambers sometimes recover their shape within seconds [118].

Can a model of cell growth where the cell wall is represented as an elastic boundary (the peptidoglycan matrix) under turgor pressure being remodeled at growth zones that polarized cells place at the tips predict the correct cell diameter? What is the relationship between the size and shape of the growth-zone signal and cell shape and diameter? Taking into account the above experimental observations, we developed a model of cell growth in which an elastic boundary under turgor pressure is remodeled at growth zones marked by Cdc42 at the tips. This model is a modified version of a model by Dumais, *et al*. [119] (see 5-5-2 for comparison to other models of tip shape). Specifically we assume that the process of wall expansion can be described by the replacement of strained cell wall material by unstrained material at a rate proportional to the local concentration of a growth factor $\Lambda(s)$, where s is distance from cell tip, see Figure 23. Function $\Lambda(s)$ represents the s-dependent concentration of Cdc42 and other proteins that contribute to wall remodeling. We assume that the material delivered according to $\Lambda(\mathrm{s})$ is able to maintain a wall of constant thickness around the cell, through local cell wall digestion and synthesis processes. In this section we assume that the growth-zone signal $\Lambda(s)$ remains constant during cell growth but in the next section we will consider the effect of the signal being also dependent on cell size.

First, we calculate the stresses, σ_s and σ_θ, necessary to balance turgor pressure P for an arbitrary simple axisymmetric shape where the position of a piece of cell wall is described by the distance to cell tip, s, and angle θ (Figure 23 A). This depends on cell wall thickness, δ, and the principal curvatures, κ_s and κ_θ [120]:

$$\sigma_s = \frac{P}{2\delta\kappa_\theta}\sigma_\theta = \frac{P}{2\delta\kappa_\theta}\left(2-\frac{\kappa_s}{\kappa_\theta}\right). \tag{5}$$

From the elastic stress–strain relationship, which includes the Young's modulus, E, and the Poisson ratio, v, the corresponding strains are:

$$\varepsilon_s = \frac{1}{E}(\sigma_s - \nu\sigma_\theta)\varepsilon_\theta = \frac{1}{E}(\sigma_\theta - \nu\sigma_s) . \qquad (6)$$

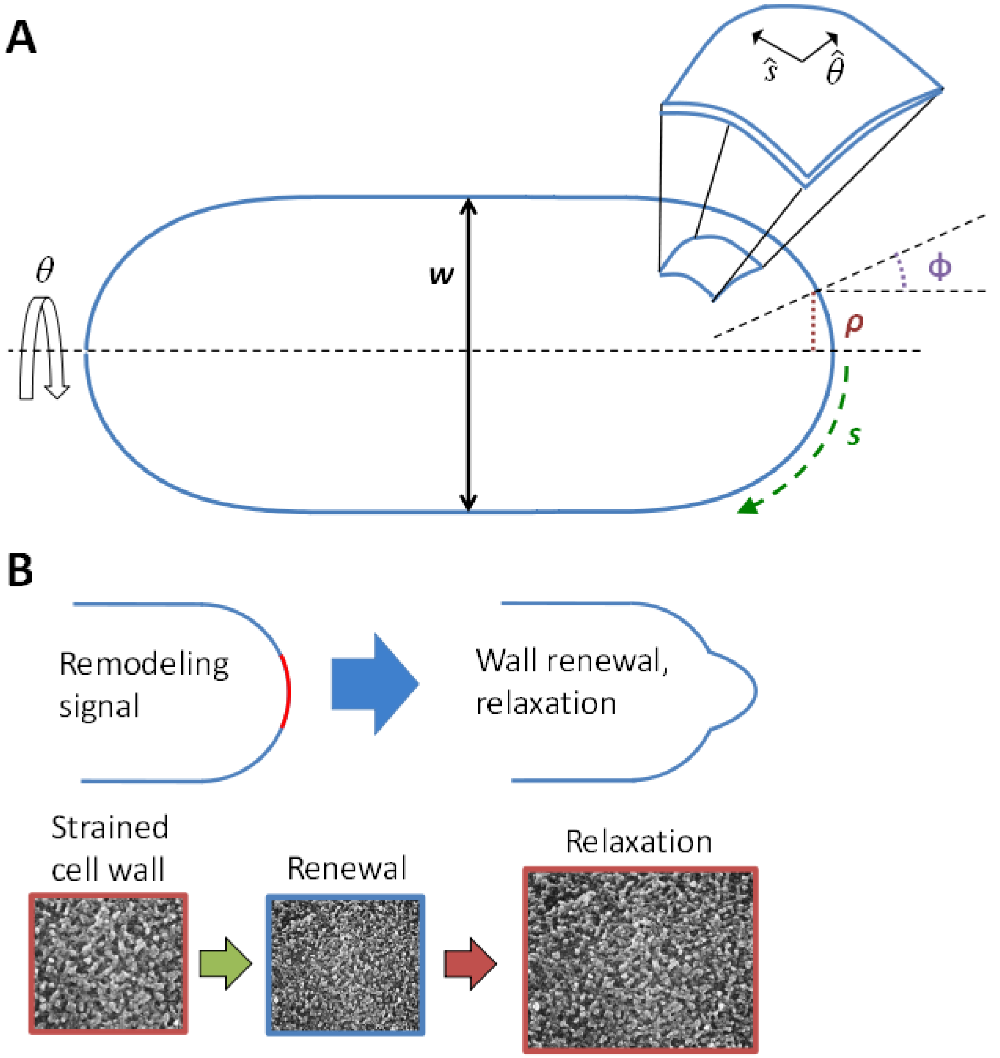

Figure 23. Coordinate axis and model of elastic cell wall remodeled under turgor pressure. **A.** Axisymmetric cell, meriodonal distance *s*, distance from axis of symmetry ρ. Angle φ is the angle between axis of symmetry and the normal to cell surface. Angle θ is measured around the axis of symmetry. Enlarged part of cell wall shows unit vectors $\hat{s}, \hat{\theta}$ along *s* and θ. **B.** Illustration of cell wall remodeling model. Top: Remodeling signal causes part of cell wall under tension to remodel and relax to new shape. Bottom: green arrow shows replacement of strained cell wall by unstrained material; red arrow shows stretching of cell wall under turgor pressure. In the model the two processes happen simultaneously. Electron microscopy images of cell wall reproduced with permission from [121].

We assume that during remodeling strained material is replaced by unstrained material with thickness held constant, corresponding to the wall expanding under turgor pressure in proportion to local strain (Figure 23 B). The signal Λ(s) directs remodeling, and the cell wall expansion rates ξ_s and ξ_θ are the product of the strain and the remodeling rate set by the signal:

$$\xi_s = \Lambda(s)G_{\max}\varepsilon_s \qquad \xi_\theta = \Lambda(s)G_{\max}\varepsilon_\theta \ . \tag{7}$$

Here, we assume that $\Lambda(0) = 1$ and constant $G_{\max}$ is the remodeling rate at the cell tip. Geometrical considerations relate the expansion rate to the velocities along the normal and tangential directions of the surface, v_n and v_t, of a piece of the cell wall with coordinates s and θ [120]:

$$\xi_s = v_n\kappa_s + \frac{\partial v_t}{\partial s}\xi_\theta = v_s\kappa_\theta + \frac{v_t\cos\phi}{\rho}\ , \tag{8}$$

where ϕ is the angle between the normal vector and the long axis of the cell and ρ is the distance to the long axis, see Fig. 2A. The velocities here are with respect to a frame of reference where $v_n(0) = \xi_s / \kappa_s$, meaning the motion at that tip is due to only local expansion.

We solved Equations (5)-(8) numerically (see section 5-6) to calculate steady-state tip shape as a function of growth-factor signal $\Lambda(s)$, see Figure 24. Osmotic pressure P, Young's Modulus E, and the thickness of wall δ combine to form $G_{max} P/E\delta$, a constant that affects the speed of expansion but not the steady-state shape [see text before Equation (9) below]. Therefore, the only factors that determine the change of shape are the geometrical properties of the contour and the signal $\Lambda(s)$. Simulation results starting from a variety of initial contours reach the same steady-state tip shape, showing that the final calculated shape depends only on Λ(*s*).

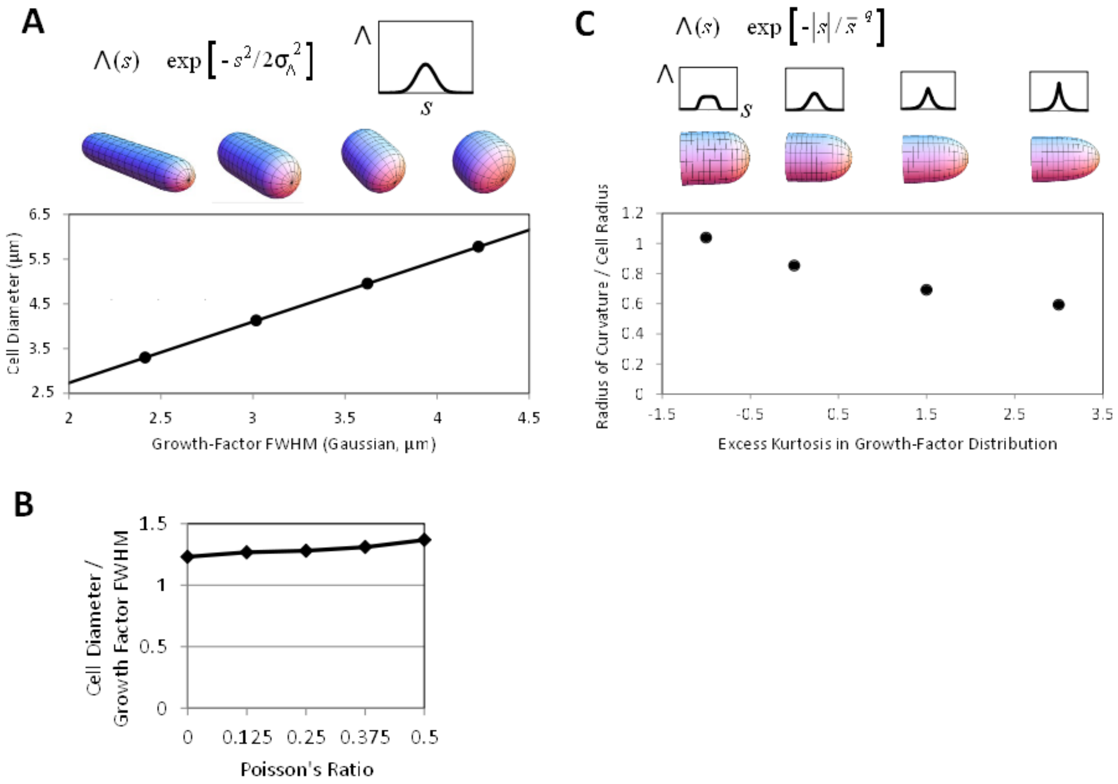

Figure 24. Model for remodeling induced by growth factor yields several predictions. **A.** For a Gaussian growth-factor signal, cell diameter is proportional to signal width as described in the main text. **B.** Effect of changing Poisson's ratio of material inserted on the slope in A. **C.** Using for input an exponential power distribution shows that a pointier or blunter signal gives a pointier or blunter cell. Excess kurtosis measures the peakedness of the distribution. Parameters q and $\bar{s}$ are found numerically to match values of excess kurtosis while keeping the standard deviation constant.

We found that the diameter of the steady state cylindrical projection increases linearly with the full-width half-max (FWHM) of a Gaussian signal (Figure 24 A). Of course this must be the case because the width of the signal is the only length scale in the model, but the model predicts the ratio of the cell diameter to the FWHM of the signal ranges from 1.23 to 1.37 as the Poisson ratio of the material inserted ranges from 0 to 0.5

(the ratio of cell diameter to the standard deviation of the signal σ_Λ ranges from 2.89 to 3.22), see Figure 24 B. This ratio, which comes directly from the theoretical model and is not the result of a fit, is close to 1.19, the value of the slope in the experiments of cell diameter versus CRIB-GFP signal width in Fig. 1I. We also tested how the shape of the growth projection depends on the form of $\Lambda(s)$ by using the exponential power distribution (Figure 24 C). This reveals what we might naively expect: a blunter or pointier signal gives a blunter or pointier cell. In order words, the precise shape of the growth projection changes in the same way the signal does. We do not know of a genetic alteration that produces a drastically non-Gaussian cortical active-Cdc42 profile but recent results suggest that cells lacking Mid1 may be able to grow pointier tips under some conditions [122], which might occur by sharpening the Cdc42 profile through Pom1-dependent regulation by Rga4 [83]. Our results also suggest testing if the ice-cream cone shape observed in some mutants [123] is due to a non-Gaussian Cdc42 profile or else due to a Gaussian Cdc42 profile with cell-length-dependent width.

Further examination of the model, namely by substitution of Equation (7) into Equation (21), substituting Equation (6) followed by Equation (9) into the result, and factoring out physical constants (leaving a dimensionless integral) uncovers a relationship between growth velocity and the parameters of the model:

$$v_{\text{growth}} \approx .058 \frac{P \cdot r^2 \cdot G_{\max}}{E\delta}, \tag{9}$$

where r is cell radius and the numerical prefactor depends on the shape of $\Lambda(s)$ (here Gaussian) and on the Poisson's ratio of the material being inserted. Here we use a Poisson's ratio of 0.5; the value of the prefactor increases by 96% as Poisson's ratio is decreased to zero because the strain approximately doubles. According to Equation (9), growth velocity scales linearly with turgor pressure. This linear relationship agrees with the experimental findings in [118], where a change in turgor pressure was simulated by confining cells in elastic chambers and regulating osmolarity with sorbitol [118]. Using 1.6 microns for the cell radius, a turgor pressure of .85 MPa [118], a cell-wall thickness of 200 nm [124], and a Young's modulus of 101 MPa [118], along with a velocity 2 μm/hr that corresponds to the cell doubling length in its cycle with a constant velocity, we estimate for $G_{\max} \sim 0.33\ \text{sec}^{-1}$. While this is only a rough estimate, this number differs by about one order of magnitude from $0.022\ \text{sec}^{-1}$, an independent estimate of the rate membrane is internalized by endocytosis found by multiplying 25 actin patches per tip [37] by the area of a 300 nm vesicle [40], dividing by the area of a 4.5μm-wide growth zone [3], and dividing by the 20-second lifetime of an actin patch [28]. Perhaps the remodeling of cell wall by cell wall synthases happens at a faster rate compared to the rate of their delivery or removal at cell tips.

5-2. Shape-Dependent Growth Signal and Maintenance of Cell Diameter

The model of the section 5-1 showed that a steady signal for cell wall growth distributed according to the measured active Cdc42 distribution at cell tips can generate a cylindrical extension with a diameter approximately equal to the measured diameter of fission yeast cells. However the spatial distribution of the signal that determines cell growth also depends on the cell shape generated by the signal. Moreover, fission yeast doubles in volume before division and the distribution of growth signal around the cell tip may vary during the cell cycle. For example, the Cdc42 signal changes from monopolar to bipolar distributions; as cells grow the signal oscillates and fluctuates, and may also change in width [3]. How can the cell maintain a stable cell diameter despite these mutual dependencies? In this section we explore the importance of the mutual dependence between signal and shape.

Since the period of Cdc42 oscillations [3], ~5 min, is much shorter than the doubling time, we expect that using the time-averaged Cdc42 profile along cell tips would be a good approximation for $\Lambda(s)$. We anticipate a bigger effect is the dependence of Λ on cell shape. The main feature of Λ that determines the width of the growing projection is its standard deviation, σ_Λ (Figure 24 A). Since wild type cells are approximately spherocylindrical, we approximate the dependence of signal on cell shape by function $\sigma_\Lambda(\overline{w}, L)$, where $\overline{w}$ is the average cell diameter along the cell length excluding the tip cap regions and L is cell length. Here we allow the cell diameter to vary slightly along the cell axis but assume that the average diameter $\overline{w}$ and cell length L are the features of shape that determine σ_Λ (as long as cells remain approximately spherocylindrical).

The diameter of the growing portion of the cell changes according to $\sigma_\Lambda(\overline{w}, L)$. This causes the average cell diameter to change with length, making $\overline{w}$ a function of L. This interplay between the diameter of the cell and the extent of a signal for remodeling can be described by:

$$\frac{d[L\overline{w}(L)]}{dL} = \alpha\,\sigma_\Lambda\left(\overline{w}(L), L\right) \tag{10}$$

In Equation (10), we assume the diameter of the growing portion depends only on the current average dimensions of the cell. Here α is a constant given by the model of the preceding section that ranges between 2.89 and 3.22 for a Gaussian Λ (Figure 24 A B).

Equation (10) is valid for growth from just one tip or from both tips (as long as both tips have the same growth signal distribution). Starting with an initial length L_0 after cell division and initial average diameter $\overline{w}_0 \equiv \overline{w}(L_0)$, integration of Equation (10) gives the average cell diameter $\overline{w}$ when cell reaches length *L*. To maintain constant cell diameter through repeated cell growth and division, the average cell diameter at division must be equal to the initial diameter $\overline{w}_0$. This gives the following requirement:

$$\overline{w}(2L_0) = \overline{w}(L_0) \equiv \overline{w}_0 \ . \tag{11}$$

The diameter of wild type cells does not change significantly throughout the cell cycle, so we can assume that $\overline{w}$ changes by a sufficiently small amount to allow us to perform a linear expansion of $\sigma_\Lambda\left(\overline{w}, L\right)$ in Equation (10). Expanding around the initial diameter $\overline{w}_0$, one has:

$$\begin{aligned} &\alpha\sigma_\Lambda(\overline{w}, L) \approx \alpha\sigma_\Lambda(\overline{w}_0, L_0) + \beta(\overline{w} - \overline{w}_0) + \gamma(L - L_0), \\ &\beta \equiv \alpha \left.\frac{\partial\sigma_\Lambda(\overline{w}, L)}{\partial\overline{w}}\right|_{\overline{w}_0, L_0}, \ \gamma \equiv \alpha \left.\frac{\partial\sigma_\Lambda(\overline{w}, L)}{\partial L}\right|_{\overline{w}_0, L_0} \end{aligned} \tag{12}$$

Substituting Eq. (8) into Eq. (6) and applying the steady state condition, Eq. (7), gives

$$\overline{w}(L) = \overline{w}_0 + \gamma \frac{(2^\beta - 4)L\,L_0 + 2L^\beta L_0^{2-\beta} - (2^\beta - 2)L^2}{(2^\beta - 2)(\beta - 2)L} \tag{13}$$

where the initial width is found by solving the following equation for $\overline{w}_0$:

$$\overline{w}_0 = \gamma \frac{L_0(2^\beta - 2\beta)}{(2^\beta - 2)(\beta - 2)} + \alpha\sigma_\Lambda(\overline{w}_0, L_0)\,. \tag{14}$$

Eq. (10) defines a fixed point for the system: its solution for $\overline{w}_0$ provides the initial cell diameter. Eq. (9) then describes how the average diameter changes with length: it goes through a maximum or minimum, depending on the sign of *γ*. Our linear expansion is self-consistent when parameter $\gamma L_0 / \overline{w}_0 \leq 1$, making the term added to $\overline{w}_0$ in Eq. (9) a small correction compared to the initial diameter (for β=1, the maximum value of the third term in Eq. (9) is ~$0.05\gamma L_0$). The linear expansion in Eq. (8) works as long as the magnitude of β is of order unity, or less, after comparing the magnitudes of the last two terms in Eq. (8).

We have calculated a fixed point for cell diameter (Eq. (10)), but this point is not necessarily a stable one. Performing linear stability analysis of Eq. (6) and requiring that if $|\overline{w}(L_0) - \overline{w}_0| = \varepsilon$ then $|\overline{w}(2L_0) - \overline{w}(L_0)| = \beta\varepsilon < \varepsilon$ leads to:

$$\beta < 1 \qquad \text{(cell diameter stability criterion)} \qquad (15)$$

Thus, the signal that determines cell growth expansion may become more widely distributed across the cell tip with increasing cell diameter ($\beta > 0$), but this dependence has to be weak enough, according to equation (15). Figure 25 illustrates stable and unstable cell shapes depending on β, for the simple case $\gamma = 0$. When $\beta > 1$, the diameter of cells become wider and wider (or thinner and thinner) after each division.

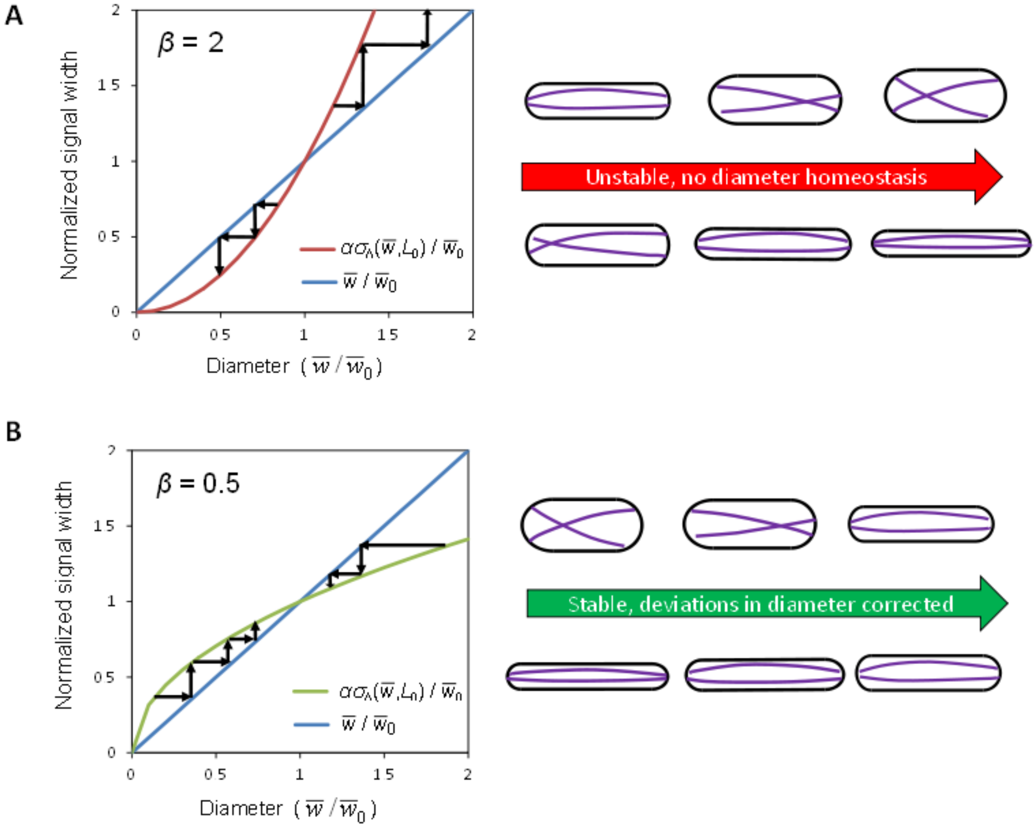

Figure 25. Stable diameter maintenance depends on how growth signal width varies with cell diameter (quantified by the value of β, see Eq. (11)). **A.** Unstable case, $\beta > 1$. Plot shows normalized growth signal width σ_Λ versus cell diameter $\overline{w}$, along with the diagonal.

The intersection between diagonal and σ_Λ curve determines steady state cell diameter $\overline{w}_0$, see Eq. (10) (for simplicity we assume no cell length dependence of σ_Λ, corresponding to $\gamma = 0$). Small perturbations of the diameter from the value of the fixed point are amplified after successive cell divisions. Arrows show how increased (decreased) diameter leads to wider (narrower) growth signal that in turn causes an increased (decreased) diameter. Illustration to the right shows how a mechanism with microtubule tips determining diameter might be unstable: larger (smaller) diameter leads to wider (narrower) microtubule tip distribution, leading to increased (decreased) diameter. **B.** Stable case, $\beta < 1$. Same as panel A but perturbations in diameter are corrected and the fixed point is stable.

5-3. Microtubule-based Distribution of Growth Signal and Stability of Cell Diameter

In fission yeast, the most obvious shape-sensing organelle is the microtubule cytoskeleton (see Figure 22). During interphase, the part of the cell cycle where the cell elongates, microtubules radiate from three to five organizing centers attached to the nucleus [48]. From these centers, approximately two microtubules usually extend tipward in either direction, undergoing catastrophes and rescues [125,126], often spending one or two minutes probing the cell-tip region before shrinking away after a catastrophe. Their alignment appears to depend on geometrical confinement within the cell [34,43]. In addition to centering the nucleus, these microtubules target the delivery of polarity regulators to the cell tips. Microtubules allow motor proteins such as kinesin Tea2 along with plus-tip proteins like Tip1 and Mal3 to deliver cargo such as protein Tea1 to the cell tips [19,127]. Tea1 forms a complex with Tea4 that also localizes formin and actin-cable-nucleator For3 to cell tips [128].

If a narrow tubular shape helps to focus microtubule tips, and if microtubule-dependent polarity effectors direct growth, can the microtubule system be the main mechanism for maintenance of diameter and rod-like shape of fission-yeast? In other words, is a mechanism where the width of the growth signal is primarily determined by the width of microtubule-based delivery able to maintain cell diameter? Indeed, this has been proposed in at least two experimental studies of fission-yeast shape [34,43] . The discussion of the preceding section shows that the feasibility of such a mechanism depends on criteria such as Equation (15) that have not been explored quantitatively.

As a simple, instructive, model of how microtubule-based signal could help control cell diameter, let us approximate the cell as two caps connected by a cylinder of diameter $\overline{w}$. Let us also assume that microtubules deliver cell tip growth proteins approximately uniformly near the cell tip, avoiding the corner region connecting the caps to the cylindrical body by a gap of size w_{ex}. We further assume that the microtubule system can achieve this in a way that signal width σ_Λ is independent of cell length, i.e. $\gamma = 0$. One has:

$$\sigma_\Lambda(\overline{w}, L) = \frac{\overline{w} - w_{ex}}{\alpha(1 - w_{ex} / \overline{w}_0^{\mathrm{WT}})}, \tag{16}$$

where the denominator is a scaling factor that gives the wild type diameter $\overline{w}_0^{\mathrm{WT}}$ as the fixed point in Equation (14). The magnitude of the width of such a growth signal would be consistent with the experimentally-measured Tea1 profile that is approximately Gaussian with standard deviation ~ 1 µm [129]. For this dependence of signal on shape, we find, using Equation (12):

$$\beta = \overline{w}_0^{\mathrm{WT}} / (\overline{w}_0^{\mathrm{WT}} - w_{ex}). \tag{17}$$

This β value is larger than unity for any positive w_{ex}, implying that the signal distribution of the simple model of Equation (16) is an unstable width regulation mechanism. It can be shown that other such simple geometrical models can give values of β that are smaller than unity, but are generally near unity. These β values show that microtubule-only-based models of cell diameter regulation may suffer from instability problems.

Microtubule buckling [47] could focus the microtubules near the cell tip and could reduce the dependence of tip growth factor delivery width on cell diameter compared to the model of Equation (16), thus providing a stable width regulation mechanism. To explore this possibility, we employed a detailed computational model of microtubules proposed by Foethke and others [47] (discussed in section 3-2-3), which treats the microtubules as growing and shrinking flexible rods attached to a spherical nucleus in a viscous fluid by drifting springs (Figure 26 A). We used the two-dimensional version of their model (available at www.cytosim.org*)* that allows extracting locations of positions of microtubule tips. We expect the 2D version to give similar results to the full 3D model, since each microtubule lies approximately on a 2D plane. Microtubule catastrophe rates, in that model, increase with both the length of the microtubule and the force on the tip. Using that model, we changed the diameter and length of the two-dimensional confining cell and tracked the coordinates of many microtubule tips (see Table 4 for model parameters). This gives a profile of where the microtubule tips touch the cell boundary during interphase as a function of cell diameter (Figure 26 B C). Snapshots of simulations in Figure 26 A show configurations of microtubules and the focusing effect of buckling.

As an approximation for the microtubule-based growth signal width $\sigma_{\Lambda}(\overline{w}, L)$ derived from the simulations of Fig. 5A, we examined a model in which the growth factor distribution across the cell tip is equal to the distribution of the likelihood of microtubule tip contact per unit area (see Figure 26 B). Such a model assumes that a localized growth factor signal is delivered in proportion to the time-averaged density of microtubule tips touching the cell membrane. Repeated simulations of microtubule dynamics give a frequency distribution for the location of microtubule tips as a function of the meridional distance (Figure 26 C). This probability density function is fitted to a

Gaussian distribution and the standard-deviation fit parameter σ_{Λ} as function of cell diameter $\overline{w}$ and length is shown in Figs. 5D and E. (Note: Conversion of the distribution

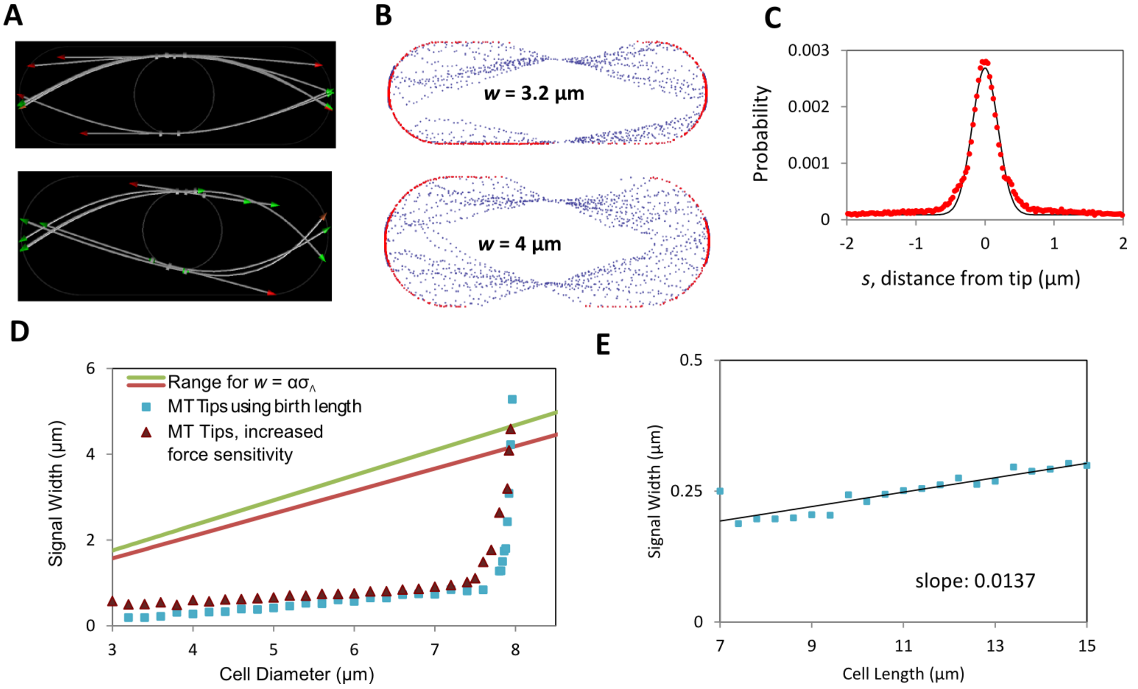

Figure 26. Microtubule-only model of growth signal distribution leads to unstable width regulation. **A.** Snapshots of microtubule distributions using the 2D version of model of Foethke *et al*. [47] for two different cell widths. **B.** Microtubule tip locations (red: touching cell boundary; blue: not touching) extracted from model shown in A. **C.** Time-averaged probability distribution of microtubule tips touching cell boundary as function of distance from cell tip. Continuous curve: Gaussian fit. **D.** Standard deviation of microtubule tip signal from plots as in panel C, versus cell diameter for two parameter sets shown in Table 4. Cell length: 8 µm. The red and green lines show curve $\sigma_{\Lambda} = \overline{w}/\alpha$ using the upper and lower values for parameter α that depends on the value of Poisson's ratio for inserted material (see Fig. 3B). The intersection between the tip signal width curve and the straight lines is the fixed point that determines the cell diameter, see Eq. (10) (here the value of γ is small, see panel E). The graph shows a fixed point at the wrong diameter (near 8 µm instead of ~3.2 µm), and that that fixed point is unstable since $\beta > 1$ at the intersection (similar to Fig. 4A). **E.** Standard deviation of microtubule tip signal varies slightly with cell length. Cell diameter = 3.2 µm. Line shows least-squares linear fit with slope 0.0137.

of Figure 26 C to the corresponding 3D distribution before extracting parameter σ_Λ does not change the following conclusions).

Plot of signal width σ_Λ as a function of cell length in Figure 26 E shows a weak length dependence, $\gamma \approx 0.04$ using the parameters of Table 4. The dependence of σ_Λ on cell diameter is approximately linear for cell diameters smaller than 7 µm, for a cell length 7 µm (Figure 26 D). As the diameter becomes comparable to cell length however, a sharp unfocusing transition occurs and σ_Λ increases rapidly (spike in Figure 26 D). The slope of the linear region is significantly smaller than in Eq. (12); had the σ_Λ curve in Figure 26 D intersected with the green and red lines (which indicate $\sigma_\Lambda = \overline{w}/\alpha$ for the extreme values of the Poisson's ratio, see Figure 24 B) at $\overline{w}_0^{\mathrm{WT}}$ = 3.4 µm, we would have β = 0.25 and a stable diameter regulation mechanism. However, the focusing of the microtubules by buckling is too strong to allow for such an intersection: the values of σ_Λ represent a narrow distribution at $\overline{w}_0^{\mathrm{WT}}$ = 3.4 µm. Instead, the candidate fixed point occurs at very large diameters around 8 µm, within the microtubule unbundling region where β >>1, an unstable case. Changing parameters in the model such as reducing the characteristic force for force-dependent microtubule catastrophes by a factor of ten (Figure 26 D), increasing the hydrolysis rate by up to a factor of five (not shown), or increasing the stiffness of microtubules by up to a factor of ten (not shown) did not modify σ_Λ significantly.

The models of Equation (16) and Figure 26 are not the only possibilities. Additional microtubule-based mechanisms could interpolate between these two models.

For example, if Tea1 delivery happens after some time after first touch of microtubule tip to cell periphery, this would give a larger σ_Λ compared to Figure 26 D. Tea1 tip delivery events do seem to be distributed over a wider area compared to Figure 26 D (see experimental data in Fig. 3E in [129]) but the dependence on cell diameter has not been studied. Overall, it appears that several non-trivial mechanisms would have to be added to microtubule geometric alignment model to achieve the desired effect of a signal with an approximately shape-independent width.

One additional mechanism that would enhance stability is that with a growth signal that can develop its own, approximately microtubule-independent width, likely via a reaction-diffusion mechanism [86,129,130]. In this case the role of the microtubules would be to provide a target for the growth signal by delivering landmark proteins that direct the signal to the cell tip. Such a mechanism would be consistent with experimental observations that show that the lack of fully functional microtubules or missing polarity proteins delivered along microtubules lead to defective cell shapes that still show polarized growth. For example, cells missing Tea1 can grow a third tip out of the center of the cell [24] and mutations of microtubule-associated protein Alp1 can lead to curved cells [131]. Mutations of cysteine 354 in beta-tubulin change the overall rate of microtubule growth, shrinkage, catastrophe, and rescue [132]; these changes lead to partially misplaced Tea1 and often to growth from the side of the cell [132]. These cells are also late or defective in initiating bipolar growth, suggesting that the landmarks are necessary to place a new growth site as the cell becomes longer and more mature [132]. Spheroplasts treated with microtubule inhibitor MBC are able to polarize and extend growth projections [114]. Membrane-bound Mod5 appears to cooperate with Tea1 to maintain a robust Tea1 distribution [129]. Related work in budding yeast also supports the ability of the Cdc42 system to break symmetry and establish a polarized growth zone independently of microtubules [86,87].

In the next section we show how a model with growth zones, microtubules, and landmarks can not only explain stability of fission yeast cell diameter but also several features of cell shape in wild type and mutant cells.

5-4. Model for Shape Maintenance by Growth Zones, Microtubules, and Landmarks

To investigate how the microtubule and tip signal growth components of shape maintenance fit together, we built a qualitative model that includes signal-dependent growth, diffusing growth zones with a native width as from a reaction-diffusion system, and an axis-sensing microtubule system that delivers landmarks to the cell tips (see Figure 27). Then we explored the parameter space of the model. Here we show that changes to the focusing of the microtubules and the dynamics of the Cdc42 system can lead to bent or bulged shapes, and we describe how many of the known aberrant shapes can be understood within this modeling framework.

In the model we assume that the landmark proteins, such as Tea1, that are delivered microtubule system provide an attractive potential $U(s)$ at cell tips for the center of the Cdc42 growth zone signal (purple zone in Figure 27 A). This potential, reflecting the interaction between Tea1, Mod5 [129] and associated proteins on the cell membrane, that we approximate as a Gaussian distribution, has width σ_{MT} and depth U_0 that we treat as an independent parameter. We assume that the Tea1/Mod5 interactions allow σ_{MT} and U_0 to be independent of cell length and diameter. While the molecular basis of the interactions between this Tea1 zone and the Cdc42 system have not been

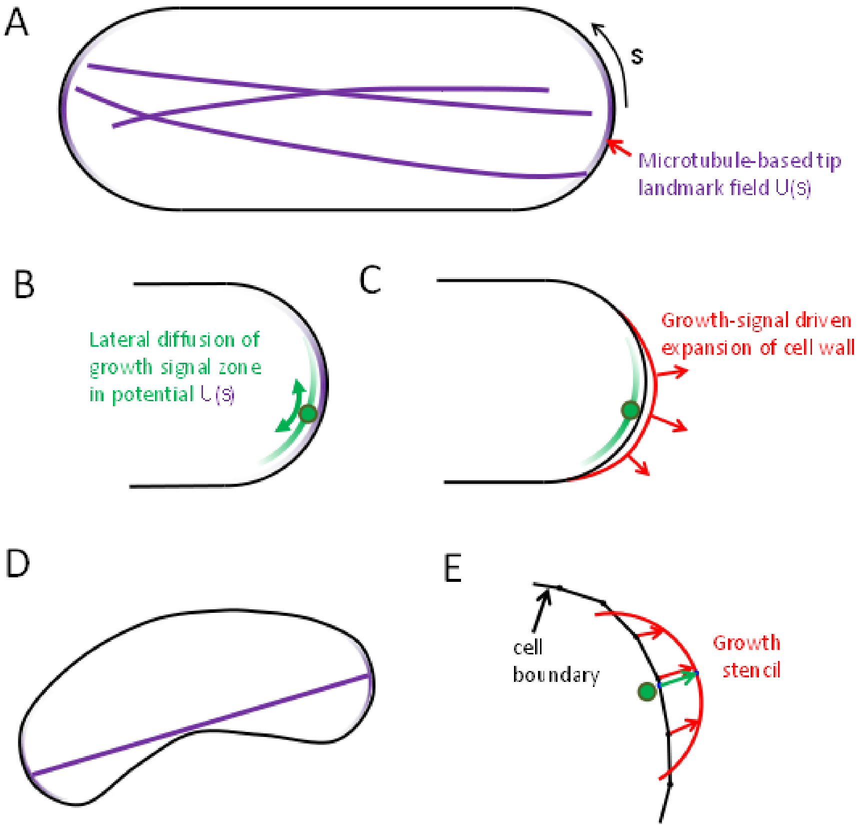

Figure 27. Model with growth zones, microtubules and landmarks (see main text and Materials and Methods for detailed description). **A.** Model schematic shows cell outline (black) and the potential $U(s)$ defined by the microtubule ends at cell tips (purple gradients). **B.** Center of diffusing growth zone (represented by a green circle) moves diffusively in the microtubule-tip-based potential. **C.** Growth signal (green gradient) leads to local cell wall expansion. **D.** A straight line (purple) representing the microtubule system extends towards local length maximum to define the center of the $U(s)$ potential. **E.** Points on the cell outline move towards the cell stencil (red) centered at the position of the center of the growth signal and oriented normal to the cell contour.

established [92,128,133], we anticipate that this interaction can be captured by a diffusion in a potential process: the constant assembly and disassembly of the Cdc42 cap would lead to random motion of the center of the growth signal zone that is biased towards the minimum of the potential. This diffusion process can be quantified by one additional parameter, D_{gz}, the intrinsic diffusion coefficient of the center of the Cdc42 signal. The standard deviation of the growth signal $\Lambda(s)$, that comes from the Cdc42 reaction-diffusion system and its regulators is fixed to be σ_{Λ}, independent of cell shape. The phenotypes of wider or narrower diameters seen in Cdc42-regulator deletion mutants such as Rga4Δ and Gef1Δ [6] or overexpression of Gef1 [3] would correspond to different σ_{Λ} but here we do not model the mechanisms determining σ_{Λ}.

For simplicity, we study the model in two dimensions. We anticipate that features of the model, such as how far from the tip the growth zone normally diffuses and how often it escapes the microtubule-based potential at the tip, do not depend qualitatively on the dimensionality. A 3D model could have additional features such as allowing corkscrew-shaped cells that are neglected here. We developed a version of the 3D axisymmetric growth model that could be plugged into the 2D model that uses a protruding stencil for a growth projection from a 2D contour (see Figure 27 and section 5-4). The stencil size scales to match the width of a growth zone. We used a stencil model since a direct conversion of the model of Fig. 2 to two dimensions does not work because an elastic boundary under turgor pressure in 2D always becomes circular. The growth stencil has the shape of a cross-section of the 3D tip shape derived earlier for a Gaussian growth-factor signal (Figure 24 A). Instead of calculating the shape change based on remodeling under pressure, the outline deforms to accommodate the protrusion of the stencil. The 2D model allows us to examine shapes that would not be axially symmetric without the added complication and computation of a fully three-dimensional model.

Finally, we assume that the microtubule system marks the two most distant parts of the cell that correspond to the two cell tips. This is can be represented in the model as a line from one point on the cell boundary to another. During every step of the simulation, the line representing the microtubule system repeatedly attempts to increase length by small movements of these two points. This process finds a local maximum of distance between two points on the outline, and for simple shapes such as a rectangle capped on opposite sides by semicircles the process finds the global maximum of distance between points on the entire boundary. The ends define centers of potential $U(s)$ on the cell boundary for diffusing growth zones.

To explore the family of shapes produced by the above model we started from a 2D cross-section of the cell shape calculated in the 3D model (Figure 24 A) and length 8 μm. This shape was evolved until the long axis of the cell had doubled. For cells that did not elongate linearly, we ended the simulation at three times the time it would take the long axis to double were the cell growing straight. We simulated cells with either one or two growth zones since some shape mutants grow in a monopolar manner (single growing tip, such as *tea1Δ* [24]) while others are bipolar (two Cdc42 zones, such as some *for3Δ* cells [13]).

Simulations reveal three families of shapes: straight cells, bent cells, and bulged cells (see Figure 28, Figure 29). For small diffusion coefficients and narrow microtubule-based potentials, cells grow approximately straight (region I on Figure 28, Figure 29). As the potential defined by the microtubule becomes wider, if the diffusion coefficient is large enough that the growth zone can move away from the tip during the lifetime of the cell, the cell often grows away from the axis of the cell, resulting in a bent final shape (region II on Figure 28, Figure 29). Finally, as the diffusion coefficient becomes large enough that the potential no longer confines the growth zone or the potential becomes so

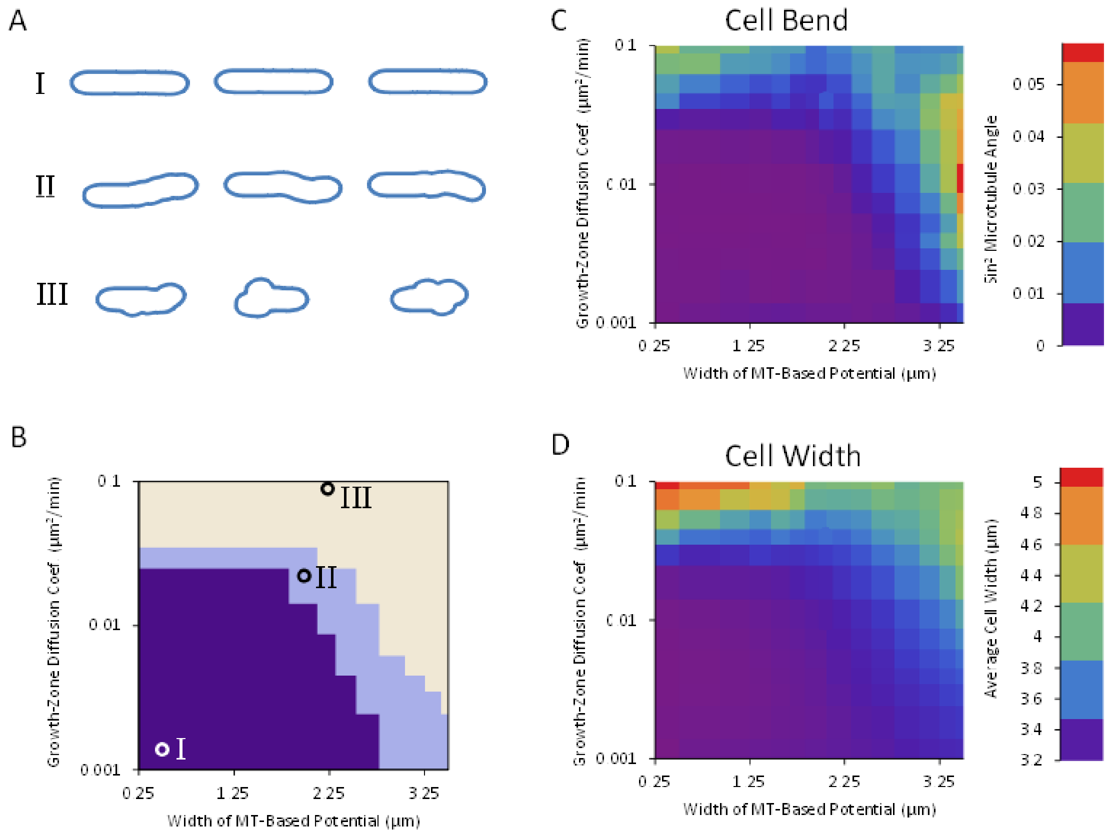

Figure 28. Two-dimensional model with one growing tip generates three families of shapes. **A.** Examples of simulated cell outlines from the three regions in parameter space show occurrence of: (I) straight cells, (II) bent cells, and (III) wide cells. Cell shapes were generated by starting from an outline of a 8 µm long cell with tips shaped according to the model of Fig. 6 and a growth zone placed at one tip. The model was evolved until cell length doubled or thrice the amount of time necessary for a straight-growing cell to double had elapsed. **B.** Regions of different shapes as function of growth zone diffusion coefficient D_{gz} and standard deviation of microtubule-based potential σ_{MT}. Circles on plot indicate parameters used for the shapes in panel A. For the definition of the regions, see Materials and Methods. The depth of the potential was $U_0 = 0.2$ µm^2/min, a value that shows a range of model behaviors. If the potential is very deep, any diffusion coefficient that allows the growth zone to escape from the tip also allows it to explore the side of the cell. If the potential is very shallow, a diffusion coefficient that allows the growth zone to be confined also precludes exploration of most of the cell boundary during the growth phase of the cell. **C.** Cell bend, measured as squared sine of angle between initial and final cell axes as described in Materials and Methods as a function of the same parameters as in panel B. **D.** Cell width, measured as described in Materials and Methods, as a function of same parameters as in panel B.

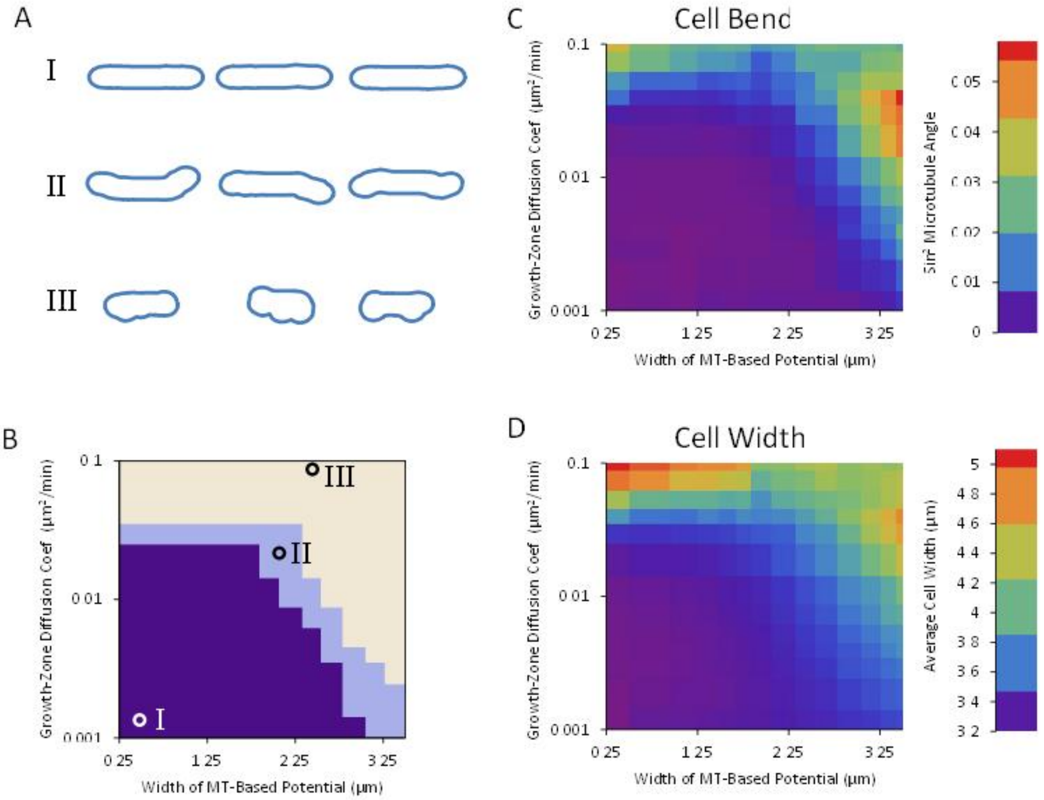

Figure 29. Two-dimensional qualitative model with two growing tips generates three families of shapes. Same as Figure 28, but with two growing tips.

wide that it extends well beyond the cell tips, the growth zones can explore the entire surface of the cell and the cell develops bulges and diameter increases (region III on Figure 28, Figure 29).

Both the bent (region II) and bulged (region III) cell morphologies have been observed by experimentalists, as we will discuss in the remainder of this section. The ban mutants become banana shaped [108] and our results suggest that this could be the result of the combination of wider Tea1 and other landmark protein distribution with a fast diffusing Cdc42 cap. Thus, they may provide an experimental window into the interrelationships among growth, Cdc42 signaling, and the microtubule system. We note that our simulations show equal numbers of S-shaped and banana-shaped cells while prior reports show primarily banana shapes [108]. One possibility is that the model of Fig. 6 is correct in that initial cell bending is due to diffusing growth caps. Aspects of the microtubule system not included in the model might subsequently preferentially stabilize banana shapes as compared to S-shapes: for example, U-shaped buckled microtubules are more likely to occur as compared to S-shapes [47] but the model of Fig. 6 does not account for microtubule buckling. Microtubules in the *ban5-3* mutant tend to be shorter during interphase [108], and the shape of these cells often includes sharp bends. Since the *ban5*-3 mutation is on the gene encoding for alpha tubulin Atb2 [134], the resulting cell shape can be attributed to a failure of the microtubule system to reach and indicate the tips for growth, consistent with our model. Another possibility is that microtubule buckling is the primary cause for some of the banana shapes, rather than growth cap diffusion: the landmark distribution generated from buckled microtubules would lead to banana-shaped cells. Images of *ban2-92, ban3-2,* and *ban4-81* mutants do show a buckled microtubule bundle on one side of the cell [108] but what is cause and effect is unclear. The mechanism behind shape in these ban mutants might act through components of the microtubule organizing centers attached to the nucleus [135]. We propose experimental measurements of active Cdc42 zone diffusion in the ban mutants to help separate cause and effect in these shape mutants.

Long cells blocked in G2 also become curved in a way similar to the banana mutants [32,108]. This could be related to a cell-length limit for the normal response of the microtubule system: if mictrotubules are unable to extend all the way to cell tip, this might give rise to a wider and/or shallower potential $U(s)$.

Bulge-shaped cells have also been observed in Mid1 mutants [122,136] and in the *sla2*Δ cells shown in Fig. 1H [137]. We suggest these shapes might be related to a rapidly diffusing growth zone in combination with defects in microtubule organization. Alternatively, unregulated random nucleation, growth and disassembly of Cdc42 growth zones (as occurs during mating [138]) could explain these shape mutants. To date, bulged mutants have not been explored as much as other aberrant shape phenotypes, possibly because such a trait may be caused by factors other than mutations.

Here we did not address T-shaped cells [24]. These phenotypes may occur because of a failure to initially place the growth zone at the tips.

5-5. Discussion

5-5-1. Summary of Models of This Chapter

The work presented in this chapter addresses three questions: (1) Can a physical model for how fission-yeast cell shape could depend on a cortical signal reproduce the observed cell diameter and tip shape using the measured active Cdc42 profile? (2) What are the ramifications of a shape-dependent signal for growth, and can a mechanism where the width of the tip growth signal is determined by microtubule focusing lead to stable regulation of diameter? (3) Can a number of abnormal fission yeast shapes be understood in terms of disruptions to a few interacting modular components that link the cytoskeleton to Rho GTPase signaling?

To address the first question (1), we developed a coarse-grained mathematical description of the cell boundary as an elastic shell shaped by turgor pressure (Figure 23 A), and of how the shape of this boundary would change due to continuous renewal of the boundary material (Figure 23 B). Results from this model include a rate of signal width to cell diameter in accord with experimental results [3,6] (Figure 24 A).

To address the second question (2), we give an account of how feedback between a growth signal and cell shape might affect diameter. Results from this model include a condition for stable diameter regulation [Equation (15), Figure 25], and data from a detailed microtubule simulation ([47], Figure 26) suggesting that simple feedback between growth signal and cell shape through physical exploration by the microtubules may not be sufficient to establish a constant cell diameter.

To address the third question (3), we describe a qualitative model that incorporates components of fission-yeast shape regulation to provide a basis for understanding shape abnormalities (Figure 27). The model includes coarse grained versions of the microtubule-dependent tip-sensing mechanism, the landmark proteins delivered by motor proteins along those microtubules, and the active-Cdc42-dependent growth described in the first part (1). Results include an exploration of model parameters to show the shape families that arise due to alterations of the distribution of the landmark proteins or the diffusive speed of the Cdc42-dependent growth zones.

As a whole, this theoretical work describes a framework for understanding how shape is regulated and maintained in fission yeast, and motivates experimental investigation into the physical components of the cell that correspond to mechanisms of the model.

5-5-2. Comparison to other models for tip cell wall growth

Our model of signal-dependent growth relates to previous models of tip shape in other cell types. We note that there are some differences between fission yeast and other tip-growing cell types. Pollen tubes, for example, secrete pectic polymers to build their cell wall at the cell tip and they are cleaved of methyl groups as they mature [139,140] while fission yeast lacks pectin and its cell wall contains primarily glucan and chitin [141,142]. Vegetative fission yeast also does not have a Spitzenkörper [103,143], the organizing center for vesicle delivery in growing tips of fungal hyphae, so our model differs from models that have investigated the consequences of Spitzenkörper-dependent tip growth [144,145].

Our model is most closely related to the model of Dumais *et al*. [119], who modeled the cell wall of tip-growing plant cells (such as elongating root hair cells of *M. truncatula*) as a thin viscoplastic shell. Their model belongs to a class of models for tip growth that rely on gradients of mechanical and viscous properties of the cell wall along the cell tip [144,146]. In Dumais *et al*., the mechanical properties of the wall—extensibility, yield stress, and Poisson's ratio—vary with distance from the tip and their interaction gives rise to shape. The extensibility function plays a similar role to our $\Lambda(s)$ and both models share the same algebraic expressions for elastic shells [120]. In Dumais *et al*., delivery of material is assumed to be tuned to maintain a constant wall thickness. Here we assume delivery is proportional to $\Lambda(s)$ and that the material delivered is able to maintain a wall of constant thickness. While the equations that describe the steady state are mathematically very similar, here we explicitly link wall expansion to delivery of wall material (so we predict that in the absence of delivery expansion would stop, since we assume the wall is elastic). We also assume a different expansion rate: in Eq. (3) we assume the expansion rate is proportional to local strain while Dumais *et al*. assume that the strain rate (corresponding to ξ here) is distributed according to a local energy minimization.

Campas and Mahadevan [147] identify two length scales in tip growing cells, one describing the distance away from the tip at which the polymers of the cell wall become increasingly cross-linked causing a transition from a fluid to a solid wall (in pollen tubes this depends on pectin methyl-esterases and their inhibitors) and another describing the distance from the tip where the rate of material deposited to the wall falls off. These two length scales lead to a spectrum of possible cells diameters and shapes where the radius of curvature at the tip and the radius of the cell body differ. Here we assume cell wall expansion is linked to delivery of wall material through $\Lambda(s)$. Thus, changes of tip shape and diameter rely on different $\Lambda(s)$ profiles.

Fayant *et al*. [140] developed a finite element model for growing lily pollen tubes and use the model alongside experiments to identify a cell-wall component responsible for changing the mechanical properties of the wall. In that model, the Young's modulus varies with the angle between the tip and the long axis of the cell, reflecting a continuous maturation process as wall material moves backward from the tip. Experiments reveal this maturation process to be the esterification of pectin. They assume exocytosis acts to maintain constant cell-wall thickness during expansion.

The rod shape is not exclusive to eukaryotes: a few well-studied bacteria maintain a shape that is similar to that of fission yeast with growth occurring along the cylindrical cell body or at cell tips, depending on the organism [148]. *B. subtilis, E. coli,* and *C. crescentus* grow by patterned insertion of peptidoglycans into the sidewall using a MreB-dependent mechanism and some disagreement remains as to whether this operates by circumferential motion of a complex including MreB [149,150] or as a consequence of a helical MreB structure [151,152]. Huang, Wingreen and others used molecular-level models to describe the growth of Gram-negative bacteria such as *E. coli* [151,153,154]. In these studies, an elastic network glycan strands and peptide crosslinks expands as material is inserted with some orientation preference. These models capture cracked-cell shapes that result from patches of defects in the network [153]. Jiang and others also put the growth and shape of multiple Gram-negative cells into a common framework [155]. They use a continuum model of the peptoglycan network to show how growth, cell-wall mechanics, and the bacterial cytoskeleton can interact to produce shape. According to that study, a dynamic helical bundle of MreB exerts forces on the cell wall as it is remodeled, keeping it from swelling in response to the turgor pressure. They use the model to explain shape change after the loss of the MreB helix due to drug treatment. A study by Wang and Wingreen [156] argues that the energetics of MreB and FtsZ filaments, along with those of membranes and interactions between filaments and membranes, are sufficient to explain filament orientation in rod-shaped bacteria cells. Because the models of bacterial shape by Huang *et al*. [153], Jiang *et al*. [155], and Wang and Wingreen [156] describe cells that use a different mechanism to maintain shape, the pattern of growth is very different from the model of fission yeast described in this paper. However, the concept of remodeling part of the wall, of breaking down a peptoglycan network and inserting new material as in Huang *et al*. [153] is similar to the assumptions of our model, even if the region that expands is different.

5-5-3. Modular control of fission yeast shape

Shape regulation, as described in the last part of this work (Figure 27), is essentially modular. The separate components—the microtubule system, the Cdc42 signaling, and the landmarks—interact but are described by separate genes and consist of separate proteins. And to some extent they can operate separately: many of the shaping mechanisms are understood because the other modules continue to work if they are disrupted, as in the case of banana-shaped cells where the Cdc42 cap may function normally but the landmarks are misplaced. Our description of the bent cell shaping mechanism differs from the ideas presented in literature that suggest that the banana shape comes from a length scale within a reaction-diffusion equation [32] (note: such a mechanism also does not distinguish between S and banana shapes) or from whole-cell buckling [35]; these contrasting explanations motivate further experimental study of the ban mutants.

The framework described in this work also appears to be consistent with recent observations of spheroplasts, cells that have become round because the wall has been enzymatically digested [114]. Despite their round shape, these cells form a growth zone of the proper size (and of the altered size in cells missing components of the Cdc42 system) at a random location. Because the growth zone size in this case seems to be independent of the physical shape of the cell, this argues that the Cdc42 system has an intrinsic length scale that ultimately sets the diameter of the cell. The fact that tip growth can occur in spheroplasts treated with microtubule inhibitors [114] provides further support for the conclusions of this work. The fact that spheroplasts with microtubules unperturbed by drugs grow a straighter protuberance [114] is also consistent with the picture advanced here. This particular study also implies another aspect of shape regulation, recovery: cells can recover polarized growth from a spherical shape. This indicates that the machinery is robust enough to reestablish polarity even in cases where it is lost completely.

How would more-complex dynamics, such as oscillations or a changing number of growth zones [3] affect this picture? Perhaps not so dramatically. Because the shapes and parameter dependence of the model do not depend strongly whether one or two growth zones is used (Figure 28, Figure 29), maybe the details of partitioning growth on the timescale of minutes are important for the efficient use of resources (which may be concentrated at one tip in small cells that only have enough growth machinery to grow at one tip [3]) but not for overall morphology.

In addition to genetic and pharmacological manipulation, prior studies on fission-yeast shape also included perturbations to the physical environment of the cell. In particular, in two prior studies cells were confined within curved chambers to study the response of the growth machinery [34,43]. One study used curved passages [34], the other used elastic microchambers [43]—but in both cases they found that cells forced to adopt curved morphologies misplaced landmarks due to a change in the organization of the microtubule system. Both of these studies support the framework of fission-yeast shape regulation proposed in this work (Figure 27). Another study also investigated the effect of external electric fields on the direction of growth [157]. The ability of an external electric field to bias growth [157] could be incorporated into our model as a term added to the microtubule-based potential $U(s)$, corresponding to a process where the electric field induces changes in intracellular pH and produces a bias for localization of the glucan synthases Bgs1 and Bgs4 or some protein upstream of them, as suggested [157].

Finally, we have identified three mechanisms that could lead to round cells: (1) Establishment of a very wide Cdc42 region leading to a diameter comparable to cell length; (2) Sensitivity of cell growth signal to cell diameter (case $\beta > 1$); (3) Highly motile Cdc42 patch (the latter leading mostly to bulgy cells). Future studies imaging the distribution and dynamics of Cdc42 and the cytoskeleton in wild type and mutant cells could help distinguish among these possibilities and test the validity of the proposed modular mechanism.

5-6. Appendix: Methods related to model for remodeling under turgor pressure

Evolution of tip shape as function of growth-factor signal $\Lambda(s)$. The differential equations described by Eq. (4) can be rearranged to give a differential equation for v_t (as in [119]):

$$\frac{\partial v_t}{\partial s} - \left(\frac{\kappa_s \cos\phi}{\kappa_\theta \rho}\right) v_t = \left(\xi_s - \frac{\kappa_s}{\kappa_\theta}\xi_\theta\right). \quad (18)$$

The geometric relations $\sin\phi = \rho\kappa_\theta$ (see Fig. 1) and $\kappa_s = \partial\phi/\partial s$ allow this to be simplified:

$$\frac{\partial v_t}{\partial s} - \cot\phi v_t \frac{\partial \phi}{\partial s} = \left(\xi_s - \frac{\kappa_s}{\kappa_\theta}\xi_\theta\right). \quad (19)$$

The left-hand side is $\sin\phi\partial(v_t \csc\phi)/\partial s$, so the expression can be written:

$$\frac{\partial(v_t \csc\phi)}{\partial s} = \csc\phi\left(\xi_s - \frac{\kappa_s}{\kappa_\theta}\xi_\theta\right). \quad (20)$$

Adding the boundary condition $v_t(0)=0$, which is imposed by axisymmetry, the system admits the following solution:

$$\begin{aligned} v_t(s) &= \sin\phi \int_o^s \csc\phi \left(\xi_s - \frac{\kappa_s}{\kappa_\theta}\xi_\theta \right) ds' \\ v_n(s) &= \frac{\xi_\theta}{\kappa_\theta} - \cos\phi \int_o^s \csc\phi \left(\xi_s - \frac{\kappa_s}{\kappa_\theta}\xi_\theta \right) ds' \end{aligned} \qquad (21)$$

The axisymmetric nature of the model allows the cell surface to be represented by a tip-to-tip contour. For calculation purposes, we discretized the contour to a series of points, with *s* being the sum of segment lengths from tip to point. Derivatives and curvatures were calculated using the five-point stencil. For a given cell shape and $\Lambda(s)$, numerical integration of Eq. (17) gives the normal and tangential velocities. Every point on the contour was moved by $\vec{v} \cdot dt$ (where $\vec{V}$ is the total velocity vector). After this step, new point positions along the segmented contour were calculated to maintain equal separation between the points, with additional points added as the contour becomes longer to maintain approximately the initial spacing. We checked that *dt* and the spacing between points along *s* were sufficiently small for numerical integration. To calculate whole-cell shapes in Figure 24 A, steady-state tip shapes were joined to a cylindrical middle section and the length of that section was chosen to give constant volume.

5-7. Appendix: Methods related to model for shape maintenance by growth zones, landmarks, and microtubules

Cell boundary. The outline of the cell border is modeled as a series of discrete points (see Figure 25 E) as described in Materials and Methods section 1 for the axisymmetric growth model. Here Catmull–Romm splines were used for the interpolation during contour resegmentation. This alleviates an effect where repeated linear resegmentation erodes the contour, especially as dt becomes small.

Choice of number of beads. For the simulation to accurately represent the continuum model, the number of beads should be chosen so that the distance between beads is much smaller than the inverse of any curvature along the contour representing the cell outline. Therefore the initial number of beads n is chosen by:

$$n = 100 \cdot P_{init} / \min(\kappa_{\mathrm{stencil}}, \kappa_{\mathrm{init}}) \, , \qquad (22)$$

where P_{init} is the length of the perimeter at initialization, $\kappa_{\mathrm{stencil}}$ is the curvature at the tip of the stencil, and κ_{init} is the curvature at the tip at initialization.

Growth stencil (Figure 27 E). For the model of Figure 27, we import a tip outline from the three-dimensional model. This is defined as the intersection of the three-dimensional outline with any plane that includes the axis of symmetry of the three-dimensional outline, trimmed back at the section of the outline where the cell becomes cylindrical. A Gaussian growth-factor profile was used to generate this outline, which can then be scaled to match the width parameter of a growth zone. The axis of symmetry of this stencil is then aligned to the normal vector at its position on the contour representing the cell outline. For growth, the tip is moved along this normal vector by $v\,dt$, where v is the magnitude of the growth velocity vector, and points along the contour representing the cell outline are moved towards points that are the same distance along the stencil. Points on the contour representing the cell outline do not move if that movement would be inward (if the inner product of the normal vector with the direction to the corresponding point on the stencil is negative), and only move a maximum distance of $2\,v\,dt\,(1 - s/S)$ where s is the distance from the growth zone and S is the maximum distance along the growth stencil. This prevents discontinuities in the contour representing the cell outline.

Diffusing growth zone (Fig. 6B). While the cells expands, the center of the growth signal zone diffuses in a one-dimensional potential, $U(s)$, or equivalently $U^*(s) \equiv U(s)/\zeta$, where ζ is the drag coefficient. Potential wells surround the tips of the microtubule, and they have the form of a Gaussian with standard deviation σ_{MT} and depth U_0. The movement of the growth zone is simulated according to Brownian dynamics:

$$\frac{\Delta s_{gz}}{\Delta t} = \partial_s U^*(s) + \sqrt{\frac{2D_{gz}}{\Delta t}} \cdot R \quad , \tag{23}$$

where s_{gz} is the growth-zone position, D_{gz} is the growth-zone diffusion coefficient, R is a random number picked from a Gaussian probability density function with standard deviation one and mean zero, and Δt is the integration time step.

Choice of integration time step Δt*.* Because, for each time step, only the local gradient of the potential, $\partial_s U^*(s)$, is used to describe the interaction of the growth zone with the potential, the distance that the growth zone travels during one time step due to both that interaction and diffusion should be small compared to the scale of the features of that potential. After excluding numerical prefactors of order unity, this leads to the conditions:

$$\frac{U_0^*}{\sigma_{MT}} \Delta t << \sigma_{MT}, \qquad \sqrt{D_{gz} \cdot \Delta t} << \sigma_{MT} . \tag{24}$$

Changes to the contour representing the cell outline should also be small compared to the features of that outline during any single time step. An appropriate scale for the features of the outline is the inverse of the stencil-tip curvature, $1/\kappa_{\text{stencil}}$, and changes to the outline go as $v_{\text{growth}}\,\Delta t$. This gives the additional condition:

$$\Delta t << 1/\left(\kappa_{\text{stencil}} v_{\text{growth}}\right) \tag{25}$$

To meet the above criteria we chose the time step to be:

$$\Delta t = .03 \cdot \min\left(\sigma_{MT}{}^{2}/D_{gz}, \sigma_{MT}{}^{2}/U_{0}{}^{*}, \left(\kappa_{\text{stencil}} v_{\text{growth}}\right)^{-1}\right) \tag{26}$$

Measuring bend and width from cell outlines. Because the cell shapes tend to be mostly tubular (visual observation) the degree of bend is approximated by the angle between the line representing the microtubules, which has two ends that move in short steps when it will increase length (described above in ‘Model for Shape Maintenance by Growth Zones, Microtubules, and Landmarks’), and the initial cell axis (*i.e.*, the angle between the purple line and the horizontal in Figure 25 D). We used the squared sine of this angle as a metric (the square of the sine has non-zero average). This measure has some limitations; for instance, a simulated cell growing at both tips that develops a c-shape will appear to have no bend. However, conditions leading to c-shapes also lead to other bent shapes cells and the squared sine is a representative measure. Measuring width also relies on the line simulating microtubules for detecting the endpoints. Moving away from each tip, the distances between pairs of points are compared out to half the cell length away from the tip and the maximal distance is considered to be the width. To divide cells into the three categories of straight cells, bent cells, and bulged cells (Figure 28, Figure 29), we chose thresholds for the degree of bend (squared sine of 0.0015) and measured width (3.45 µm). Category I, straight cells, included only regions of parameter space where both the degree of bend and the measured width were below the threshold. Category II, bent cells, included only regions where the degree of bend was above the threshold and the measured width was below the threshold. Category III included everything else. These thresholds were set by trial and error to match what by inspection appeared to be the three categories.

6. Conclusion

The purpose of this research has been to further the understanding of the physical control of cell growth. To achieve this end, I have focused on fission yeast and developed models for how signaling proteins, the cytoskeleton, and the components of the wall come together to produce a simple, robust growth pattern for this organism. Specific models described the partitioning of signaling protein Cdc42 between the two cell tips [3], how the cell wall expands due to signal-dependent remodeling under turgor pressure, and how interacting modules (growth zones, microtubules, and landmarks) could work together to regulate shape.

Future modeling efforts on this topic should be informed by experiments that will fill in details, such as of delivery rates and reaction coefficients, about these growth processes that are at present missing. Using CRIB-GFP and other markers for Cdc42 and related proteins, in conjunction with markers for the cytoskeleton, exocytosis, and wall remodeling, to study how these modules relate in wild-type and growth-aberrant cells will provide many tests of the models described in this thesis and challenges for future models. Studying how the cell wall is remodeled at a molecular level, through biochemistry and possibly super-resolution microscopy, will inform coarse-grained models of how its shape changes, and study of the Cdc42 pathway and associated pathways will clarify the picture of how physical growth events are linked to signaling and shape detection. By starting from a similar quantitative framework to the work presented here in Section 5-4, but elaborating on and expanding it with details from molecular biology experiments, researchers could develop a rich test environment for uncovering more details about the processes and mechanisms responsible for the establishment and maintenance of shape.

To apply these models to more complex organisms, they will almost certainly require modifications. But the need for modifications will inform us. Cytoskeletal elements and regulators are often strongly conserved. In some cases, asking why the models must be adjusted despite this may lead to insight about the organism—may reveal why the organism required the adjusted mechanism. To confidently address these complex questions, we must first demonstrate the accuracy and predictive power of modeling simpler biological systems. The studies described in the review provide first steps towards this demonstration. Fission yeast provides, at least, a testing ground for modeling methods—a foundation for modeling more complex organisms.

	n	New end/Old end average intensity ratio[†]	Relative intensity fluctuations, new end*	Relative intensity fluctuations, old end*	Fraction with at least one tip exhibiting oscillations, lower bound	Period (min)[†]
WT, Asymmetric	6	0.21 ± 0.11	0.71 ± 0.18	0.30 ± 0.07	50%	4.5 ± 1.8
WT, Symmetric	16	0.84 ± 0.3	0.46 ± 0.04	0.39 ± 0.03	45%	5.1 ± 2.1
gef1Δ, Asymmetric	10	0.13 ± 0.06	0.88 ± 0.06	0.30 ± 0.03	50%	4.1 ± 1.2
*gef1*Δ, Symmetric	7	0.96 ± 0.13	0.52 ± 0.08	0.55 ± 0.07	72%	4.1 ± 0.7
*cdc25-22, S*ymmetric (16+)	7	0.95 ± 0.15	0.45 ± 0.07	0.38 ± 0.03	14%	
*cdc25-22, S*ymmetric (13-16)	9	1.04 ± 0.27	0.39 ± 0.01	0.38 ± 0.02	33%	6.6 ± 2.8
*rga4*Δ, Asymmetric	5	0.23 ± 0.09	0.57 ± 0.07	0.30 ± 0.03	60 %	4.0 ± 1.7
*rga4*Δ, Symmetric	11	0.79 ± 0.21	0.47 ± 0.04	0.55 ± 0.05	64%	4.5 ± 0.7
pJK 148 nmt1-gef1 Symmetric	16	1.07 ± 0.35	0.21 ± 0.02	0.22 ± 0.01	31 %	3.3 ± 0.6
pJK 148 control, Symmetric	15	1.01 ± 0.33	0.43 ± 0.03	0.41 ± 0.02	87%	4.1 ± 0.95
Scd2-GFP, Symmetric	14	0.99 ± 0.4	0.50 ± 0.04	0.46 ± 0.04	27 %	4.7 ± 1.5
Scd2-GFP, Asymmetric	8	0.28 ± 0.05	0.50 ± 0.06	0.43 ± 0.04	50 %	5.1 ±1.5

	n	Non-growing/ growing end average intensity ratio[†]	Relative intensity fluctuations, non-growing end*	Relative intensity fluctuations, growing end*	Fraction with at least one tip exhibiting oscillations, lower bound	Period (min)
orb2-34, Asymmetric	10	0.05 ± 0.06	1.6 ± 0.5	0.21 ± 0.02	70%	6.3 ± 1.1
Tea1□, Asymmetric	10	0.03 ± 0.07	2.0 ± 0.4	0.45 ± 0.05	1/10 cell marginally oscillates with period 3 min	

[†] Error bars represent one standard deviation among different time courses

* Error bars represent standard deviation of mean among different time courses

Two boxes are unfilled because of insufficient data to calculate a reliable average

Table 1. CRIB-GFP and Scd2-GFP tip intensities and fluctuations. Over a given time course, the tip CRIB-GFP intensities exhibit a complex pattern (see Fig. 1E). The parameters in the table were derived under the assumption that the signal consists of a rapidly fluctuating pattern superimposed over a slowly changing average. The average value may change suddenly due to switching of steady states (e.g. symmetric to asymmetric as in Fig. 1E) or slowly over tens of minutes due to changes in the cell conditions, e.g. expression levels. We measured many cells and separated the signal from each cell into 10-100 min intervals. During such intervals, the behavior at each tip could be attributed to fluctuations around a stationary average. Thus we excluded those parts of the signal that could be attributed to cells in the process of switching states or those parts that included a slow drift of the average value. The value of *n* is the number of such intervals. We separated the resulting time courses into “symmetric” and “asymmetric”, depending on whether fraction of CRIB-GFP signal at the tip with the lower intensity was larger or smaller than 25% (an empirical value that helped classify the cells into two groups). The first three columns show the values of the ratio of average intensity between tips and corresponding relative fluctuations (defined as the ratio of standard deviation within an individual time course over average intensity). To distinguish between parts that exhibit periodic oscillations versus those that simply fluctuate, we calculated the auto-correlation and cross-correlation functions for each time course as in Supplementary Fig. 3. We then counted the number of cells that exhibited peaks indicative of oscillatory

behavior. The measured value of the fraction of oscillating cells should be considered as a lower bound since factors such as high signal noise and duration of time course can limit our ability to detect the oscillatory component. The period was estimated by measuring the position of the peaks in the auto-correlation function. Cells expressing increased levels of Gef1 (pJK 148 *nmt1-gef1*) were predominantly symmetric, and were compared to symmetric cells in the control. We could not detect statistically significant differences in the period among the different cell types. This was largely due to ~ 1 min measurement error in individual measurements and limited number of oscillating cells for certain cell types. See also legend of Table 2 for a comparison of different cells types.

	n	Cross-correlation	Cross-correlation, standard deviation	Cross-correlation, standard deviation of mean	Cell length ± standard deviation (mm)	Time interval ± standard deviation (min)
WT, Asymmetric	6	-0.43	0.22	0.09	9.5 ± 0.9	13 ± 3
WT, Symmetric	16	-0.42	0.18	0.05	10.1 ± 0.7	26 ± 11
*gef1*Δ, Asymmetric	10	-0.32	0.28	0.08	10.0 ± 0.8	20 ± 14
*gef1*Δ, Symmetric	7	-0.42	0.14	0.05	10.7 ± 1.0	27 ± 16
cdc25-22, Symmetric (16+)	7	0.018	0.19	0.07	17.1 ± 0.8	36 ± 14
cdc25-22, Symmetric (13-16)	9	-0.23	0.28	0.11	14.5 ± 1.0	36 ± 9
*rga4*Δ, Asymmetric	6	-0.32	0.31	0.14	9.5 ± 0.6	20 ± 8
*rga4*Δ, Symmetric	11	-0.56	0.22	0.07	10.0 ± 0.5	26 ± 9
pJK148 *nmt1-Gef1* Symmetric	16	-0.014	0.26	0.07	9.0 ± 0.7	28 ± 10
pJK148 control, Symmetric	15	-0.47	0.19	0.05	10.5 ± 0.7	25 ± 7
Scd2-GFP, Symmetric	14	-0.2	0.33	0.09	ND	22 ± 5
Scd2-GFP, Asymmetric	8	-0.25	0.26	0.10	ND	18 ± 7

Table 2. Cross-correlations of CRIB-GFP and Scd2-GFP tip intensities. Value of instantaneous cross-correlation between tip intensities for the same cells as in Supplementary Table 2. Cell length (time interval) indicates the average length (time interval) of the cells used to calculate the values of Table S2 and S3. Negative values of the cross-correlation coefficient indicate anti-correlated behavior (as opposed to positive values that indicate positive correlations).

Comparison of Symmetric Cells in Table 1 and Table 2.
(a) *gef1*Δ Symmetric cells had similar values for the relative intensity fluctuations and cross-correlation coefficients with WT Symmetric cells, within one or two standard deviation of the mean of one another.
(b) *cdc25-22* Symmetric cells had similar relative intensity fluctuations compared to WT cells (within one standard deviation of the mean) but significantly smaller cross-correlation coefficients than WT cells (several standard deviations of the mean, p = 0.00019).
(c) *rga*4Δ Symmetric cells had similar values for the relative intensity fluctuations and cross-correlation coefficients with WT Symmetric cells, within one or two standard deviation of the mean of one another.
(d) Control pJK 148 Symmetric Cells had similar values for the relative intensity fluctuations and cross-correlation coefficients with WT Symmetric cells, within one standard deviation of the mean of one another.
(e) pJK148 *nmt1-Gef1* Symmetric cells (that over-express Gef1) had characteristically smaller relative intensity fluctuations and cross-correlation coefficients than control pJK 148 Symmetric Cells and WT Symmetric cells, by several standard deviations of the mean: p = 0.0000088 for NE relative fluctuations between Gef1 over-expression and control pJK148 cells, p = 0.000042 for OE relative fluctuations between Gef1 over-expression and control pJK148 cells, and p = 0.000022 for cross-correlation coefficients between Gef1 over-expression and control pJK148 cells. The fraction of oscillating

pJK148 *nmt1-Gef1*
Symmetric cells also appears smaller then the Control pJK 148 Symmetric Cells and WT Symmetric cells.

Parameter	Description	Value	Reason
$\alpha_A \equiv \frac{\lambda_0^+}{k^- C_{\text{sat}}}$	Magnitude of regular association compared to dissociation rate constant.	2.25	Four conditions determine these parameter choices. (1) The upper and lower bounds of the coexistence region should match the results in Figure 11 C as $\bar{C}_{\text{tot}}$ increases. (2) The value of *n* must be high enough such that the lagging tip accumulates enough Cdc42 in asymmetric states, see NE/OE ratio in Table S4. (3) The model requires a significant fraction of available Cdc42 at the tips, so we impose that 70% of available Cdc42 is tip-bound for the shortest cells. (4) Constant total active-Cdc42 density requires that this occurs over an interval where $\bar{C}_{\text{tot}}$ doubles.
$\alpha_B \equiv \frac{\lambda_n^+ C_{sat}^{n-1}}{k^-}$	Magnitude of autocatalytic association rate constant compared to dissociation rate constant.	6.467	
$\bar{C}_{\text{tot}} \equiv \frac{C_{\text{tot}}}{C_{\text{sat}}}$	Initial (final) ratio of total active-Cdc42 amount to saturation amount. Doubles during the life of the cell.	6.5 (13)	
n	Non-linearity of autocatalytic term	4	

Additional Parameters for Oscillations, Increasing Cell Length

Parameter	Description	Value	Reason
$d\bar{C}_{\text{tot}} / dt$	Rate of change of $\bar{C}_{\text{tot}}$	.0271 min^{-1}	Cells double in approximately four hours.
τ	Delay constant for dissociation amplification	2 min	Affects oscillation frequency, tuned so that oscillations match observed period.
ε	Relative strength of delayed dissociation	.5375	Set to match the observed oscillation size.
h	Non-linearity of dissociation	40	Set to be sufficiently non-linear to see significant oscillations.
k^-	Dissociation rate	4 min^{-1}	Affects oscillation shape and degree of anti-correlation between tips. Set to match observed oscillatory behavior.

Table 3. Polarity-Model Parameters.

Table 4. Parameters for the two-dimensional model of Foethke *et al.* (see Figure 26). For the units, distances are given in µm, forces are given in pN, and times are expressed in seconds. Bolded values are changed for some simulations as described in the text. These values are used in a configuration file for the Cytosim program found at http://www.cytosim.org/cytosim/index.html. We used the compiled version 3.0 beta found on that site, which comes with a set of configuration files. The default values for the microtubule simulation can be found in the pombe.cym file.

Container	Parameter	Description	Value
simul	time_step	time step for integration	0.01
simul	kT	temperature in energy units	0.0042
simul	viscosity	viscosity of cytoplasm partially determines mobility of nucleus	0.9
simul	precondition		0
simul	binary_output		0
space pombe	geometry	shape of the cell boundary; 'capsule' indicates spherocylinder; 2.4 is half the cylinder height; 1.6 is the radius of the hemispheres	**(capsule 2.4 1.6) adjusted to change dimensions of cell, see Figure 26**
fiber microtubule	rigidity	modulus for bending elasticity	**30 (up to 300)**
fiber microtubule	confine	sets forces between fiber and confining space	inside, 200
fiber microtubule	activity		dynamic
fiber microtubule	unit_length	length of discrete units of assembly/disassembly	0.008
fiber microtubule	growing_speed	speed of assembly	0.06
fiber microtubule	shrinking_speed	speed of disassembly	-0.15
fiber microtubule	hydrolysis_rate	hydrolysis rate of g-units, from which the catastrophe rate is calculated	**0.058 (up to 0.29)**
fiber microtubule	growing_force	characteristic force of polymer assembly, used for force-dependent catastrophes	**1.7 (down to 0.17)**
fiber microtubule	shrinking_fate	what happens when a microtubule reaches the minimum authorized length	rescue

fiber microtubule	min_length	minimum authorized length	0.5
sphere envelope	point_mobility	mobility of points on the surface	0.05
sphere envelope	radius	the radius of the sphere	1.3
sphere envelope	confine	flag to confine this object	inside, 200
sphere envelope	piston_effect	if true, use special formula to calculate mobility (presumably as in Foethke, et al.)	1
bundle microtubule_bundle	fibers	the name of the fiber in the bundle	microtubule
bundle microtubule_bundle	nb_fibers	the number of fibers in the bundle	4
bundle microtubule_bundle	overlap	the length of the zone where the fibers in the bundle overlap	0.5
bundle microtubule_bundle	stiffness	stiffness of the links that connect overlapping fibers	1000
nucleus nucleus	sphere	name of the sphere	envelope
nucleus nucleus	nb_bundles	number of MTOCs	4
nucleus nucleus	bundles	the bundles at the MTOCs	microtubule_bundle
nucleus nucleus	stiffness	stiffness of assembly links	200

Works Cited

1. Drake T, Vavylonis D (2013) Model of Fission Yeast Cell Shape Driven by Membrane-Bound Growth Factors and the Cytoskeleton. PLoS Comput Biol 9: e1003287.
2. Drake T, Yusuf E, Vavylonis D (2012) A Systems-Biology Approach to Yeast Actin Cables. Advances in Systems Biology 736: 325-335.
3. Das M, Drake T, Wiley DJ, Buchwald P, Vavylonis D, et al. (2012) Oscillatory Dynamics of Cdc42 GTPase in the Control of Polarized Growth. Science 337: 239-243.
4. Drake T, Vavylonis D (2010) Cytoskeletal dynamics in fission yeast: a review of models for polarization and division. Hfsp Journal 4: 122-130.
5. Das M, Wiley DJ, Medina S, Vincent HA, Larrea M, et al. (2007) Regulation of cell diameter, For3p localization, and cell symmetry by fission yeast Rho-GAP Rga4p. Molecular Biology of the Cell 18: 2090-2101.
6. Kelly FD, Nurse P (2011) Spatial control of Cdc42 activation determines cell width in fission yeast. Molecular Biology of the Cell 22: 3801-3811.
7. Groves JT, Kuriyan J (2010) Molecular mechanisms in signal transduction at the membrane. Nature Structural & Molecular Biology 17: 659-665.
8. Pollard TD, Earnshaw WC, Lippincott-Schwartz J (2008) Cell biology. Philadelphia: Saunders/Elsevier. xix, 905 p. p.
9. Svitkina TM, Verkhovsky AB, McQuade KM, Borisy GG (1997) Analysis of the actin-myosin II system in fish epidermal keratocytes: Mechanism of cell body translocation. Journal of Cell Biology 139: 397-415.
10. Lewin B (2007) Cells. Sudbury, Mass.: Jones and Bartlett Publishers. xix, 863 p. p.
11. Tsien RY (1998) The green fluorescent protein. Annual Review of Biochemistry 67: 509-544.
12. Wu JQ, Pollard TD (2005) Counting cytokinesis proteins globally and locally in fission yeast. Science 310: 310-314.
13. Feierbach B, Chang F (2001) Roles of the fission yeast formin for3p in cell polarity, actin cable formation and symmetric cell division. Current Biology 11: 1656-1665.
14. Hayles J, Nurse P (2001) A journey into space. Nature Reviews Molecular Cell Biology 2: 647-656.
15. La Carbona S, Le Goff C, Le Goff X (2006) Fission yeast cytoskeletons and cell polarity factors: connecting at the cortex. Biology of the Cell 98: 619-631.
16. Mogilner A, Wollman R, Marshall WF (2006) Quantitative modeling in cell biology: What is it good for? Developmental Cell 11: 279-287.
17. Pollard TD, Wu JQ (2010) Understanding cytokinesis: lessons from fission yeast. Nature Reviews Molecular Cell Biology 11: 149-155.
18. Mitchison JM, Nurse P (1985) Growth in Cell Length in the Fission Yeast Schizosaccharomyces-Pombe. Journal of Cell Science 75: 357-376.
19. Martin SG (2009) Microtubule-dependent cell morphogenesis in the fission yeast. Trends in Cell Biology 19: 447-454.

20. Piel M, Tran PT (2009) Cell Shape and Cell Division in Fission Yeast. Current Biology 19: R823-R827.
21. Tolic-Norrelykke IM (2010) Force and length regulation in the microtubule cytoskeleton: lessons from fission yeast. Current Opinion in Cell Biology 22: 21-28.
22. Chang F, Martin SG (2009) Shaping fission yeast with microtubules. Cold Spring Harb Perspect Biol 1: a001347.
23. Sawin KE, Tran PT (2006) Cytoplasmic microtubule organization in fission yeast. Yeast 23: 1001-1014.
24. Mata J, Nurse P (1997) tea1 and the microtubular cytoskeleton are important for generating global spatial order within the fission yeast cell. Cell 89: 939-949.
25. Moseley JB, Goode BL (2006) The yeast actin cytoskeleton: From cellular function to biochemical mechanism. Microbiology and Molecular Biology Reviews 70: 605-+.
26. Pollard TD, Cooper JA (2009) Actin, a Central Player in Cell Shape and Movement. Science 326: 1208-1212.
27. Martin SG, Chang F (2006) Dynamics of the formin For3p in actin cable assembly. Current Biology 16: 1161-1170.
28. Sirotkin V, Beltzner CC, Marchand JB, Pollard TD (2005) Interactions of WASp, myosin-I, and verprolin with Arp2/3 complex during actin patch assembly in fission yeast. Journal of Cell Biology 170: 637-648.
29. Marks J, Hagan IM, Hyams JS (1986) Growth Polarity and Cytokinesis in Fission Yeast - the Role of the Cytoskeleton. Journal of Cell Science: 229-241.
30. Martin SG, Chang F (2005) New end take off - Regulating cell polarity during the fission yeast cell cycle. Cell Cycle 4: 1046-1049.
31. Rupes I, Jia ZP, Young PG (1999) Ssp1 promotes actin depolymerization and is involved in stress response and new end take-off control in fission yeast. Molecular Biology of the Cell 10: 1495-1510.
32. Csikasz-Nagy A, Gyorffy B, Alt WG, Tyson JJ, Novak B (2008) Spatial controls for growth zone formation during the fission yeast cell cycle. Yeast 25: 59-69.
33. Meinhardt H, Gierer A (2000) Pattern formation by local self-activation and lateral inhibition. Bioessays 22: 753-760.
34. Terenna CR, Makushok T, Velve-Casquillas G, Baigl D, Chen Y, et al. (2008) Physical Mechanisms Redirecting Cell Polarity and Cell Shape in Fission Yeast. Current Biology 18: 1748-1753.
35. Riveline D (2009) Explaining Lengths and Shapes of Yeast by Scaling Arguments. Plos One 4.
36. Baumgartner S, Tolic-Norrelykke IM (2009) Growth Pattern of Single Fission Yeast Cells Is Bilinear and Depends on Temperature and DNA Synthesis. Biophysical Journal 96: 4336-4347.
37. Wang H, Vavylonis D (2008) Model of For3p-Mediated Actin Cable Assembly in Fission Yeast. Plos One 3.
38. Galletta BJ, Chuang DY, Cooper JA (2008) Distinct roles for Arp2/3 regulators in actin assembly and endocytosis. Plos Biology 6: 72-85.
39. Kaksonen M, Toret CP, Drubin DG (2005) A modular design for the clathrin- and actin-mediated endocytosis machinery. Cell 123: 305-320.

40. Berro J, Sirotkin V, Pollard TD (2010) Mathematical Modeling of Endocytic Actin Patch Kinetics in Fission Yeast: Disassembly Requires Release of Actin Filament Fragments. Molecular Biology of the Cell 21: 2905-2915.
41. Liu J, Kaksonen M, Drubin DG, Oster G (2006) Endocytic vesicle scission by lipid phase boundary forces. Proceedings of the National Academy of Sciences of the United States of America 103: 10277-10282.
42. Liu J, Sun YD, Drubin DG, Oster GF (2009) The Mechanochemistry of Endocytosis. Plos Biology 7.
43. Minc N, Bratman SV, Basu R, Chang F (2009) Establishing New Sites of Polarization by Microtubules. Current Biology 19: 83-94.
44. Daga RR, Yonetani A, Chang F (2006) Asymmetric microtubule pushing forces in nuclear centering. Current Biology 16: 1544-1550.
45. Tolic-Norrelykke IM, Sacconi L, Stringari C, Raabe I, Pavone FS (2005) Nuclear and division-plane positioning revealed by optical micromanipulation. Current Biology 15: 1212-1216.
46. Tran PT, Marsh L, Doye V, Inoue S, Chang F (2001) A mechanism for nuclear positioning in fission yeast based on microtubule pushing. Journal of Cell Biology 153: 397-411.
47. Foethke D, Makushok T, Brunner D, Nedelec F (2009) Force- and length-dependent catastrophe activities explain interphase microtubule organization in fission yeast. Mol Syst Biol 5: 241.
48. Janson ME, Loughlin R, Loiodice I, Fu CH, Brunner D, et al. (2007) Crosslinkers and motors organize dynamic microtubules to form stable bipolar arrays in fission yeast. Cell 128: 357-368.
49. Padte NN, Martin SG, Howard M, Chang F (2006) The cell-end factor pom1p inhibits mid1p in specification of the cell division plane in fission yeast. Current Biology 16: 2480-2487.
50. Martin SG, Berthelot-Grosjean M (2009) Polar gradients of the DYRK-family kinase Pom1 couple cell length with the cell cycle. Nature 459: 852-U857.
51. Moseley JB, Mayeux A, Paoletti A, Nurse P (2009) A spatial gradient coordinates cell size and mitotic entry in fission yeast. Nature 459: 857-U858.
52. Saunders TE, Pan KZ, Angel A, Guan YH, Shah JV, et al. (2012) Noise Reduction in the Intracellular Pom1p Gradient by a Dynamic Clustering Mechanism. Developmental Cell 22: 558-572.
53. Coffman VC, Nile AH, Lee IJ, Liu HY, Wu JQ (2009) Roles of Formin Nodes and Myosin Motor Activity in Mid1p-dependent Contractile-Ring Assembly during Fission Yeast Cytokinesis. Molecular Biology of the Cell 20: 5195-5210.
54. Vavylonis D, Wu JQ, Hao S, O'Shaughnessy B, Pollard TD (2008) Assembly mechanism of the contractile ring for cytokinesis by fission yeast. Science 319: 97-100.
55. Hachet O, Simanis V (2008) Mid1p/anillin and the septation initiation network orchestrate contractile ring assembly for cytokinesis. Genes & Development 22: 3205-3216.
56. Ojkic N, Vavylonis D (2010) Kinetics of Myosin Node Aggregation into a Contractile Ring. Physical Review Letters 105.

57. Ojkic N, Wu JQ, Vavylonis D (2011) Model of myosin node aggregation into a contractile ring: the effect of local alignment. Journal of Physics-Condensed Matter 23.
58. Laporte D, Ojkic N, Vavylonis D, Wu JQ (2011) The condensation of actomyosin network into a contractile ring depends on actin cross-linkers alpha actinin and fimbrin during fission yeast cytokinesis. Molecular Biology of the Cell 22.
59. Carlsson AE (2006) Contractile stress generation by actomyosin gels. Physical Review E 74.
60. Kruse K, Julicher F (2003) Self-organization and mechanical properties of active filament bundles. Physical Review E 67.
61. Larripa K, Mogilner A (2006) Transport of a 1D viscoelastic actin-myosin strip of gel as a model of a crawling cell. Physica a-Statistical Mechanics and Its Applications 372: 113-123.
62. Liverpool TB, Marchetti MC (2006) Rheology of active filament solutions. Physical Review Letters 97.
63. Zumdieck A, Kruse K, Bringmann H, Hyman AA, Julicher F (2007) Stress Generation and Filament Turnover during Actin Ring Constriction. Plos One 2.
64. Proctor SA, Minc N, Boudaoud A, Chang F (2012) Contributions of Turgor Pressure, the Contractile Ring, and Septum Assembly to Forces in Cytokinesis in Fission Yeast. Current Biology 22: 1601-1608.
65. Mishra M, Huang YY, Srivastava P, Srinivasan R, Sevugan M, et al. (2012) Cylindrical cellular geometry ensures fidelity of division site placement in fission yeast. Journal of Cell Science 125: 3850-3857.
66. Fu CH, Ward JJ, Loiodice I, Velve-Casquillas G, Nedelec FJ, et al. (2009) Phospho-Regulated Interaction between Kinesin-6 Klp9p and Microtubule Bundler Ase1p Promotes Spindle Elongation. Developmental Cell 17: 257-267.
67. Mogilner A, Wollman R, Civelekoglu-Scholey G, Scholey J (2006) Modeling mitosis. Trends in Cell Biology 16: 88-96.
68. Sprague BL, Pearson CG, Maddox PS, Bloom KS, Salmon ED, et al. (2003) Mechanisms of microtubule-based kinetochore positioning in the yeast metaphase spindle. Biophysical Journal 84: 3529-3546.
69. Pearson CG, Yeh E, Gardner M, Odde D, Salmon ED, et al. (2004) Stable kinetochore-microtubule attachment constrains centromere positioning in metaphase. Current Biology 14: 1962-1967.
70. Gardner MK, Pearson CG, Sprague BL, Zarzar TR, Bloom K, et al. (2005) Tension-dependent regulation of microtubule dynamics at kinetochores can explain metaphase congression in yeast. Molecular Biology of the Cell 16: 3764-3775.
71. Gardner MK, Bouck DC, Paliulis LV, Meehl JB, O'Toole ET, et al. (2008) Chromosome Congression by Kinesin-5 Motor-Mediated Disassembly of Longer Kinetochore Microtubules. Cell 135: 894-906.
72. Dorn JF, Jaqaman K, Rines DR, Jelson GS, Sorger PK, et al. (2005) Yeast kinetochore microtubule dynamics analyzed by high-resolution three-dimensional microscopy. Biophysical Journal 89: 2835-2854.
73. Tolic-Norrelykke IM (2008) Push-me-pull-you: how microtubules organize the cell interior. European Biophysics Journal with Biophysics Letters 37: 1271-1278.

74. Vogel SK, Pavin N, Maghelli N, Julicher F, Tolic-Norrelykke IM (2009) Self-Organization of Dynein Motors Generates Meiotic Nuclear Oscillations. Plos Biology 7: 918-928.
75. Heasman SJ, Ridley AJ (2008) Mammalian Rho GTPases: new insights into their functions from in vivo studies. Nat Rev Mol Cell Biol 9: 690-701.
76. Cowan CR, Hyman AA (2007) Acto-myosin reorganization and PAR polarity in C. elegans. Development (Cambridge, England) 134: 1035-1043.
77. Perez P, Rincon SA (2010) Rho GTPases: regulation of cell polarity and growth in yeasts. Biochem J 426: 243-253.
78. Slaughter BD, Smith SE, Li R (2009) Symmetry breaking in the life cycle of the budding yeast. Cold Spring Harbor perspectives in biology 1: a003384.
79. Irazoqui JE, Gladfelter AS, Lew DJ (2003) Scaffold-mediated symmetry breaking by Cdc42p. Nature cell biology 5: 1062-1070.
80. Kozubowski L, Saito K, Johnson JM, Howell AS, Zyla TR, et al. (2008) Symmetry-breaking polarization driven by a Cdc42p GEF-PAK complex. Current biology : CB 18: 1719-1726.
81. Wedlich-Soldner R, Wai SC, Schmidt T, Li R (2004) Robust cell polarity is a dynamic state established by coupling transport and GTPase signaling. The Journal of cell biology 166: 889-900.
82. Slaughter BD, Das A, Schwartz JW, Rubinstein B, Li R (2009) Dual modes of cdc42 recycling fine-tune polarized morphogenesis. Developmental cell 17: 823-835.
83. Tatebe H, Nakano K, Maximo R, Shiozaki K (2008) Pom1 DYRK regulates localization of the Rga4 GAP to ensure bipolar activation of Cdc42 in fission yeast. Current Biology 18: 322-330.
84. Endo M, Shirouzu M, Yokoyama S (2003) The Cdc42 binding and scaffolding activities of the fission yeast adaptor protein Scd2. Journal of Biological Chemistry 278: 843-852.
85. Wheatley E, Rittinger K (2005) Interactions between Cdc42 and the scaffold protein Scd2: requirement of SH3 domains for GTPase binding. Biochemical Journal 388: 177-184.
86. Goryachev AB, Pokhilko AV (2008) Dynamics of Cdc42 network embodies a Turing-type mechanism of yeast cell polarity. Febs Letters 582: 1437-1443.
87. Marco E, Wedlich-Soldner R, Li R, Altschuler SJ, Wu LF (2007) Endocytosis optimizes the dynamic localization of membrane proteins that regulate cortical polarity. Cell 129: 411-422.
88. Novak B, Tyson JJ (2008) Design principles of biochemical oscillators. Nature Reviews Molecular Cell Biology 9: 981-991.
89. Ozbudak EM, Becskei A, van Oudenaarden A (2005) A system of counteracting feedback loops regulates Cdc42p activity during spontaneous cell polarization. Developmental Cell 9: 565-571.
90. Meinhardt H, de Boer PAJ (2001) Pattern formation in Escherichia coli: A model for the pole-to-pole oscillations of Min proteins and the localization of the division site. Proceedings of the National Academy of Sciences of the United States of America 98: 14202-14207.

91. Coll PM, Trillo Y, Ametzazurra A, Perez P (2003) Gef1p, a new guanine nucleotide exchange factor for Cdc42p, regulates polarity in Schizosaccharomyces pombe. Molecular Biology of the Cell 14: 313-323.
92. Martin SG, Rincon SA, Basu R, Perez P, Chang F (2007) Regulation of the formin for3p by cdc42p and bud6p. Molecular Biology of the Cell 18: 4155-4167.
93. Chang E, Bartholomeusz G, Pimental R, Chen J, Lai H, et al. (1999) Direct binding and in vivo regulation of the fission yeast p21-activated kinase Shk1 by the SH3 domain protein Scd2. Molecular and Cellular Biology 19: 8066-8074.
94. Chang EC, Barr M, Wang Y, Jung V, Xu HP, et al. (1994) Cooperative Interaction of S-Pombe Proteins Required for Mating and Morphogenesis. Cell 79: 131-141.
95. Howell AS, Jin M, Wu CF, Zyla TR, Elston TC, et al. (2012) Negative Feedback Enhances Robustness in the Yeast Polarity Establishment Circuit. Cell 149: 322-333.
96. Verde F, Wiley DJ, Nurse P (1998) Fission yeast orb6, a ser/thr protein kinase related to mammalian rho kinase and myotonic dystrophy kinase, is required for maintenance of cell polarity and coordinates cell morphogenesis with the cell cycle. Proceedings of the National Academy of Sciences of the United States of America 95: 7526-7531.
97. Marcus S, Polverino A, Chang E, Robbins D, Cobb MH, et al. (1995) Shk1, a Homolog of the Saccharomyces-Cerevisiae Ste20 and Mammalian P65(Pak) Protein-Kinases, Is a Component of a Ras/Cdc42 Signaling Module in the Fission Yeast Schizosaccharomyces-Pombe. Proceedings of the National Academy of Sciences of the United States of America 92: 6180-6184.
98. Ottilie S, Miller PJ, Johnson DI, Creasy CL, Sells MA, et al. (1995) Fission Yeast Pak1(+) Encodes a Protein-Kinase That Interacts with Cdc42p and Is Involved in the Control of Cell Polarity and Mating. Embo Journal 14: 5908-5919.
99. Gulli MP, Jaquenoud M, Shimada Y, Niederhauser G, Wiget P, et al. (2000) Phosphorylation of the Cdc42 exchange factor Cdc24 by the PAK-like kinase Cla4 may regulate polarized growth in yeast. Molecular Cell 6: 1155-1167.
100. Karsenti E (2008) Self-organization in cell biology: a brief history. Nature Reviews Molecular Cell Biology 9: 255-262.
101. Howell AS, Savage NS, Johnson SA, Bose I, Wagner AW, et al. (2009) Singularity in polarization: rewiring yeast cells to make two buds. Cell 139: 731-743.
102. Cerone L, Novak B, Neufeld Z (2012) Mathematical Model for Growth Regulation of Fission Yeast Schizosaccharomyces pombe. Plos One 7.
103. Fischer R, Zekert N, Takeshita N (2008) Polarized growth in fungi--interplay between the cytoskeleton, positional markers and membrane domains. Molecular Microbiology 68: 813-826.
104. Geitmann A, Ortega JKE (2009) Mechanics and modeling of plant cell growth. Trends in Plant Science 14: 467-478.
105. Brown PJ, Kysela DT, Brun YV (2011) Polarity and the diversity of growth mechanisms in bacteria. Semin Cell Dev Biol 22: 790-798.
106. Huisman SM, Brunner D (2011) Cell polarity in fission yeast: a matter of confining, positioning, and switching growth zones. Semin Cell Dev Biol 22: 799-805.
107. Hachet O, Bendezu FO, Martin SG (2012) Fission yeast: in shape to divide. Curr Opin Cell Biol 24: 858-864.

108. Verde F, Mata J, Nurse P (1995) Fission Yeast-Cell Morphogenesis - Identification of New Genes and Analysis of Their Role during the Cell-Cycle. Journal of Cell Biology 131: 1529-1538.
109. Verde F, Wiley DJ, Nurse P (1998) Fission yeast orb6, a ser/thr protein kinase related to mammalian rho kinase and myotonic dystrophy kinase, is required for maintenance of cell polarity and coordinates cell morphogenesis with the cell cycle. Proc Natl Acad Sci U S A 95: 7526-7531.
110. Villar-Tajadura MA, Coll PM, Madrid M, Cansado J, Santos B, et al. (2008) Rga2 is a Rho2 GAP that regulates morphogenesis and cell integrity in S. pombe. Molecular Microbiology 70: 867-881.
111. Das M, Wiley DJ, Chen X, Shah K, Verde F (2009) The Conserved NDR Kinase Orb6 Controls Polarized Cell Growth by Spatial Regulation of the Small GTPase Cdc42. Current Biology 19: 1314-1319.
112. Cheung AY, Wu HM (2008) Structural and signaling networks for the polar cell growth machinery in pollen tubes. Annu Rev Plant Biol 59: 547-572.
113. La Carbona S, Le Goff C, Le Goff X (2006) Fission yeast cytoskeletons and cell polarity factors: connecting at the cortex. Biol Cell 98: 619-631.
114. Kelly FD, Nurse P (2011) De Novo Growth Zone Formation from Fission Yeast Spheroplasts. PLoS One 6.
115. Bendezu FO, Martin SG (2011) Actin cables and the exocyst form two independent morphogenesis pathways in the fission yeast. Mol Biol Cell 22: 44-53.
116. Cortes JCG, Ishiguro J, Duran A, Ribas JC (2002) Localization of the (1,3)beta-D-glucan synthase catalytic subunit homologue Bgs1p/Cps1p from fission yeast suggests that it is involved in septation, polarized growth, mating, spore wall formation and spore germination. Journal of Cell Science 115: 4081-4096.
117. Cortes JCG, Carnero E, Ishiguro J, Sanchez Y, Duran A, et al. (2005) The novel fission yeast (1,3)beta-D-glucan synthase catalytic subunit Bgs4p is essential during both cytokinesis and polarized growth. Journal of Cell Science 118: 157-174.
118. Minc N, Boudaoud A, Chang F (2009) Mechanical Forces of Fission Yeast Growth. Current Biology 19: 1096-1101.
119. Dumais J, Shaw SL, Steele CR, Long SR, Ray PM (2006) An anisotropic-viscoplastic model of plant cell morphogenesis by tip growth. International Journal of Developmental Biology 50: 209-222.
120. Ugural AC (1999) Stresses in plates and shells. Boston: WCB/McGraw Hill. xx, 502 p. p.
121. Osumi M, Sato M, Ishijima SA, Konomi M, Takagi T, et al. (1998) Dynamics of cell wall formation in fission yeast, Schizosaccharomyces pombe. Fungal Genetics and Biology 24: 178-206.
122. Lee IJ, Wu JQ (2012) Characterization of Mid1 domains for targeting and scaffolding in fission yeast cytokinesis. Journal of Cell Science 125: 2973-2985.
123. Levin DE, Bishop JM (1990) A putative protein kinase gene (kin1+) is important for growth polarity in Schizosaccharomyces pombe. Proc Natl Acad Sci U S A 87: 8272-8276.
124. Osumi M (1998) The ultrastructure of yeast: Cell wall structure and formation. Micron 29: 207-233.

125. Drummond DR, Cross RA (2000) Dynamics of interphase microtubules in Schizosaccharomyces pombe. Current Biology 10: 766-775.
126. Tischer C, Brunner D, Dogterom M (2009) Force- and kinesin-8-dependent effects in the spatial regulation of fission yeast microtubule dynamics. Molecular Systems Biology 5.
127. Snaith HA, Sawin KE (2003) Fission yeast mod5p regulates polarized growth through anchoring of tea1p at cell tips. Nature 423: 647-651.
128. Martin SG, McDonald WH, Yates JR, Chang F (2005) Tea4p links microtubule plus ends with the formin For3p in the establishment of cell polarity. Developmental Cell 8: 479-491.
129. Bicho CC, Kelly DA, Snaith HA, Goryachev AB, Sawin KE (2010) A catalytic role for Mod5 in the formation of the Tea1 cell polarity landmark. Curr Biol 20: 1752-1757.
130. Saunders TE, Pan KZ, Angel A, Guan Y, Shah JV, et al. (2012) Noise reduction in the intracellular pom1p gradient by a dynamic clustering mechanism. Developmental Cell 22: 558-572.
131. Hirata D, Masuda H, Eddison M, Toda T (1998) Essential role of tubulin-folding cofactor D in microtubule assembly and its association with microtubules in fission yeast. Embo Journal 17: 658-666.
132. Thadani R, Huang D, Oliferenko S (2011) Robust polarity specification operates above a threshold of microtubule dynamicity. Cytoskeleton (Hoboken) 68: 290-299.
133. Glynn JM, Lustig RJ, Berlin A, Chang F (2001) Role of bud6p and tea1p in the interaction between actin and microtubules for the establishment of cell polarity in fission yeast. Current Biology 11: 836-845.
134. Yaffe MP, Harata D, Verde F, Eddison M, Toda T, et al. (1996) Microtubules mediate mitochondrial distribution in fission yeast. Proceedings of the National Academy of Sciences of the United States of America 93: 11664-11668.
135. Hagan IM (1998) The fission yeast microtubule cytoskeleton. Journal of Cell Science 111: 1603-1612.
136. Paoletti A, Chang F (2000) Analysis of mid1p, a protein required for placement of the cell division site, reveals a link between the nucleus and the cell surface in fission yeast. Molecular Biology of the Cell 11: 2757-2773.
137. Castagnetti S, Behrens R, Nurse P (2005) End4/Sla2 is involved in establishment of a new growth zone in Schizosaccharomyces pombe. Journal of Cell Science 118: 1843-1850.
138. Bendezú F, Martin S (2013) Cdc42 Explores the Cell Periphery for Mate Selection in Fission Yeast. Current Biology 23: 42-47.
139. Chebli Y, Kaneda M, Zerzour R, Geitmann A (2012) The cell wall of the Arabidopsis pollen tube--spatial distribution, recycling, and network formation of polysaccharides. Plant Physiology 160: 1940-1955.
140. Fayant P, Girlanda O, Chebli Y, Aubin CE, Villemure I, et al. (2010) Finite element model of polar growth in pollen tubes. Plant Cell 22: 2579-2593.
141. Latge JP (2007) The cell wall: a carbohydrate armour for the fungal cell. Molecular Microbiology 66: 279-290.

142. Manners DJ, Meyer MT (1977) Molecular-Structures of Some Glucans from Cell-Walls of Schizosaccharomyces-Pombe. Carbohydrate Research 57: 189-203.
143. Howard RJ (1981) Ultrastructural Analysis of Hyphal Tip Cell-Growth in Fungi - Spitzenkorper, Cytoskeleton and Endomembranes after Freeze-Substitution. Journal of Cell Science 48: 89-103.
144. Eggen E, de Keijzer MN, Mulder BM (2011) Self-regulation in tip-growth: The role of cell wall ageing. Journal of Theoretical Biology 283: 113-121.
145. Gierz G, Bartnicki-Garcia S (2001) A three-dimensional model of fungal morphogenesis based on the vesicle supply center concept. Journal of Theoretical Biology 208: 151-164.
146. Goriely A, Tabor M (2003) Biomechanical models of hyphal growth in actinomycetes. Journal of Theoretical Biology 222: 211-218.
147. Campas O, Mahadevan L (2009) Shape and dynamics of tip-growing cells. Curr Biol 19: 2102-2107.
148. Daniel RA, Errington J (2003) Control of cell morphogenesis in bacteria: two distinct ways to make a rod-shaped cell. Cell 113: 767-776.
149. Dominguez-Escobar J, Chastanet A, Crevenna AH, Fromion V, Wedlich-Soldner R, et al. (2011) Processive Movement of MreB-Associated Cell Wall Biosynthetic Complexes in Bacteria. Science 333: 225-228.
150. Garner EC, Bernard R, Wang WQ, Zhuang XW, Rudner DZ, et al. (2011) Coupled, Circumferential Motions of the Cell Wall Synthesis Machinery and MreB Filaments in B. subtilis. Science 333: 222-225.
151. Wang S, Furchtgott L, Huang KC, Shaevitz JW (2012) Helical insertion of peptidoglycan produces chiral ordering of the bacterial cell wall. Proceedings of the National Academy of Sciences of the United States of America 109: E595-E604.
152. Swulius MT, Jensen GJ (2012) The Helical MreB Cytoskeleton in Escherichia coli MC1000/pLE7 Is an Artifact of the N-Terminal Yellow Fluorescent Protein Tag. Journal of Bacteriology 194: 6382-6386.
153. Huang KC, Mukhopadhyay R, Wen B, Gitai Z, Wingreen NS (2008) Cell shape and cell-wall organization in Gram-negative bacteria. Proc Natl Acad Sci U S A 105: 19282-19287.
154. Furchtgott L, Wingreen NS, Huang KC (2011) Mechanisms for maintaining cell shape in rod-shaped Gram-negative bacteria. Molecular Microbiology 81: 340-353.
155. Jiang H, Si F, Margolin W, Sun SX (2011) Mechanical control of bacterial cell shape. Biophys J 101: 327-335.
156. Wang S, Wingreen Ned S (2013) Cell Shape Can Mediate the Spatial Organization of the Bacterial Cytoskeleton. Biophysical Journal 104: 541-552.
157. Minc N, Chang F (2010) Electrical Control of Cell Polarization in the Fission Yeast Schizosaccharomyces pombe. Current Biology 20: 710-716.

7.Vita

Tyler Gates Drake

EDUCATION:

College of Arts and Sciences Lehigh University, Bethlehem, PA	Doctor of Philosophy Physics
College of Arts and Sciences Drew University, Madison, NJ	Bachelor of Arts, 2007 *Summa cum laude* Physics, Math

SELECTED ACADEMIC AWARDS AND HONORS:

- Graduate Assistance in Areas of National Need (GAANN) Fellow at Lehigh University
- Mars Corporation Fellow at the 2012 Lindau Nobel Laureates Meeting
- Society for Industrial and Applied Mathematics First-Place Poster Prize, Graduate Student Division, 2010 Life Sciences Division Meeting
- Grant-In-Aid Award, Sigma Xi Research Society
- Yoshida–Dierolf Travel Award, Physics Department, Lehigh University
- Novartis Award for Excellence in Mathematics, Drew University

<u>Peer-Reviewed Journal Articles:</u>

1) **Drake T**, Vavylonis D. *Model of fission yeast shape driven by membrane-bound growth factors and the cytoskeleton*, PLoS Computational Biology, **9:**e1003287 (2013).

2) Das M*, **Drake T***, Wiley DJ, Buchwald P, Vavylonis D, Verde F. (2012). *Oscillatory dynamics and long-range competition for Cdc42 between distinct growth zones in the control of bipolar growth*, Science; 337: 239-43. *: co-first authors.

3) **Drake T**, Vavylonis D. (2010). *Cytoskeleton dynamics in fission yeast: a review of models for polarization and division.* HFSP Journal; 4: 122-130.

4) Andrews S, **Drake T**, Munusamy R, Haslett W. (2010). *Dartmouth Decision Support Designer Software*. Psychiatric Rehabilitation Journal; 34: 37-41.

5) Drake RE, Woltmann EM, Deegan P, Haslett W, **Drake T**, Rapp C. (2010). *Comprehensive Electronic Decision Support Systems*. Psychiatric Services; 61(7): 714-717.

6) Morgus L, Morgus T, **Drake T**, Huennekens J. (2008) *Hyperfine state changing collisions of Cs(6P1/2) atoms with argon perturbers*. Physical Review A. 77:032704.

7) Husain A, Hone J, Postma HWC, Huang XMH, **Drake T**, Barbic M, Scherer A, Roukes ML. (2003) *Nanowire-based very-high-frequency electromechanical resonator*. Applied Physics Letters; 70:1327.

Peer-Reviewed Book Chapters:

1) Drake T, Yusuf E, Vavylonis D. *A Systems-Biology Approach to Yeast Actin Cables*. In Goryanin II, Goryachev AB, *Advances in Systems Biology*. Series: *Advances in Experimental Medicine and Biology*, Vol. 736. New York City: Springer Publishing, 2012.